SLAC-R-549
UC-414

Measurement of the $Z^0 \to s\bar{s}$ Coupling at the SLD*

Hermann Stängle

Stanford Linear Accelerator Center
Stanford University
Stanford, CA 94309

SLAC-Report-549
November 1999

Prepared for the Department of Energy
under contract number DE-AC03-76SF00515

*Ph.D. thesis, Colorado State University, Fort Collins, Colorado

ABSTRACT OF DISSERTATION

MEASUREMENT OF THE $Z^0 \to s\bar{s}$ COUPLING AT THE SLD

This dissertation presents a direct measurement of the parity-violating coupling of the Z^0 to strange quarks, A_s, derived from e^+e^- collision data containing approximately 550,000 hadronic decays of polarized Z^0 bosons. Data were recorded with the SLC Large Detector (SLD) at the SLAC Linear Collider (SLC) between 1993 and 1998 with an average electron beam polarization of 73% and 74% during the 1993-5 and 1996-8 run periods, respectively. Making use of several unique features of the SLC and SLD, this measurement relies on a new generation particle identification system, the Cherenkov Ring Imaging Detector, to test the Standard Model prediction of universality in the coupling of the Z^0 to down-type quarks. Polarized $Z^0 \to s\bar{s}$ events are tagged by the presence in each event hemisphere of a high-momentum $K^{\pm}$, K^0_s or $\Lambda^0/\bar{\Lambda}^0$ identified using particle identification and/or a mass tag. The background from heavy flavor events is suppressed with the CCD-based vertex detector. The event thrust axis is signed with the strangeness of the tagged particle to point in the direction of the initial s quark. The coupling A_s is derived from a maximum likelihood fit to the polar angle distributions of the tagged s quark measured with left- and right-handed electron beams. To reduce the model dependence of the measurement, the background from $u\bar{u}$ and $d\bar{d}$ events as well as the analyzing power of the method for $s\bar{s}$ events are constrained from the data. We obtain $A_s = 0.86 \pm 0.08(stat.) \pm 0.05(syst.)$. The result is consistent with both the Standard Model prediction and previous bottom quark coupling, A_b, measurements performed by SLD and LEP, and therefore supports the predicted universality of the Z^0 to down-type quark couplings.

Hermann Stängle
Physics Department
Colorado State University
Fort Collins, CO 80523
Fall 1999

Acknowledgements

It is with joyful gratitude that I appreciate the helpful guidance, encouragement, and support I have received during my thesis work.

In particular, I am indebted to my adviser, Dr. Robert J. Wilson, to whom I owe my entire SLD experience. I thank all members of our HEP Group at Colorado State University for cultivating an enjoyable work atmosphere.

Very special thanks go to Dr. David R. Muller and Dr. Kenneth G. Baird for the insightful help and advice in both physics analysis and the details of the CRID detector. I wish to thank all members in the SLD QCD group for the many helpful physics discussions and the SLD CRID group for the opportunity to obtain hardware experience.

I would like to thank the SLD collaboration, the SLC physicists, and the technical staff at SLAC whose dedication have made the SLD experiment successful.

My thanks and best wishes go to people in Fort Collins who make Colorado State University such a welcoming place for international students.

Last, but really first, I wish to thank my family: my mother, Anna Maria, my brothers Johannes and Gerhard, and my twin sister Renate Barbara, for their endless love, encouragement, patience, and support.

Table of Contents

List of Figures

List of Tables

Chapter 1

Introduction

The scientific attempt to answer the old question: "What is the world made of?" led to the formulation of the Standard Model describing our current knowledge on the properties and interactions of elementary particles. This theory has provided a remarkably successful description of a variety of physics phenomena at energies accessible to experimental facilities.

In the $Z^0 \to f\bar{f}$ coupling, parity violation arises from the difference in strength between the right-handed and left-handed coupling of the fermion f to the Z^0 boson. The extent of parity violation in the $Z^0 \to f\bar{f}$ coupling is represented by the coupling parameter, A_f.

Measurements of fermion production asymmetries allow these coupling parameters to be determined, and provide an important tool for precision tests of the Standard Model which predicts that all down-type quark couplings to the Z^0 are *universal*, and therefore $A_d = A_s = A_b$. Similarly, this statement separately holds for the up-type quark couplings and the lepton couplings. Provided with a measurement of the electroweak mixing angle, $\sin^2\theta_W$, the Standard Model predicts the values of the couplings.

In order to test these predictions, it is important to precisely measure as many of the coupling parameters as possible. Experiments at the Large Electron Positron Collider (LEP) and at the SLAC Linear Collider (SLC) have contributed a series of previous measurements of A_e, A_μ, A_τ, A_c and A_b [1], supporting lepton universality and the prediction for A_c. However, the current averages for the bottom quark coupling from SLD, $A_b = 0.898 \pm 0.029$ [2], and from LEP, $A_b = 0.887 \pm$

0.021 [2], appear to be converging to a lower value than predicted by the Standard Model. This potential discrepancy heightens the interest in a precise measurement of A_s to investigate further universality of the down-type quark couplings.

Compared with the situation in the lepton and heavy-flavor sector, very few measurements [3; 4] have been performed for the light-flavor quark couplings due to the difficulty of tagging specific light flavors. Recently, it has been demonstrated experimentally [5–9] that light-flavor jets can be tagged by the presence of a high-momentum 'leading' identified particle containing a valence quark of the desired flavor, e.g. a K^- (K^+) meson could tag an s ($\bar{s}$) jet. However, the background from other light flavors (a $\bar{u}$ jet can also produce a leading K^-), decays of B and D hadrons, and non-leading kaons in events of all flavors is large, and neither the signal nor the background have been well measured experimentally. Therefore only qualitative aspects of the 'leading particle' effect have been incorporated into fragmentation models used to simulate the QCD fragmentation process. The analysis strategy pursued in this thesis employs a sample of high-momentum strange particles that are tagged with high purity and efficiency to obtain a candidate event sample of high $s\bar{s}$ purity. In this respect, a measurement of A_s probes aspects of both electroweak and strong interactions.

In contrast to measurements performed at LEP, the highly polarized electron beam at the SLD allows a direct measurement of the final state coupling, i.e. independent of the initial state coupling. In combination with the small and stable interaction region provided by the SLC, precision tracking and vertexing, and the capability of efficient particle identification with the Cherenkov Ring Imaging Detector (CRID), the SLD is well equipped for this measurement.

This thesis presents a direct measurement of the coupling parameter for strange quarks, A_s, using a sample of 550,000 hadronic Z^0 decays recorded by the SLD experiment at the SLAC Linear Collider between 1993 and 1998. The average electron beam polarization in the 1993-5 and

1996-8 data runs was 73% and 74%, respectively. Polarized $Z^0 \to s\bar{s}$ events are tagged by the presence in each event hemisphere of a high-momentum $K^{\pm}$, K^0_s or $\Lambda^0/\bar{\Lambda}^0$ identified using particle identification and/or a mass tag. The background from heavy flavor events ($c\bar{c}$ and $b\bar{b}$) is suppressed using lifetime information determined by the decay vertex reconstruction. The background from the other light flavors ($u\bar{u}$ and $d\bar{d}$) is suppressed by the additional requirement of a high-momentum strange particle in the opposite hemisphere of the event. The event thrust axis is signed with the strangeness of the tagged particle to point in the direction of the initial s quark. The coupling A_s is extracted from a maximum likelihood fit to the polar angle distributions measured with left- and right-handed electron beams. The analyzing power of the tags for true $s\bar{s}$ events, as well as the relative contribution of $u\bar{u} + d\bar{d}$ events, are constrained using data. This procedure removes much of the model dependence.

This thesis is organized as follows. Chapter 2 presents an overview of the Standard Model. Electroweak interactions are summarized with an emphasis on electroweak asymmetries, followed by an outline of the strong interaction and its manifestation in the hadronization process, and a brief summary of major fragmentation models. A general overview of the SLC accelerator and the SLD detector is provided in Chapter 3, followed by a description of the simulation used to model both the Monte Carlo event generation and the SLD detector response. Particle identification with the SLD CRID is crucial to this analysis, and Chapter 4 presents details of its operation principle. The CRID calibration is described including details of the author's contribution to its alignment, and the physics performance of the CRID is summarized. Chapter 5 discusses SLD event triggers and the hadronic event selection for this analysis, followed by the technique employed to select light flavor events. Chapter 6 describes the selection of fast strange particles ($K^{\pm}$, K_s and $\Lambda^0/\bar{\Lambda}^0$), and then motivates the author's approach to using these particles to obtain a tagged sample of relatively high $s\bar{s}$ purity. Chapter 7 introduces the maximum likelihood fit

method used to obtain A_s, and Chapter 8 presents the systematic uncertainties associated with this measurement. Chapter 9 summarizes the result of this analysis, provides a comparison with the existing LEP measurements, and comments on future prospects for this measurement.

The preliminary results from the analysis detailed in this thesis have been presented by the author at two U.S. conferences (APS, Columbus, Ohio, April 1998; and DPF, Los Angeles, California, January 1999) and one international conference (QCD Moriond, Les Arcs, France, March 1999).

Chapter 2

Standard Model Overview

The Standard Model describes elementary particles and their electroweak and strong interactions within a framework based on Quantum Field Theory. Effects of gravity, described by General Relativity, are not included in the Standard Model, but are negligibly small on the scale of particle interactions. Details on the Standard Model can be found in, for example, Ref. [10; 11], and the status of precision tests confronting its predictions is summarized in Ref. [1; 12]. The measurement of A_s probes aspects of both electroweak and strong interactions. This chapter provides an overview of the Standard Model and emphasizes areas related to the analysis.

2.1 Electroweak Interactions in the Standard Model

Electromagnetic and weak interactions were unified into a single interaction with $SU(2)_L \otimes U(1)$ gauge symmetry by Glashow [13], Salam [14] and Weinberg [15]. This forms the basis of the Standard Model. The fundamental matter particles in the Standard Model are leptons and quarks. Gauge bosons are the propagators of the forces. The arrangement of the fundamental leptons and quarks into left-handed weak isospin doublets and right-handed weak isospin singlets is shown in Table 2.1. The electric charge, Q, is related to the 3^{rd} component of the weak isospin, T^3, and the weak hypercharge, Y, by:

$$Q = T^3 + \frac{Y}{2}. \tag{2.1}$$

The fundamental fermions have been grouped into three fermion families although the deeper reason for this repetition remains unexplained. The gauge bosons mediating the interactions between these fermions are listed in Table 2.2. The massless photon mediates the electromagnetic force, the massive $W^{\pm}$ and Z^0 bosons transmit the weak forces, and massless gluons are the carriers of the strong force. The neutral leptons experience only weak interactions, the charged leptons also interact electromagnetically, and the quarks interact with all three forces.

Table 2.1: Some properties of the three fundamental fermion families.

Fermion families			Quantum numbers		
1^{st}	2^{nd}	3^{rd}	Q	T^3	Y
$\begin{pmatrix} \nu_e \\ e \end{pmatrix}_L$	$\begin{pmatrix} \nu_\mu \\ \mu \end{pmatrix}_L$	$\begin{pmatrix} \nu_\tau \\ \tau \end{pmatrix}_L$	$\begin{pmatrix} 0 \\ -1 \end{pmatrix}$	$\begin{pmatrix} \frac{1}{2} \\ -\frac{1}{2} \end{pmatrix}$	$\begin{pmatrix} -1 \\ -1 \end{pmatrix}$
$\begin{pmatrix} u \\ d \end{pmatrix}_L$	$\begin{pmatrix} c \\ s \end{pmatrix}_L$	$\begin{pmatrix} t \\ b \end{pmatrix}_L$	$\begin{pmatrix} \frac{2}{3} \\ -\frac{1}{3} \end{pmatrix}$	$\begin{pmatrix} \frac{1}{2} \\ -\frac{1}{2} \end{pmatrix}$	$\begin{pmatrix} \frac{1}{3} \\ -\frac{1}{3} \end{pmatrix}$
e_R	μ_R	τ_R	-1	0	-2
u_R	c_R	t_R	$\frac{2}{3}$	0	$\frac{4}{3}$
d_R	s_R	b_R	$-\frac{1}{3}$	0	$-\frac{2}{3}$

Similar to the A^μ fields of electromagnetism, gauge bosons are introduced into the Standard Model by the requirement of local gauge invariance. Quantum Electrodynamics (QED [10; 11]) can be developed from the interaction:

$$-ie j^{em}_\mu A^\mu = -ie(\bar{\psi}\gamma_\mu Q\psi)A^\mu \tag{2.2}$$

where the electromagnetic current, j^{em}_μ, couples to the A^μ field, $-e$ denotes the electron charge,

Table 2.2: Some characteristics of fundamental interactions, excluding gravity.

Interaction	Electroweak	Strong
Theory	Glashow-Salam-Weinberg	QCD
Gauge group	$SU(2)_L \otimes U(1)$	$SU(3)$
Gauge boson	γ, Z^0, $W^{\pm}$	8 gluons
Spin	1, 1, 1	1
Mass	0, 91 GeV/c^2, 80 GeV/c^2	0
Charge	weak isospin, weak hypercharge	color
Coupling	g, $g\prime$	α_s

Q is the charge operator, γ^μ are the Dirac matrices, and ψ represents the wavefunction, with its adjoint $\bar{\psi} = \psi^\dagger \gamma^0$.

In the Standard Model, we include weak interaction processes by introducing a massless $SU(2)$ isotriplet W^i_μ $(i = 1, 2, 3)$ coupling with strength g to the weak isospin current, J^i_μ, and a massless $U(1)$ isosinglet B_μ coupling with strength $g\prime$ to the weak hypercharge current, j^Y_μ:

$$-ig(J^i)^\mu W^i_\mu - i\frac{g\prime}{2}(j^Y)^\mu B_\mu. \tag{2.3}$$

The physical gauge bosons are given by combinations of the W^i_μ and B_μ fields:

$$\begin{aligned} A_\mu &= B_\mu \cos\theta_W + W^3_\mu \sin\theta_W \\ Z_\mu &= -B_\mu \sin\theta_W + W^3_\mu \cos\theta_W \\ W^\pm_\mu &= \frac{1}{\sqrt{2}}(W^1_\mu \mp iW^2_\mu) \end{aligned} \tag{2.4}$$

with the electroweak mixing angle, θ_W. Therefore the electroweak neutral current interaction can

be written as a sum of electromagnetic and weak neutral terms:

$$-igJ^3_\mu(W^3)^\mu - i\frac{g\prime}{2}j^Y_\mu B^\mu = \\ -i(g\sin\theta_W J^3_\mu + g\prime\cos\theta_W\frac{j^Y_\mu}{2})A^\mu - i(g\cos\theta_W J^3_\mu - g\prime\sin\theta_W\frac{j^Y_\mu}{2})Z^\mu. \tag{2.5}$$

Comparing the first term with the electromagnetic interaction we obtain:

$$j^{em}_\mu = J^3_\mu + \frac{1}{2}j^Y_\mu \tag{2.6}$$

$$g\sin\theta_W = g\prime\cos\theta_W = e \tag{2.7}$$

so that the mixing angle is given by $\tan\theta_W = g\prime/g$. The weak neutral current, J^{NC}_μ, can be obtained from the second term as:

$$J^{NC}_\mu = J^3_\mu - j^{em}_\mu\sin^2\theta_W \tag{2.8}$$

The weak neutral current interaction for the $Z^0 \to f\bar{f}$ process is given by:

$$-i\frac{g}{\cos\theta_W}J^{NC}_\mu Z^\mu = -i\frac{g}{\cos\theta_W}\bar{\psi}_f\gamma^\mu(\frac{1}{2}(1-\gamma^5)T^3 - Q\sin^2\theta_W)\psi_f Z_\mu \tag{2.9}$$

with $\gamma^5 = i\gamma^0\gamma^1\gamma^2\gamma^3$. From the expression of the $Z^0 \to f\bar{f}$ vertex factor:

$$-i\frac{g}{\cos\theta_W}\frac{\gamma^\mu}{2}(v_f - a_f\gamma^5) \tag{2.10}$$

where v_f and a_f denote the vector and axial-vector couplings, respectively, we conclude that these

couplings are given in the Standard Model once $\sin^2\theta_W$ is determined:

$$\begin{aligned} a_f &= T_f^3 \\ v_f &= T_f^3 - 2Q_f \sin^2\theta_W \end{aligned} \tag{2.11}$$

Table 2.3 summarizes the vector couplings and axial-vector couplings of the fermions to the Z^0. At this stage, the gauge bosons are massless in the theory. The Higgs mechanism [17] is invoked to break the $SU(2)_L \otimes U(1)$ symmetry spontaneously, thereby generating mass for the Z^μ and $W^\pm$, i.e. the physical Z^0 and $W^\pm$ masses, but leaving the A^μ field, i.e. the photon, massless.

Table 2.3: Vector couplings and axial-vector couplings of the Z^0 to fundamental fermions.

Fermion	a_f	v_f
ν_e, ν_μ, ν_τ	$+\frac{1}{2}$	$+\frac{1}{2}$
e, μ, τ	$-\frac{1}{2}$	$-\frac{1}{2} + 2\sin^2\theta_W$
u, c, t	$+\frac{1}{2}$	$+\frac{1}{2} - \frac{4}{3}\sin^2\theta_W$
d, s, b	$-\frac{1}{2}$	$-\frac{1}{2} + \frac{2}{3}\sin^2\theta_W$

In addition to the fermion masses, the Higgs mass, and the CKM mixings [10], the Standard Model can be parametrized with three free parameters. In practice, variables are chosen which are easily related to experimentally accessible measurements. These are the fine structure constant, α, the Fermi constant, G_F, and the mass of the Z^0, M_{Z^0}. The current values of these three parameters [19] are:

- $\alpha = 1/137.035989(61)$
- $G_F = 1.16639(1) \times 10^{-5}$ GeV^{-2}
- $M_{Z^0} = 91.187(7)$ GeV/c^2

where 1 σ uncertainties in the last digits are denoted by parentheses after the values. In 1983, the UA-1 [18] experiment discovered the Z^0 and $W^{\pm}$ bosons. However the Higgs particle has not been observed. Recent searches for the Higgs particle set an upper limit on its mass of 230 GeV/c^2 at 95% confidence level [2].

2.1.1 Fermion Production Cross Section at the Z^0

In the process $e^+e^- \rightarrow Z^0/\gamma \rightarrow f\bar{f}$ where f is a fermion (other than an electron), the only processes that contribute to the cross section at tree level are the s channel γ and Z^0 exchanges. The Feynman diagrams for these contributions are shown in Figure 2.1.

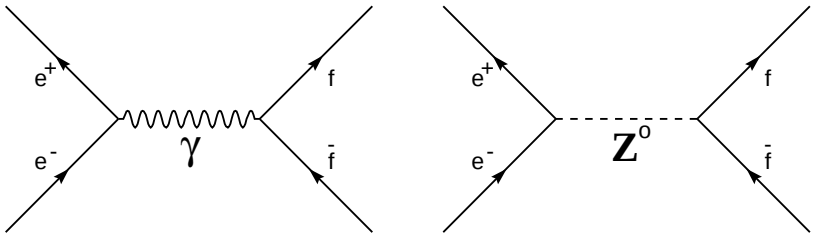

Figure 2.1: The s channel tree-level Feynman diagrams for the process $e^+e^- \rightarrow Z^0/\gamma \rightarrow f\bar{f}$.

The differential production cross section for a particular reaction describes the probability for an interaction to happen in a particular angular configuration. For the process $e^+e^- \rightarrow Z^0/\gamma \rightarrow f\bar{f}$, the differential production cross section [10] in the center of mass frame is given by:

$$\frac{d\sigma}{d\Omega} = \frac{1}{64\pi^2 s}\frac{p_f}{p_e}|\mathcal{M}_{Z^0} + \mathcal{M}_{\gamma}|^2 \tag{2.12}$$

where $\mathcal{M}_{Z^0}$ and $\mathcal{M}_{\gamma}$ denote the matrix elements for Z^0 and γ exchange, $\sqrt{s}$ is the total energy, and p_e and p_f are the momenta of the incoming electron and outgoing fermion, respectively. Therefore

the differential production cross section for this process contains a γ exchange term a Z^0 exchange term and a γ/Z^0 interference term. Figure 2.2 shows the cross section for $e^+e^- \rightarrow hadrons$ as a function of center of mass energy. At the Z^0 pole the Z^0 exchange term dominates the γ exchange term by a factor of approximately 800 and the γ/Z^0 interference term vanishes.

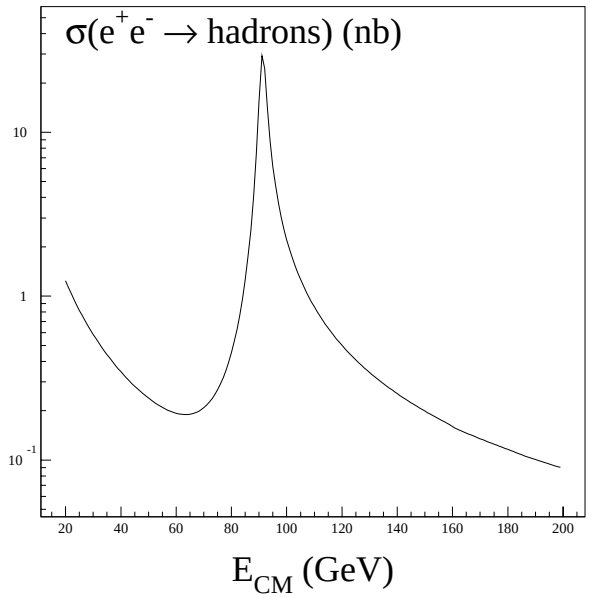

Figure 2.2: Energy dependence of the $e^+e^- \rightarrow hadrons$ cross section.

In the following we will only consider the Z^0 exchange term. Its matrix element $\mathcal{M}_{Z^0}$ is given by:

$$\mathcal{M}_{Z^0} = -\frac{g^2}{4\cos^2\theta_W}\left\{\bar{f}\gamma^\nu\left(v_f - a_f\gamma^5\right)f\right\}\frac{g_{\nu\mu} - k_\nu k_\mu/M_{Z^0}^2}{k^2 - M_{Z^0}^2}\left\{\bar{e}\gamma^\mu\left(v_e - a_e\gamma^5\right)e\right\}, \qquad (2.13)$$

where f and e represent the fermion and electron wavefunctions M_{Z^0} and , $_{Z^0}$ are the mass and width of the Z^0 respectively and k denotes the 4-momentum of the virtual Z^0. It is customary to express the left- (c_L^f) and right-handed (c_R^f) couplings of the Z^0 to the fermion f in terms of v_f

and a_f:

$$\begin{aligned} c_L^f &= \frac{1}{2}(v_f + a_f) \\ c_R^f &= \frac{1}{2}(v_f - a_f). \end{aligned} \tag{2.14}$$

After summing over the final state fermion polarization, the differential cross sections [16] are given by:

$$\frac{d\sigma_L}{d\Omega} \propto (c_R^{f\,2} + c_L^{f\,2})(1 + x^2) - 2(c_R^{f\,2} - c_L^{f\,2})x \tag{2.15}$$

$$\frac{d\sigma_R}{d\Omega} \propto (c_R^{f\,2} + c_L^{f\,2})(1 + x^2) + 2(c_R^{f\,2} - c_L^{f\,2})x \tag{2.16}$$

where the helicity index L (R) refers to the incoming electron, and $x = \cos\theta$, where θ is the polar angle of the final state fermion f with respect to the electron beam direction. For a partially polarized incoming electron beam, and an unpolarized positron beam, the differential production cross section at the Born level can be written as:

$$\frac{d\sigma^f}{d\Omega} = D(s)(v_e^2 + a_e^2)(v_f^2 + a_f^2)\left\{(1 - A_e P_e)(1 + x^2) + 2A_f(A_e - P_e)x\right\} \tag{2.17}$$

where P_e is the longitudinal polarization of the electron beam, and the coupling parameters:

$$A_f = \frac{(c_L^f)^2 - (c_R^f)^2}{(c_L^f)^2 + (c_R^f)^2} = \frac{2v_f a_f}{v_f^2 + a_f^2} \tag{2.18}$$

are defined in terms of the vector and axial-vector or left-handed and right-handed couplings

introduced earlier. The coefficient $D(s)$ is given by:

$$D(s) = \frac{\alpha^2}{4\sin^4 2\theta_W} \frac{s}{(s - M_{Z^0}^2)^2 + \frac{\Gamma_{Z^0}^2 s^2}{M_{Z^0}^2}} \tag{2.19}$$

in terms of α the fine structure constant at the Z^0 the center of mass energy $\sqrt{s}$ and the Z^0 decay width $, _{Z^0}$. Some properties of the Z^0 [19] are summarized in Table 2.4. The coupling parameters A_f (assuming $\sin^2\theta_W = 0.23$) and their sensitivity to $\sin^2\theta_W$ are given in Table 2.5.

Table 2.4: Some Z^0 properties.

$M_{Z^0} = 91.187 \pm 0.007$ GeV/c^2 $, _{Z^0} = 2.490 \pm 0.007$ GeV	
Z^0 decay branching ratios	in %
e^+e^-	3.366 ± 0.008
$\mu^+\mu^-$	3.367 ± 0.013
$\tau^+\tau^-$	3.360 ± 0.015
l^+l^-	3.366 ± 0.006
invisible	20.01 ± 0.16
hadrons	69.90 ± 0.15
$(u\bar{u} + c\bar{c})/2$	10.1 ± 1.1
$(d\bar{d} + s\bar{s} + b\bar{b})/3$	16.6 ± 0.6
$c\bar{c}$	12.4 ± 0.6
$b\bar{b}$	15.16 ± 0.09

Table 2.5: Coupling parameters A_f and sensitivity to $\sin^2\theta_W$.

Fermion	A_f	$\frac{\partial A_f}{\partial \sin^2\theta_W}$
e, μ, τ	0.16	-7.85
u, c, t	0.67	-3.43
d, s, b	0.94	-0.63

2.2 Electroweak Production Asymmetries

The calculated cross sections of the process $Z^0 \to f\bar{f}$ allow the theoretical formalism outlined so far to be related to experimentally accessible quantities. Normalized differences of production cross sections constitute powerful tools for performing precision tests of the Standard Model. At the SLC/SLD, the large production asymmetry in $\cos\theta$ for negative and positive electron beam polarization at the Z^0 pole is particularly suited to the study of electroweak asymmetries. Figure 2.3 shows the production asymmetry, normalized to the total production cross section, derived for three values of the electron beam polarization: $|P_e| = 0$ and assuming $|P_e| = \pm 0.73$. We show the distributions for up-type quarks, down-type quarks, and the charged leptons, and assume a value of $A_e = 0.15$ at the initial state vertex.

2.2.1 Left-Right Asymmetry A_{LR}

The definition of the left-right asymmetry, A_{LR}, makes use of the electron beam polarization produced by the SLC, and is sensitive to spin inversion:

$$A_{LR} = \frac{\sigma(e^+e_L^- \to Z^0 \to f\bar{f}) - \sigma(e^+e_R^- \to Z^0 \to f\bar{f})}{\sigma(e^+e_L^- \to Z^0 \to f\bar{f}) + \sigma(e^+e_R^- \to Z^0 \to f\bar{f})} \tag{2.20}$$

where L (R) denotes the negative (positive) inital electron beam polarization. This normalized difference of cross sections avoids many sources of systematic uncertainty. A_{LR} is one of the most important measurements at the SLD. A_{LR} relates to the electroweak mixing angle, $\sin^2\theta_W$, by:

$$A_{LR}^0 = A_e = \frac{2\{1 - 4\sin^2\theta_W^{eff}(M_{Z^0}^2)\}}{1 + \{1 - 4\sin^2\theta_W^{eff}(M_{Z^0}^2)\}^2} \tag{2.21}$$

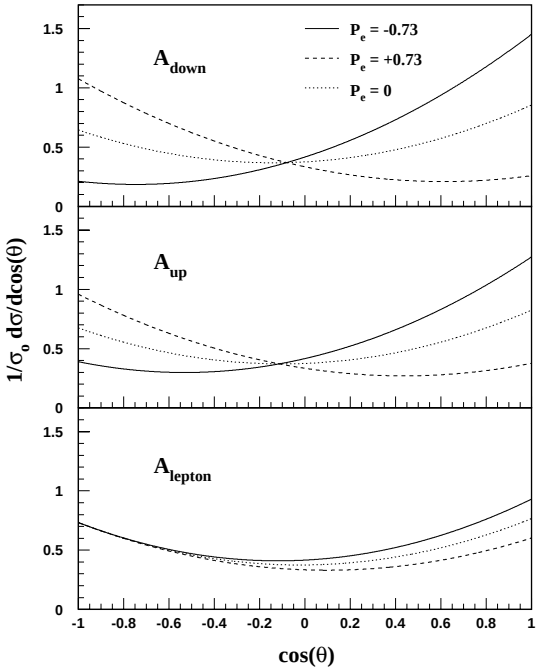

Figure 2.3: Polar angle dependence of the normalized production cross section for positive and negative electron beam polarization.

The 'running' of the coupling constants with energy is indicated by the energy dependence of the weak mixing angle, $\sin^2\theta_W^{eff}$. Here we evaluate the parameter at the Z^0 pole and account for radiative corrections (e.g. [20]) to form an effective mixing angle different from $\sin^2\theta_W$, i.e. the 'bare' tree-level value. The A_{LR} determination is essentially a counting experiment:

$$A_{LR} = \frac{1}{|P_e|}\frac{N_L - N_R}{N_L + N_R} \tag{2.22}$$

in which N_L (N_R) denotes the number of Z^0 decays recorded with left (right) electron beam polarization, P_e. A_{LR} probes the initial state coupling and is independent of the final state coupling; this provides a large statistical advantage since all final states can be used. In practice,

the e^+e^- final state is excluded in order to avoid the admixture of the t channel $e^+e^- \to Z^0/\gamma \to f\bar{f}$ process. SLD has performed several measurements of A_{LR} and $\sin^2\theta_W^{eff}(M_{Z^0}^2)$, the current preliminary SLD values [21] for the 1992-8 data are:

$$A_{LR}^0 = 0.1511 \pm 0.0022 \tag{2.23}$$

$$\sin^2\theta_W^{eff}(M_{Z^0}^2) = 0.23101 \pm 0.00028. \tag{2.24}$$

2.2.2 A_{FB}^f and $\tilde{A}_{FB}^f$

The forward-backward asymmetry, A_{FB}^f, for a given final state $f\bar{f}$ is defined as:

$$A_{FB}^f(x) = \frac{\sigma^f(x) - \sigma^f(-x)}{\sigma^f(x) + \sigma^f(-x)} = 2A_f \frac{A_e - P_e}{1 - A_e P_e} \frac{x}{1 + x^2}. \tag{2.25}$$

where $x = \cos\theta$. This asymmetry is sensitive to space inversion, and depends on both the initial and final state coupling parameters, as well as on the beam polarization. For zero polarization, such as for LEP experiments, one measures the product of couplings $A_e A_f$ which is a rather small number compared to A_f. If the distributions in samples taken with negative (L) and positive (R) beam polarization of magnitude P_e are measured, one can derive the left-right-forward-backward asymmetry, $\tilde{A}_{FB}^f$, which is sensitive to both space and spin inversion, but insensitive to the initial state coupling:

$$\tilde{A}_{FB}^f(x) = \frac{\{\sigma_L^f(x) + \sigma_R^f(-x)\} - \{\sigma_R^f(x) + \sigma_L^f(-x)\}}{\{\sigma_L^f(x) + \sigma_R^f(-x)\} + \{\sigma_R^f(x) + \sigma_L^f(-x)\}} = 2|P_e|A_f \frac{x}{1 + x^2}. \tag{2.26}$$

This quantity isolates the final state coupling and thus allows a direct measurement of the final state couplings at the SLD.

2.3 Strong Interactions in the Standard Model

Strong interactions are described by the $SU(3)$ gauge theory called Quantum Chromodynamics (QCD [22; 23]). In 1964, Gell-Mann [24] and Zweig [25] independently proposed a strong interaction model which envisioned hadrons (baryons and mesons) to be composed of the three quarks u, d, and s. Although successful in explaining many phenomena, such as the occurrence of hadrons in multiplets or the conservation of baryon number in strong interactions, the postulated quarks were first considered merely a notational device rather than physical entities.

In this model, however, difficulties emerged with particles in a totally symmetric quark state, e.g. Ω^-, represented by sss. This configuration appeared to contradict the fundamental Pauli exclusion principle. Han and Nambu [26] resolved this situation by postulating a new quantum number called color and requiring particles to be singlets, referred to as colorless states. In their model, color became part of the wave function and provided the appropriate symmetry to satisfy the Pauli exclusion principle.

The SLAC-MIT deep inelastic scattering experiments [27] in 1968 presented first evidence for the presence of physical quarks. The observed deviations from point like cross sections confirmed Bjorken scaling [28] of the nucleon structure functions. In 1973, the foundations of modern QCD were laid by Gross and Wilczek [22] and Politzer [23]. This theory is based on a non-Abelian local gauge invariant $SU(3)_{color}$ group. The 8 generators of the $SU(3)_{color}$ group involve 8 massless gauge fields, the gluons, g, carrying the strong force. Color is represented as red, green, and blue. The non-Abelian character of the group leads to gluon-gluon couplings which are enhanced due to the gluons being massless. This feature leads to a decrease of the strong coupling constant, α_s, with energy. The strong interaction is asymptotically free which means that as the distance scale becomes smaller, i.e. the momentum transfer becomes larger, the quarks behave like quasi-free

particles. At distances beyond about 1 fm the quarks interact strongly.

Experimental support for QCD came in 1975 from the MARK I experiment at SPEAR [29] where a tendency for particle collimation in a pair of opposite 'jets' was observed in e^+e^- collisions, indicating that hadronic events are initiated by a small number of highly energetic particles. The angular distribution of the jets confirmed the expected spin $\frac{1}{2}$ assignment for the quarks. Four years later experiments at PETRA [30] first reported 3-jet events which are interpreted as the addition of a gluon radiating from one of the primary quarks. An example of a 3-jet event in the SLD is shown in Figure 2.4.

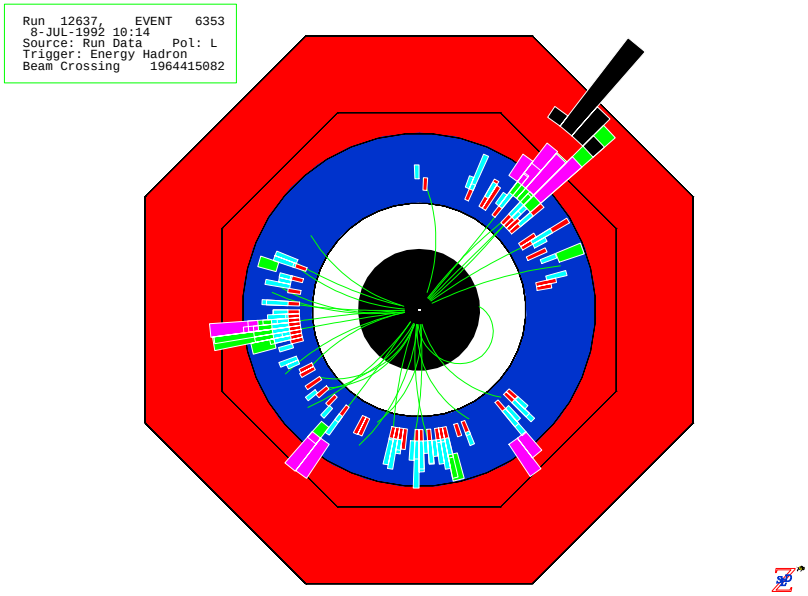

Figure 2.4: A 3-jet hadronic event recorded by the SLD.

All available evidence accumulated since then has served to support QCD predictions. To date, no free quarks have been observed by experiment, so any complete theory of strong interactions must explain why quarks should occur in color singlets only, a property called confinement. It has yet to be proven that QCD implies this property.

Other open questions arise from phenomena like hadronization, the process by which the primary partons, quarks and gluons, form final state hadrons. These calculations require the use of non-perturbative QCD since the strong coupling constant, α_s, becomes larger than unity. Several models for the hadronization process have been proposed and will be discussed below. This is an area where the Standard Model needs further experimental input for the formulation of correct mechanisms.

2.3.1 Production of Hadrons in e^+e^- Collisions

Experimentally observable hadrons emerge from the process $e^+e^- \rightarrow Z^0/\gamma \rightarrow q\bar{q}$ which passes through the stages depicted in Figure 2.5.

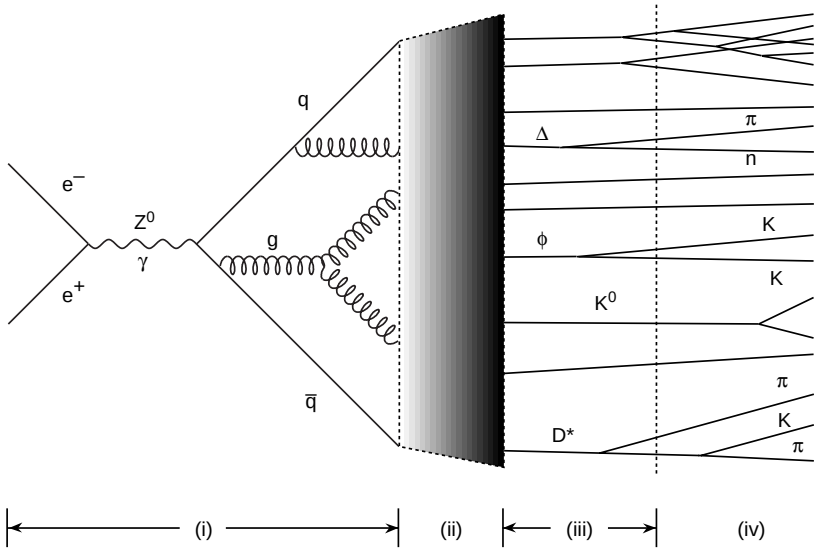

Figure 2.5: Main stages in the $e^+e^- \rightarrow$ *hadrons* process: perturbative, hadronization, and decay. Stage (iv) depicts the experimentally accessible final state.

Formation of a parton shower. In the first stage, the creation of a $q\bar{q}$ pair can be calculated from electroweak physics for which perturbative calculations can be performed to high accuracy. Then perturbative QCD is employed to describe the evolution of the parton shower to the level of

$\alpha_s(\sqrt{s}) \approx 1$ where the partons start to be bound in colorless hadrons.

The tree level $e^+e^- \to q\bar{q}$ diagram is modified by first order QCD correction, i.e. the production of $q\bar{q}g$ where a gluon is emitted. The cross section for the latter process is given in Ref. [31]:

$$\frac{d^2\sigma}{dx_1 dx_2} = \sigma_0 \frac{2\alpha_s}{3\pi} \frac{{x_1}^2 + {x_2}^2}{(1-x_1)(1-x_2)}, \tag{2.27}$$

where σ_0 denotes the tree-level cross section for $e^+e^- \to q\bar{q}$, and $x_i = 2E_i/\sqrt{s}$ describes the parton scaled energies (with $x_1 < x_2 < x_3$ and $\sum x_i = 2$). This equation is clearly divergent for $x_1, x_2 \to 1$; however, these singularities are canceled by the corresponding poles in the $e^+e^- \to q\bar{q}$ cross section from first order virtual corrections. The second order perturbative QCD processes, $e^+e^- \to q\bar{q}gg$ and $e^+e^- \to q\bar{q}q'\bar{q}'$, are calculated in Ref. [32; 33]. For higher orders, calculations become exceedingly complex due to the large number of Feynman diagrams involved. At this stage, parton evolution can be approximated by the parton shower model. The underlying idea in this approach is to consider the generation of partons as successive branchings of partons according to $q \to qg$, $g \to gg$, or $g \to q\bar{q}$. Figure 2.6 presents a schematic view of these successive branchings. The evolution of the probability that a branching $a \to bc$ will take place during a virtuality interval is described by the Dokshitzer-Gribov-Lipatov-Altarelli-Parisi (DGLAP [34–36]) equation. It contains a cut-off scale, equivalent to an effective parton mass, at which the shower formation terminates when approaching the hadron mass scale. The DGLAP equation is applied recurrently in a probabilistic manner to model the parton shower in Figure 2.6.

Hadronizaton. After reaching the hadron mass scale, the partons become bound in colorless hadrons. This QCD process is fundamentally non-pertubative in nature, and several phenomenological fragmentation models, discussed below, have been used as a description.

Final state hadrons. In this stage, unstable hadrons emerge from the hadronization process

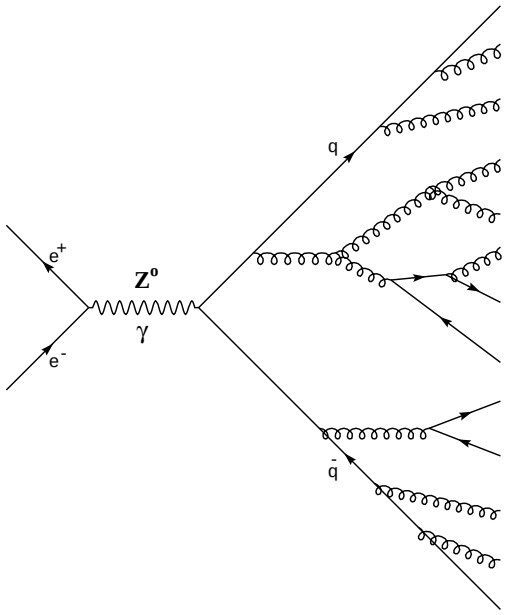

Figure 2.6: Schematic view of a parton shower.

and decay, and their decay products form the final state particles observable in a detector. Quantitative properties of this phase are comparatively well known from experimentally determined production rates and branching fractions. These measurements provide an experimental window to the underlying, non-perturbative fragmentation process.

2.3.2 Fragmentation Models

Due to the non-perturbative nature of the hadronization process, several fragmentation models, motivated by QCD properties, have been employed to simulate this stage. A more detailed review of hadronization models can be found in Ref. [37]. Several types of hadronization models, representing different approaches to hadronization, have been developed:

1. Independent fragmentation

2. Cluster fragmentation

3. String fragmentation

In 1978, Field and Feynman [38] introduced the first fragmentation model based on the notion that each parton fragments independently in a recursive scheme, i.e. the fragmentation process can be described by an incoherent sum of independent fragmentation processes. However, in this model 4-momentum is not conserved, nor is the model Lorentz invariant. Although both difficulties have been overcome by later refinements, this model is rarely used in e^+e^- experiments today.

Cluster fragmentation models take a different approach, and find its most successful implementation in the HERWIG Monte Carlo by Marchesini and Webber [39]. In these models, the parton shower proceeds until all partons reach a virtuality mass cut-off. At this point the gluons decay into $q\bar{q}$ pairs, and the quarks and anti-quarks form colorless clusters, characterized by mass and flavor content. Relatively massive clusters are allowed to fragment into a pair of lighter clusters. Then all clusters decay into hadrons. Conservation of 4-momentum is achieved by its exchange among neighboring clusters. This class of models is advantageous in that the number of tunable parameters is relatively small, thus retaining much of the predictive power.

The string fragmentation model was first introduced by Artru and Mennessier [40], and extended in the JETSET Monte Carlo of Andersson, Gustafson, and Sjöstrand [41; 42]. The basic idea envisions a color flux tube, called a string, stretching between the quarks. The field lines, concentrated in the string by gluon-gluon interactions, connect color charges as shown in Figure 2.7. The major difference with respect to electromagnetic field lines connecting two electrically charged objects is apparent. The color tube has approximately constant energy density per string unit length of about 1 GeV/fm. As the color charges separate, the energy in the string increases linearly. Once the potential energy has grown sufficiently to produce a $q\bar{q}$ pair from the vacuum, the

string breaks with some probability proportional to the pair mass and forms two separate strings. If the invariant mass of either of the new strings is above the hadron mass scale, further splitting occurs until only hadrons remain. Thus breaking color tubes are used as a model for confinement.

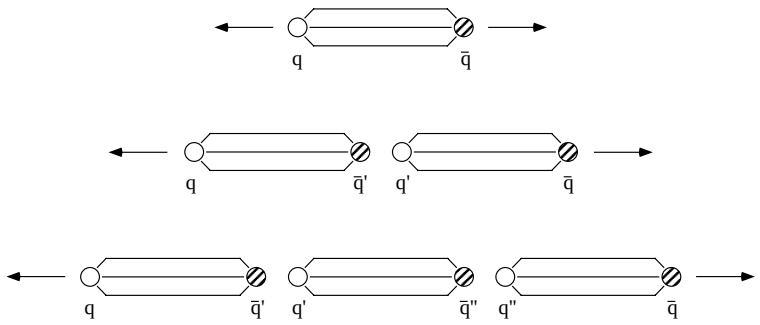

Figure 2.7: Color tube stretching between a q and $\bar{q}$. Increased separation of the q and $\bar{q}$ raises the potential energy in the string to the threshold of $q'\bar{q}'$ creation, when the string breaks.

Energy and momentum are conserved at each step of the fragmentation process. To generate momentum transverse to the string direction in the string breaking process, the $q'\bar{q}'$ pair is created at a point and tunnels with a probability [43] that depends on the transverse momentum, $p_\perp$, and the quark mass, m:

$$P = \exp(-\frac{\pi(p_\perp^2 + m^2)}{\kappa}), \tag{2.28}$$

where κ is the string constant. Thus both heavy particle production and large transverse momentum states are suppressed in the string breaking process. The mass term in the exponent leads to the production ratio: $u : d : s : c \sim 1 : 1 : 0.3 : 10^{-11}$. The strangeness suppression factor, $\gamma_s \sim 0.3$, is an important parameter in all fragmentation models and has been determined experimentally [7]. Finally, a gluon acts like a kink in the sting and is attached to both the q and $\bar{q}$ as shown in Figure 2.8.

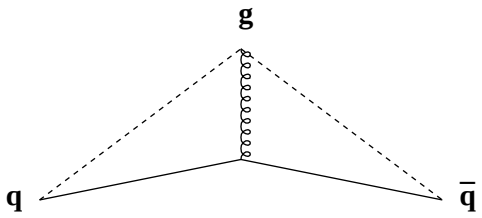

Figure 2.8: String fragmentation in a $q\bar{q}g$ event with the gluon causing a kink in the string.

The string model is 'left-right' symmetric, i.e. the result of the string fragmentation is independent of which end of the string the fragmentation process started. The symmetric Lund fragmentation function, $f(z)$, describes the probability for $z = \frac{(E+p_{\parallel})_{hadron}}{(E+p_{\parallel})_{quark}}$, and is given for $u\bar{u}$, $d\bar{d}$, $s\bar{s}$ events by:

$$f(z) \propto z^{-1}(1-z)^{a} \exp(\frac{-b(p_{\perp}^2 + m^2)}{z}). \tag{2.29}$$

However, a harder fragmentation function is needed for heavy flavors; experimentally it has been found that a good choice is the Peterson fragmentation function:

$$f(z) \propto \frac{1}{z(1-\frac{1}{z}-\frac{\epsilon}{1-z})^2} \tag{2.30}$$

Figure 2.9 shows the symmetric Lund fragmentation function with the parameters $a = 0.18$, $b = 0.34$, and $p_{\perp} = 300$ MeV/c for $\pi^{\pm}$, $K^{\pm}$, and $p/\bar{p}$, and the Peterson fragmentation function with $\epsilon = 0.060$ (0.006) for $c\bar{c}$ ($b\bar{b}$) events. The Lund symmetric (light flavor) fragmentation function differs significantly in shape from the Peterson (heavy flavor) fragmentation function, the latter being much harder. This has important consequences for the determination of the initial event flavor with 'leading' particles, as discussed below.

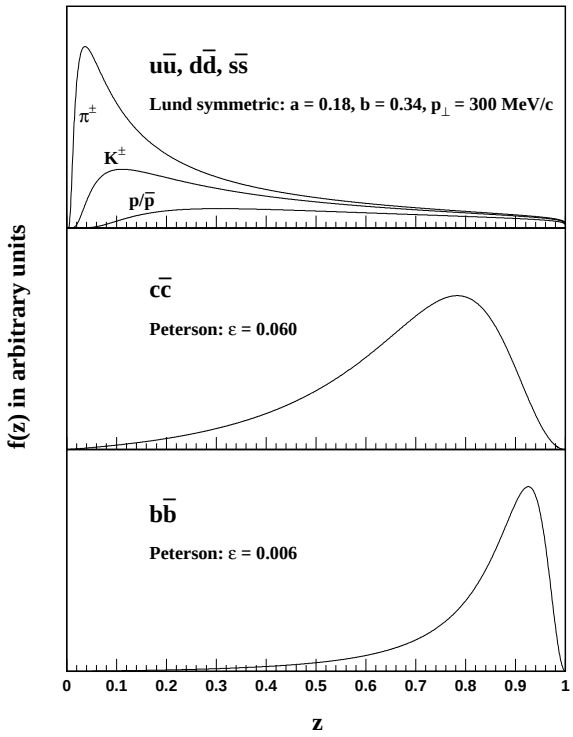

Figure 2.9: The Lund symmetric and the Peterson fragmentation functions for a particular choice of parameters.

2.3.3 Leading Particle Effect

In the fragmentation process of a hadronic event, the primary quark (or anti-quark) is incorporated in a 'leading' particle which may carry a considerable fraction of the energy in the event. The hard fragmentation function for $b\bar{b}$ ($c\bar{c}$) events results in a 'leading' B (D) meson of relatively high energy in each event hemisphere. Very few additional B or D mesons are produced in a heavy flavor event hemisphere. A $b\bar{b}$ final state can be tagged by the presence of a lepton with high momentum transverse to the jet axis or of a decay vertex displaced from the primary interaction point, indicating the presence of a leading B meson in the jet. A $c\bar{c}$ final state can be identified

by exclusive or partial reconstruction of the leading charmed hadron in a hadronic jet.

In contrast, the much softer fragmentation function for light flavor events frequently results in other particles of the same type as the leading hadron, and of roughly simlar energy, to be present in each light flavor ($u\bar{u}$, $d\bar{d}$, $s\bar{s}$) event hemisphere, in addition to the leading hadron. Furthermore, e.g. a leading K^- can be produced in an s jet, as well as in a $\bar{u}$ jet. Thus the determination of light event flavors is significantly more complicated.

Measurements [8; 9] performed at the SLD have demonstrated that light flavored jets can be tagged by the presence of a high-momentum leading identified particle containing a valence quark of the desired flavor. As described in detail in Ref. [9], we may define the normalized difference between hadron and anti-hadron production in light quark (u, d, s) jets:

$$D_h = \frac{R_h^q - R_{\bar{h}}^q}{R_h^q + R_{\bar{h}}^q} \tag{2.31}$$

with the differential cross section per light quark jet:

$$\begin{aligned} R_h^q &= \frac{1}{2N_{events}} \frac{d}{dx_p}(N(q \to h) + N(\bar{q} \to \bar{h})), \\ R_{\bar{h}}^q &= \frac{1}{2N_{events}} \frac{d}{dx_p}(N(q \to \bar{h}) + N(\bar{q} \to h)) \end{aligned} \tag{2.32}$$

where q ($\bar{q}$) represents a light flavor quark (anti-quark) jet, N_{events} denotes the total number of events in the sample, and h ($\bar{h}$) represents any of the identified hadron species π^-, K^-, p, $\bar{K}^{*0}$, Λ^0 (anti-hadrons). E.g., $N(q \to h)$ denotes the number of hadrons of species h in light quark jets. Figure 2.10 shows the D_h distributions for these five hadron species for the 1993-5 SLD data sample.

In each case, D_h is consistent with equal production of hadron and anti-hadron at low x_p.

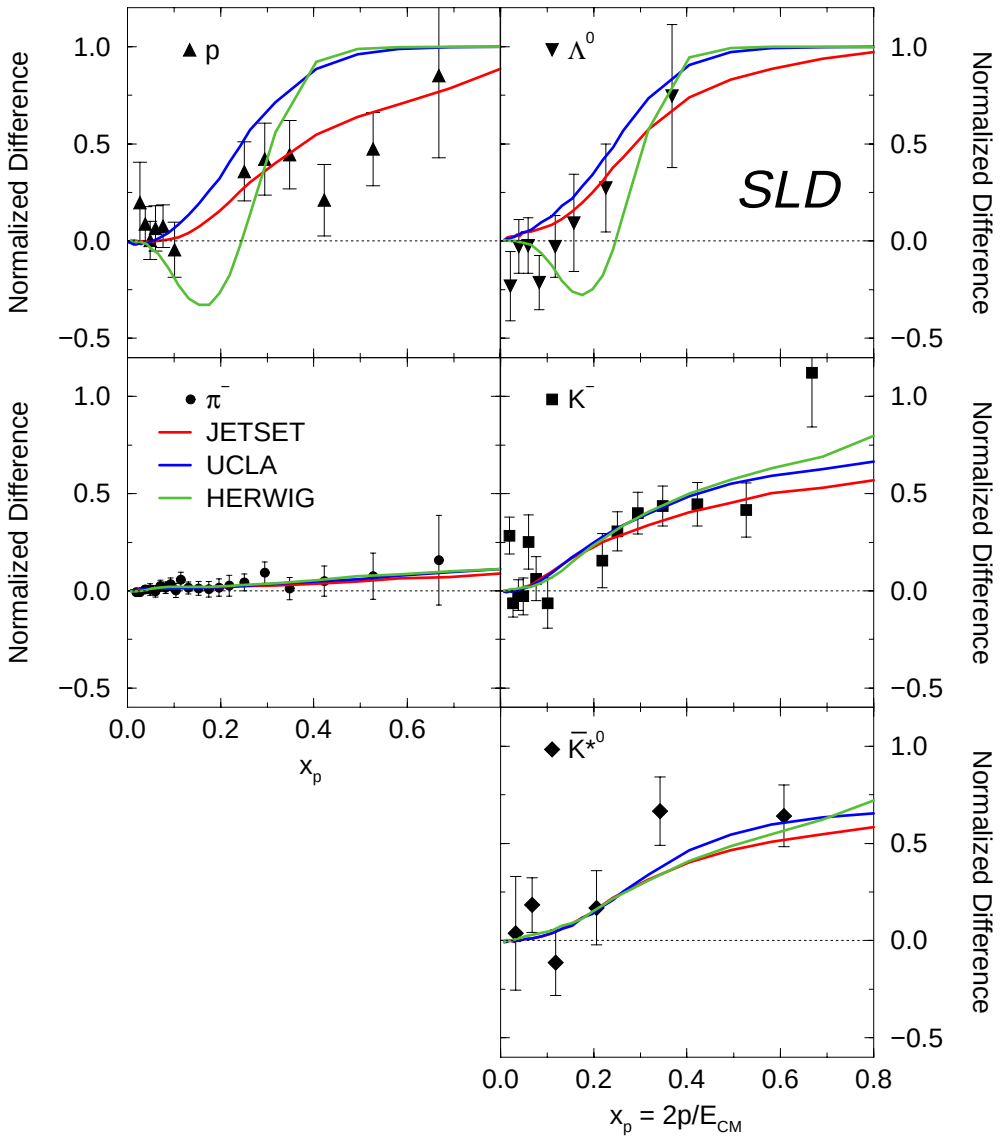

Figure 2.10: Normalized differences between hadron and anti-hadron production in light flavored jets. The data, represented by symbols, are compared to the predictions of three fragmentation models.

For $x_p > 0.2$, the observed excess of p and Λ^0 over $\bar{p}$ and $\bar{\Lambda}^0$ is clear evidence for leading baryon production. Since a meson contains a valence quark and a valence anti-quark, the interpretation of the results for mesons is more complicated. E.g. if a leading $\bar{K}^{*0}$ were produced equally in s and in $\bar{d}$ jets, D would be zero. The two highest-x_p data points for $\bar{K}^{*0}$ are positive, indicating both leading $\bar{K}^{*0}$ production and that more leading $\bar{K}^{*0}$ are produced in s than in $\bar{d}$ jets, as expected from strangeness suppression in the fragmentation process. For $x_p > 0.2$, the data are positive for K^-, and beyond the excess expected due to the different production and forward-backward asymmetry of s quarks compared to $\bar{u}$ quarks. As in the case of $\bar{K}^{*0}$, this indicates both leading particle production and more frequent production of leading K^- in s jets than in $\bar{u}$ jets. The data for π^- are consistent with zero everywhere. This indicates large non-leading pion production, and does not rule out leading pion production. The predictions of three fragmentation models are also shown. The HERWIG 5.8 [44] and UCLA 4.1 [45] predictions for p and Λ^0 rise to unity for $x_p \approx 0.4$ and are inconsistent with the proton data. All three models are consistent with data for the three mesons species. However, the quantification of the total number of observed leading particles remains problematic.

In the A_s analysis presented in this thesis, $s\bar{s}$ events need to be identified. For example, we may use a K^- (K^+) meson to tag an s ($\bar{s}$) jet. However the background from other light flavors (a $\bar{u}$ jet can also produce a leading K^-), decays of B and D hadrons, and nonleading kaons in events of all flavors is large, and neither the signal nor the background have been well measured experimentally. Qualitative features of the leading particle effect have been incorporated in the JETSET 7.4 [46] Monte Carlo model used at the SLD. With the help of the leading particle effect for $K^\pm$ and $\Lambda^0/\bar{\Lambda}^0$ and strangeness suppression in the fragmentation process, $s\bar{s}$ events can be tagged with quite high purity, and the strange quark coupling, A_s, can be measured.

The intuitive experimental approach leading to Figure 2.10 employs the electroweak production

asymmetry in polar angle to tag the quark (and anti-quark) hemisphere in an event. However we intend to determine the coupling A_s from the production asymmetry, so we must use another approach. Rapidity correlations, discussed in Chapter 6, provide a model-independent method to study several features of the hadronization process including leading particles.

Chapter 3

Experimental Apparatus Overview

This chapter presents a brief discussion of the experimental apparatus used in this measurement. The SLAC Linear Collider (SLC) accelerates and collides electrons and positrons at the Z^0 resonance. At the interaction point, collisions are detected within the SLC Large Detector (SLD). Many more details of the SLD are given in Ref. [47], and the SLC is discussed in more depth in Ref. [48]. The chapter concludes with a description of the SLD event trigger which determines when the detector data is recorded and a brief description of the event generation and detector simulation for the SLD.

3.1 SLAC Linear Collider (SLC)

The SLAC Linear Collider (SLC) is a unique single-pass electron positron collider located at the Stanford Linear Accelerator Center (SLAC). Figure 3.1 shows an outline of the SLC which employs an almost 2 mile long linear accelerator (linac) to accelerate both electrons and positrons. The SLC operates at a 120 Hz machine cycle. At the beginning of each cycle, two longitudinally polarized electron bunches, each approximately 1 mm in length and containing about 6×10^{10} electrons, are generated by the polarized electron source. Both bunches are accelerated to 1.19 GeV and stored in the North damping ring. Before entering the damping ring, a spin-rotator magnet rotates the electron spin into the transverse direction in order to preserve the spin during the damping process. The damping makes use of synchrotron radiation to compress the phase space of the bunches. A

similar process occurs for a positron bunch in the South damping ring. The three bunches re-enter the linac and are accelerated by the linac. The positron bunch leads the two electron bunches. The positron bunch and the first electron bunch are accelerated to an energy of 46.7 GeV, and then are separated by dipole bending magnets in the Beam Switchyard into approximately 1 km long arcs. The electron bunch enters the North arc, while the positron bunch goes into the South arc. In the arcs, each bunch looses about 1.1 GeV in energy on the way to the IP due to synchrotron radiation. In addition, the arcs tend to reduce the polarization of the electron beam. Therefore the electron beam polarization is rotated to a specific angle before entering the arc, so that after spin precession in the arc, the electrons arrive at the IP with longitudinal polarization. In the final focus sections, both beams are collimated by superconducting quadrupole magnets before colliding head-on in a micron-sized interaction point (IP) inside the SLD. After passing through the IP both beams are dumped.

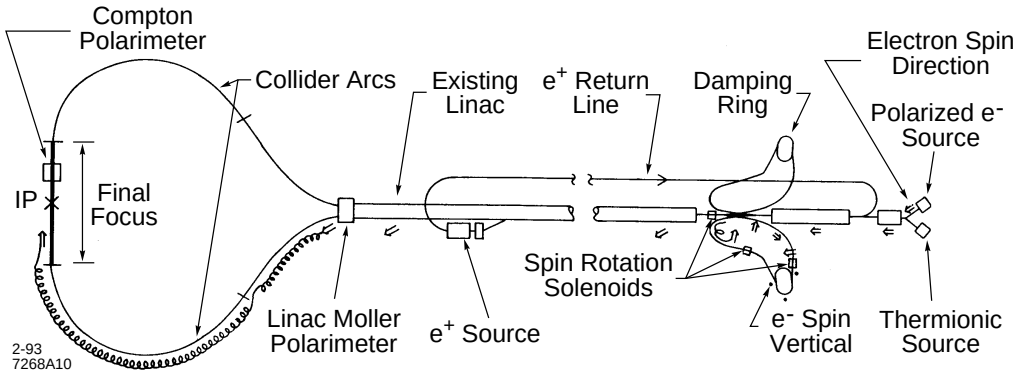

Figure 3.1: Layout of the SLC.

The second of the electron bunches is extracted part way down the linac at an energy of 30 GeV and directed onto a tungsten-rhenium alloy target. An electromagnetic shower consisting of electrons, positrons and photons develops. Positrons are filtered from this shower, transported

back to the front-end of the linac in a separate line, and employed in the next acceleration cyle.

The collimation of the electron beam and positron beam at the IP is very important for achieving sufficient luminosity. Due to a combination of improved beam focussing, enhanced electron and positron bunch populations, and operational experience, the SLC constantly improved the luminosity since it started producing Z^0 in 1989. In the 1992 physics run, peak luminosites reached 30 Z^0/hour, rising to peaks of approximately 60 Z^0/hour and 100 Z^0/hour in the 1993 and 1994-5 run periods, respectively. In the final 1997-8 data run, the luminosity more than doubled again with peaks of well above 200 Z^0/hour. The SLC luminosity history is summarized in Figure 3.2.

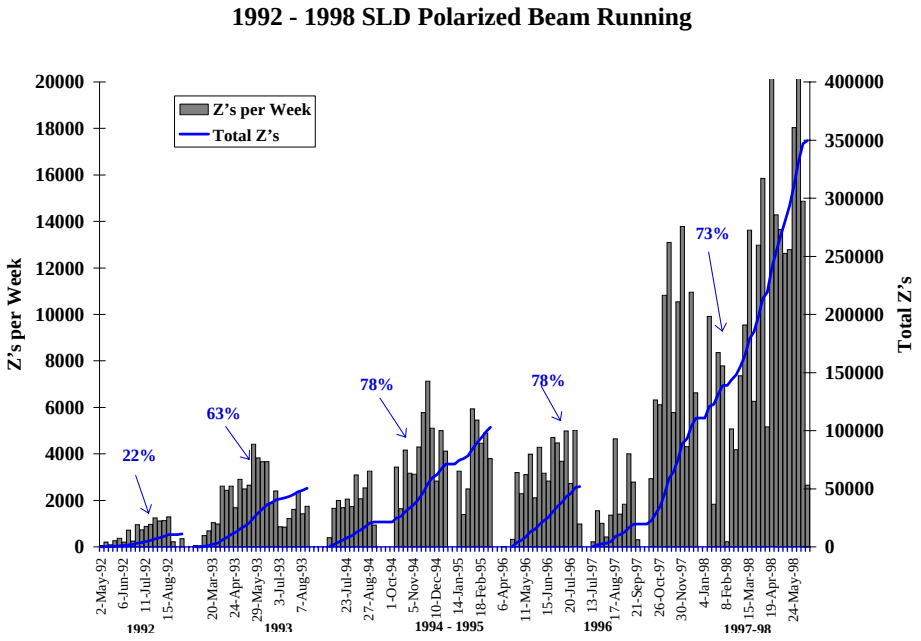

Figure 3.2: SLC/SLD luminosity history. In the 1997-8 data run, the luminosity improved substantially and reached 20,000 Z^0/week.

3.1.1 Polarized Electron Source

An important strength of the SLD is the capability to generate, accelerate and collide longitudinally polarized electrons with unpolarized positrons to produce polarized Z^0 bosons. The electron beam polarization originates from a strained-lattice GaAs photocathode in the electron gun at the linac's electron injector. Circularly polarized light from a Nd:YAG-pumped Ti sapphire laser is employed to selectively excite electron transitions into longitudinally-polarized states in the conduction band of the photocathode. Figure 3.3 shows the electron transitions between the relevant energy levels.

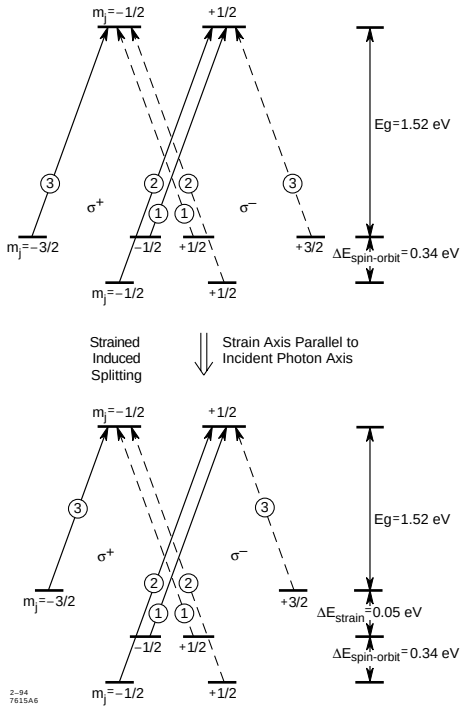

Figure 3.3: Energy state diagram for (top) bulk GaAs and (bottom) the strained GaAs lattice. The encircled numbers denote the relative intensities of the transitions. The strained lattice breaks the degeneracy and allows a theoretical polarization of 100%.

The electron bunch is then accelerated by a 30 kV electric field before injection to the linac. The 1992 physics run made use of a bulk GaAs photocathode whose theoretical maximum polarization of 50% is due to the degeneracy in its valence band as shown in Figure 3.3. Approximately 22%

average polarization was achieved. For the 1993 physics run, a strained lattice photocathode consisting of a 300 nm layer of GaAs deposited on a GaAsP substrate was used. The name for this cathode derives from the difference in the lattice spacings of the two materials, which leads to a strain on the epitaxial GaAs layer. This strain breaks the degeneracy in the valence band, yielding a theoretical maximum polarization of 100%. About 63% average polarization was achieved. For the 1994-5 physics run, the thickness of the epitaxial layer was further reduced to 100 nm, improving the average polarization to 77%. This type of photocathode was retained for the 1996 (1997-1998) physics run, and resulted in an average polarization of 77% (73%).

3.1.2 Energy Spectrometer

The Wire Imaging Synchrotron Detectors (WISRD) [52], located between the IP and each of the beam dumps, measure the energies of the electron and positron beams on a pulse-by-pulse basis. The operational principle of the WISRD is based on the deflection of the beam by two horizontal bend magnets, producing a swath of synchrotron radiation imaged by a multiwire proportional chamber (MWPC). A calibrated vertical bend magnet, deflecting the beam by an angle inversely proportional to its energy, is located between the two horizontal bend magnets. This angle is inferred from the distance between the two radiation swaths. Figure 3.4 shows a schematic view of the WISRD.

During the 1997-8 SLD data taking period, a Z^0 peak scan was performed which allowed the WISRD energy spectrometer to be calibrated against the precise Z^0 mass measurement obtained at LEP. The resulting luminosity weighted mean center-of-mass energy for the 1997-8 data run was determined to be $E_{cm} = 91.237 \pm 0.029$ GeV [53].

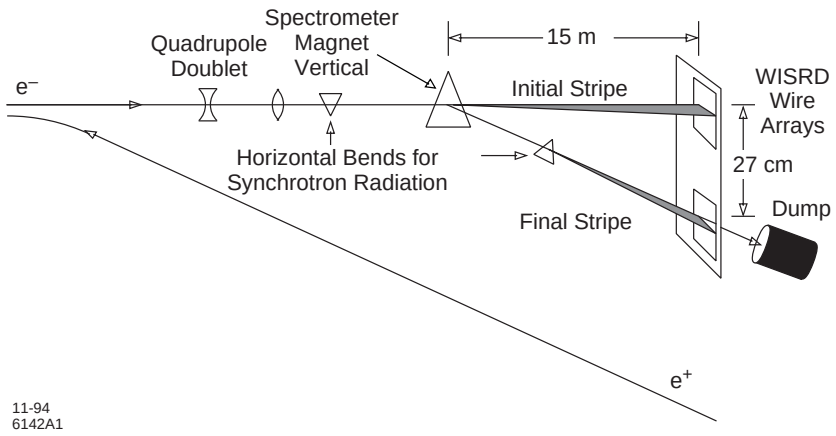

Figure 3.4: Schematic layout of the WISRD. The deflection of the beam is inversely proportional to its energy.

3.1.3 Compton Polarimeter

The electron beam polarization close to the IP is of special interest for electroweak measurements performed at the SLD. The Compton Polarimeter [20] allows the electron beam polarization to be determined by making use of the helicity asymmetry in the Compton scattering cross section. This device consists of a laser with polarizing optics and an electron spectrometer, as shown in Figure 3.5. Photons from a frequency-doubled YAG laser are polarized by a series of Pockels cells and quarter-wave plates and interact with the electron beam before their polarization is determined. Approximately 33 m downstream of the IP, the Compton polarimeter collides 2.33 eV circularly-polarized photons with the electron beam, causing the scattered electrons to lose energy. The electrons traverse a precision dipole magnet separating the scattered electrons from the main bunch. The momentum spectrum of the scattered electrons is determined by measuring their deflection angle with a multi-channel Cherenkov device. The scattered electrons shower in a lead pre-radiator, and the produced particles generate Cherenkov light which is guided to an array of

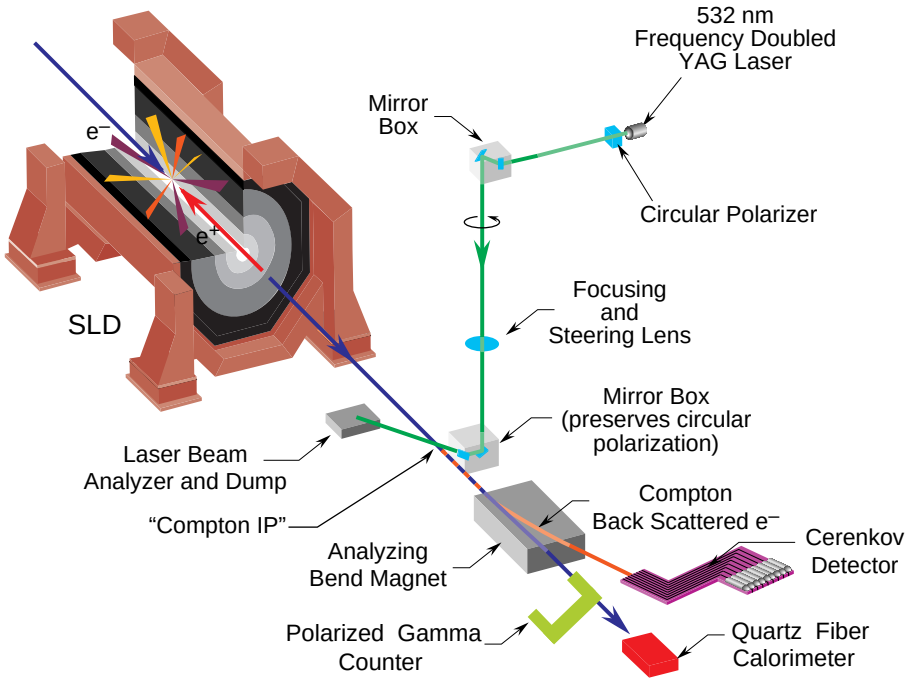

Figure 3.5: Schematic view of the Compton Polarimeter.

photomultiplier tubes.

The differential Compton cross section for the scattering of polarized photons and polarized electrons can be written as:

$$\frac{d\sigma_C}{dE} = \frac{d\sigma_C^u}{dE}[1 + A_{Compton}(E)] \tag{3.1}$$

where E denotes the energy of the scattered electron, and $\frac{d\sigma_C^u}{dE}$ is the unpolarized differential Compton cross section. The unknown electron beam polarization, P_e, can be determined from the Compton asymmetry, $A_{Compton}(E)$, measured in the $J_z = 3/2$ and $J_z = 1/2$ cross sections:

$$A_{Compton}(E) = \frac{\sigma_{J_z=\frac{3}{2}} - \sigma_{J_z=\frac{1}{2}}}{\sigma_{J_z=\frac{3}{2}} + \sigma_{J_z=\frac{1}{2}}} = P_e P_\gamma a_C(E) \tag{3.2}$$

where P_γ is the known photon polarization, and the "analyzing power" for Compton scattering,

i.e. the dilution of the measured Compton cross section asymmetry, is given by $a_C(E)$, which is determined form the theoretical cross section using information from a calibration process [54]. Since $A_{Compton}(E)$ can be calculated precisely from QED, the precision of the Compton Polarimeter is limited only by detector systematics.

Since the polarization measurement occurs about 33 m downstream from the SLC IP, the measured polarization at the Compton IP shows a systematic difference from the luminosity-weighted polarization at the SLC IP due to chromatic terms in the SLC final focus optics and the energy dependence of the spin-precession in the SLC arcs. The average luminosity-weighted polarizations [49] at the SLC IP for the different physics run periods, together with their uncertainties, are summarized in Table 3.1.

Table 3.1: Summary of average electron beam polarizations for the different physics run periods.

Run period	Average polarization P_e
1992	0.224 ± 0.006
1993	0.626 ± 0.012
1994-5	0.772 ± 0.005
1996	0.765 ± 0.005
1997	0.733 ± 0.008
1998	0.731 ± 0.008

Two additional detectors, the Polarized Gamma Counter (PGC [50]) and the Quartz Fiber Calorimeter (QFC [50]), are used to measure the electron beam polarization. Both devices provide cross checks of the Compton Polarimeter result with a precision of better than 1%. Finally, we expect the polarization of the positron beam to be zero. The measurement of the positron beam polarization with the Moller Polarimeter [51] in SLAC End Station A yields $P_{e^+} = (-0.02 \pm 0.07)\%$, i.e. consistent with zero.

3.2 SLC Large Detector (SLD)

The SLD [47] was proposed in 1984 to be a general purpose detector with almost 4-π steradian solid angle coverage. It surrounds the SLC IP and replaced the less sophisticated Mark II detector. Figure 3.6 and Figure 3.7 show the layout of the SLD. The cylindrical, concentric geometry is characteristic of modern detectors at collider facilities. The central "barrel" portion of the SLD is about 10 m in length with a radius of approximately 4.5 m, closed off by "endcaps" at either face of the cylinder. Each layer of the detector contains a separate sub-detector used to record different aspects of the collision products. The sub-division into layers is similar for the barrel and the endcaps. The beampipe and its support structures lead to a 98% solid angle coverage. Following from the IP radially outward, we encounter the CCD-based vertex detector (VXD2, VXD3) and the wire drift chamber (CDC) allowing precise charged particle tracking, the Cherenkov Ring Imaging Detector (CRID) for charged particle identification, the Liquid Argon Calorimeter (LAC), the 0.6 T conventional solenoid serving as the outer support structure, and the Warm Ion Calorimeter (WIC) used for muon identification.

The following discussion presents more details on the operational principles of each sub-system, with the barrel detectors taking preference since they are better understood than the endcaps, and more important to the analysis in this thesis. Depending on the sub-system, the barrel covers roughly 2/3 of the available solid angle.

In the standard SLD coordinate system, the z axis points towards geographic north along the positron beam direction, and the x and y axes lie in the plane perpendicular to the beams. The horizontal x axis points west and the vertical y axis points upwards. When using cylindrical coordinates, the radius r is defined in the x, y plane; the polar angle θ and the azimuthal angle ϕ are defined with respect to the positive z axis and x axis, respectively.

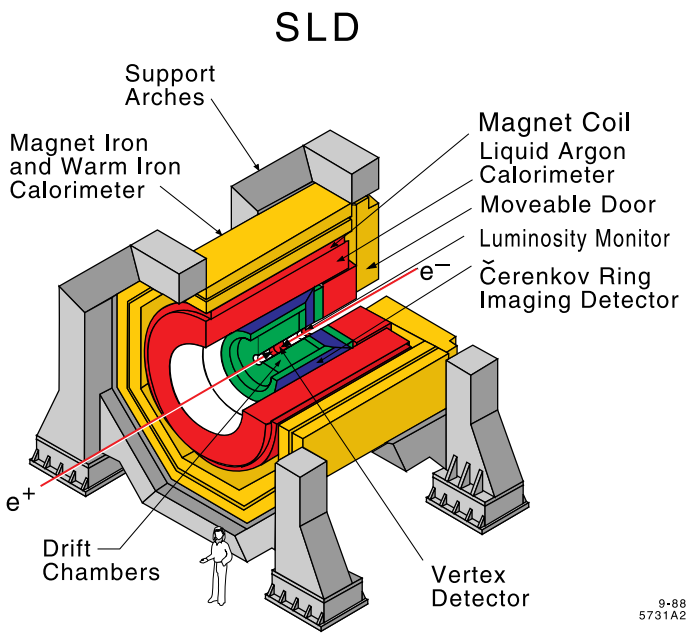

Figure 3.6: The SLD in isometric view showing the cylindrical layout of the sub-detectors. The Luminosity Monitor is not shown, and the encaps have been omitted for clarity.

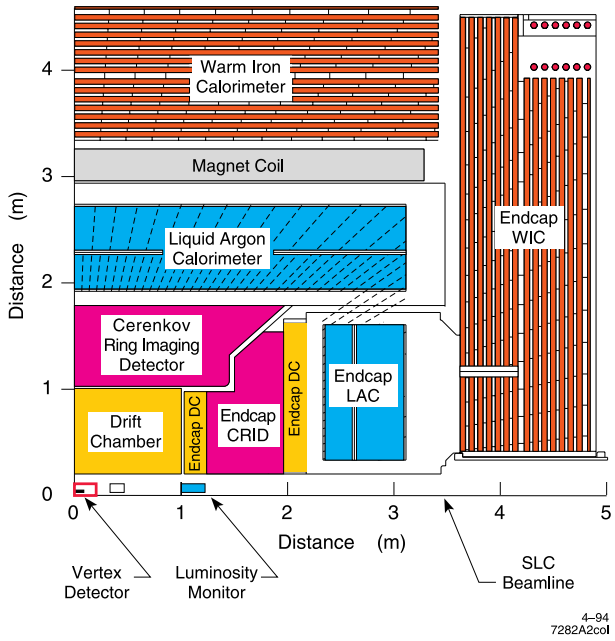

Figure 3.7: The SLD in quadrant view. The dimensions are indicated.

3.2.1 Luminosity Monitor (LUM)

The SLD Luminosity Monitor (LUM) [55] provides a precise measurement of the luminosity by measuring small-angle Bhabha scattering whose cross section is derived from QED. In addition, it was designed to extend the coverage of electromagnetic calorimetry down to small angles. The LUM, shown in Figure 3.8, is positioned 1 m downstream from the IP and consists of two silicon-tungsten calorimeter modules, the Luminosity Monitor/Small Angle Trigger (LMSAT) and the Medium Angle Silicon Calorimeter (MASiC), providing polar angle coverage from 28 mrad to 68 mrad, and from 68 mrad to 200 mrad, respectively. The projective towers in both calorimeters are highly segmented. Using Bhabha events, an energy resolution of about 3% at 50 GeV has been achieved with the LUM.

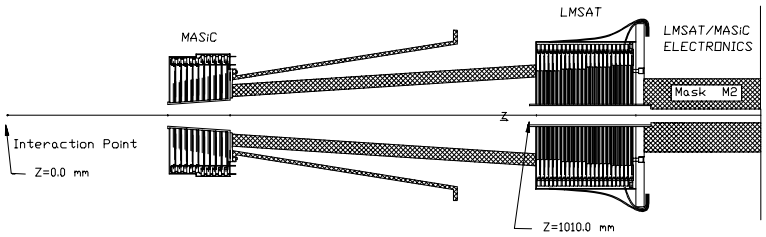

Figure 3.8: The SLD luminosity monitor, showing the MASiC, the LMSAT and masks.

3.2.2 Vertex Detectors (VXD2 and VXD3)

The SLD vertex detector [56] provides precision vertexing by making use of charged coupled devices (CCD) to detect the charge deposition caused by traversing charged particle tracks. Two devices were used over the lifetime of the experiment. VXD2 and VXD3 were operational during the 1993-5 and 1996-8 run periods, respectively.

VXD2 is illustrated in Figure 3.9. The outer layer of the beryllium beam pipe is at 25 mm, limiting the innermost VDX2 layer to 29.5 mm. The outer VXD2 layer is located at 41.5 mm from

the IP. VXD2 consists of 480 CCDs located on sixty aluminum-ceramic ladders, each 9.2 cm long, held in place by a beryllium shell and arranged in four concentric layers, parallel to the beam axis. Eight CCDs are located on each ladder, with 4 CCDs mounted on each side. Each CCD covers about 1 cm^2 and contains 375×578 (22 μm)^2 pixels. On average, 2.3 pixel hits are recorded per charged track passing through the detector.

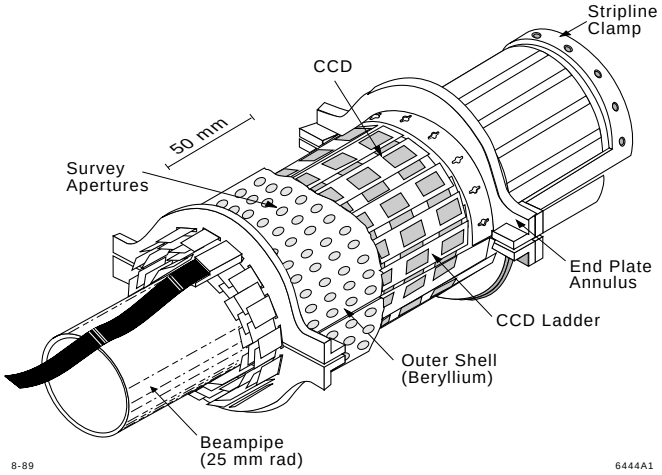

Figure 3.9: The SLD vertex detector VXD2.

Due to advances in CCD technology, the individual CCDs for VXD3 cover about 13.6 cm^2 and contain $4,000 \times 800$ (20 μm)^2 pixels, permitting a three-layer device with just 96 CCDs. Figure 3.10 and Figure 3.11 compare the geometrical layout of VXD2 and VXD3. The individual layers in VXD3 are fully overlapping. In addition, VXD3 provides 3-hit acceptance up to $|\cos\theta| < 0.85$ that allows stand-alone tracking. VXD2 provides $|\cos\theta| < 0.75$ acceptance with only two hits. The vertex detector is operated at about 190 K to suppress dark currents. Each CCD is read out serially in 160 ms and in 120 ms for VXD2 and VXD3, respectively.

The CCDs and ladders for VXD2 and VXD3 were optically surveyed to a precision of about 10 μm. The single hit resolution of VXD2 was determined from 3-hit tracks ("triplets"). The residual between the projected position, using the inner and outer hit, and the hit in the middle

layer, is shown in Figure 3.12. The single hit spatial resolutions of 5.6 μm in $r\phi$ and 5.5-9 μm in rz for VXD2 and 3.8 μm in $r\phi$ and 4.2 μm in rz for VXD3 were achieved after correcting for the inner and outer hit resolution. The xy miss-distance in $Z^0 \to \mu^+\mu^-$ events yielded an impact parameter resolution for VXD2 of about 11 μm in $r\phi$ and 38 μm in rz [57], and 7.8 μm in $r\phi$ and 9.7 μm in rz for VXD3 [58].

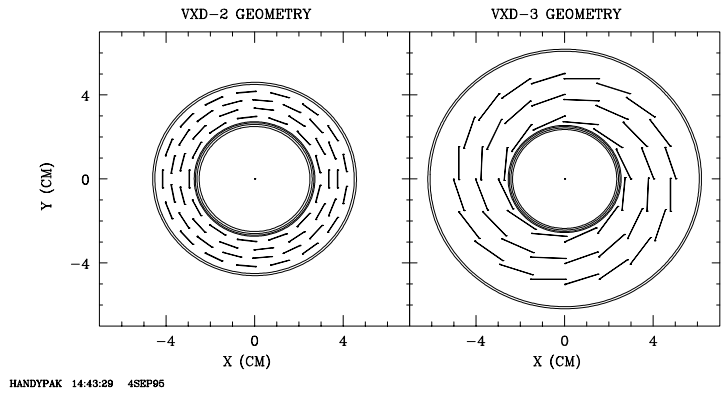

Figure 3.10: Comparison of VXD2 and VXD3, viewed in the $r\phi$ plane. VXD3 features overlapping layers and a longer lever arm.

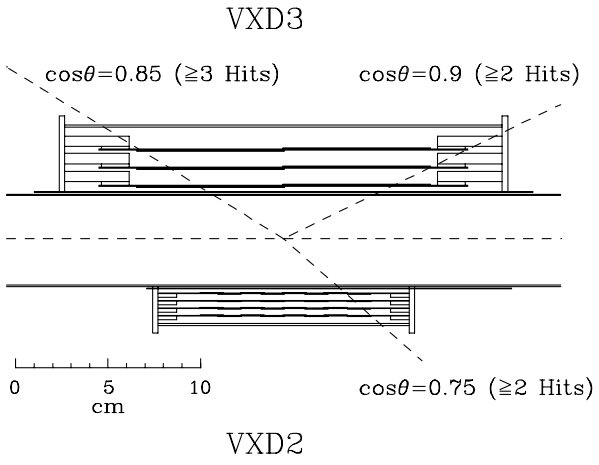

Figure 3.11: Comparison of VXD2 and VXD3, viewed in the rz plane. VXD3 provides improved coverage in polar angle.

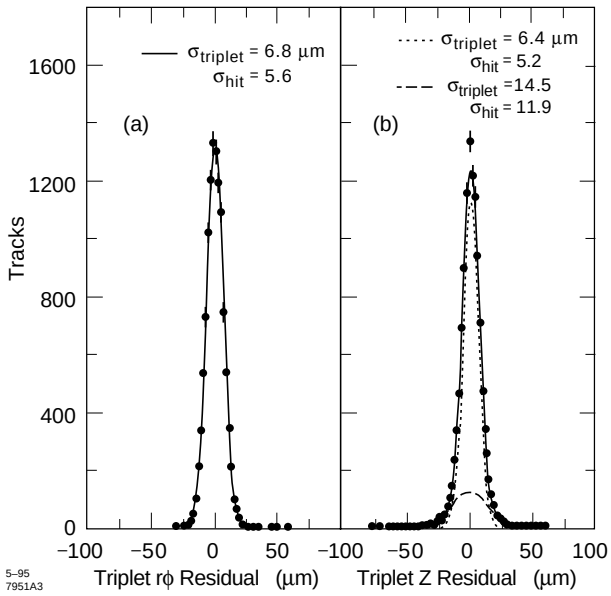

Figure 3.12: The VXD2 single hit resolution, determined from triplets, in (a) the $r\phi$ plane and (b) the rz plane.

3.2.3 Drift Chambers (CDC and ECDC)

The Central Drift Chamber (CDC) [59] and the Endcap Drift Chambers (ECDC) are the two separate SLD drift chamber sub-systems. The CDC is the primary SLD tracking device. It is immersed in a uniform solenoidal field of 0.6 T, and occupies an annulus of 200 cm in length, 20 cm in inner radius and 100 cm in outer radius. The inner and outer walls consist of an aluminum sheet-Hexcell fiberboard laminate, entailing $1.8\%X_0$ ($1.6\%X_0$) for the inner (outer) wall. The endplates are constructed from aluminum. The drift cells in the CDC are arranged in 10 staggered superlayers, as shown in Figure 3.13. The sense wires in the superlayers are either axial or have a 41 mrad stereo angle with respect to the beam axis. The wire layout – 8 sense wires, 18 guard wires, and 25 field wires – for a cell, measuring about 6 cm by 5 cm high, is displayed in Figure 3.14. The sense wires consist of 25 μm gold-coated tungsten, and the guard and field wires are made of 150 μm gold-coated aluminum.

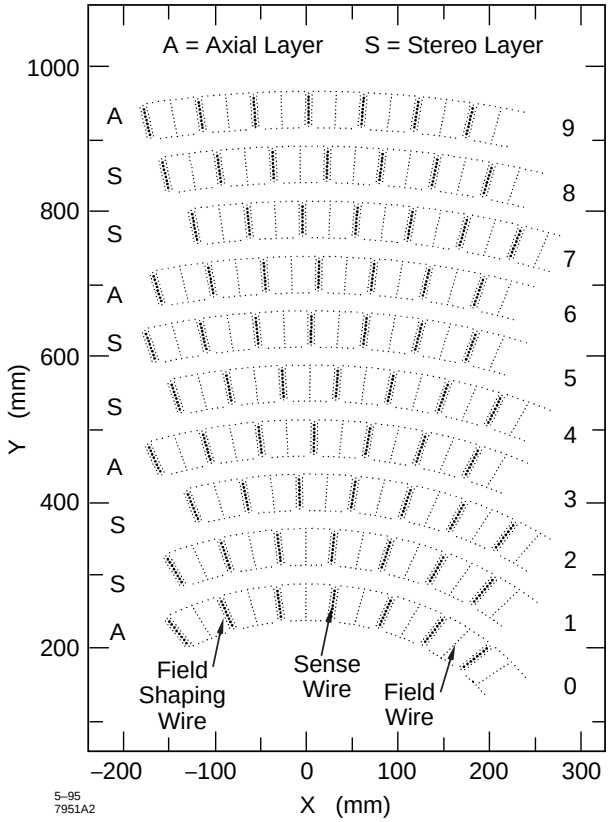

Figure 3.13: Endplate view of the CDC, showing the arrangement of the axial (A) and stereo (S) superlayers.

The drift gas in the CDC consists of 75% CO_2, 21% Ar, 4% isobutane, and 0.2% H_2O. Properties of this mixture are: low drift velocity and low diffusion, provided by CO_2, improve the spatial resolution; Ar increases the avalanche gain; isobutane helps quenching; the admixture of H_2O helps suppress wire aging [60]. The mean drift field of 0.9 kV/cm leads to a drift velocity of 7.9 μm/ns in the gas.

When a charged track passes through the cells, a trail of ions is produced in the drift gas. The drift field directs the liberated electrons towards the sense wires, as shown in Figure 3.15. The hit position is given by the wire address, drift time information, and charge division along the wire. Together with information from the other sense wires in the same cell, a vector hit is formed. Since

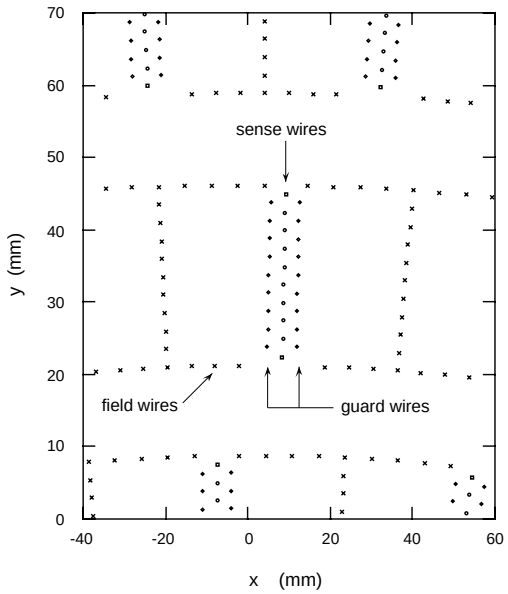

Figure 3.14: Schematic view of the CDC cell layout.

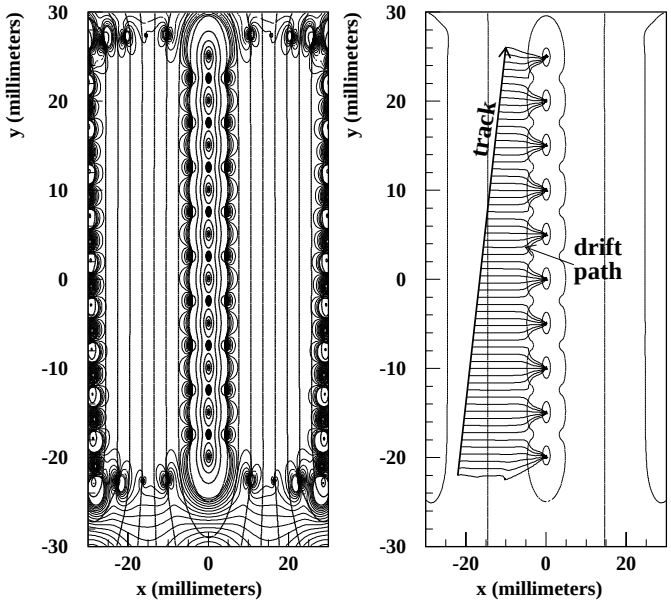

Figure 3.15: Field map for a CDC cell, showing (left) the field configuration for a cell and (right) the drift paths of liberated electrons caused by a charged particle traversing the cell.

the sense wires in one cell are not staggered, an ambiguity in the form of a mirror image arises. A pattern recognition program combines the vector hits from adjacent cells into track candidates. The individual wire hit information is then used to perform a detailed fit, using the more precise z information from the stereo layers, and taking into account electric and magnetic field variations, and energy loss of the track. Details of the track reconstruction algorithms can be found in Ref. [61]. After alignment [62], the momentum resolution for the CDC has been determined to be $(\sigma_{p_\perp}/p_\perp)^2 = 0.010^2 + (0.0050 p_\perp)^2$ where $p_\perp$ is the track momentum transverse to the beam axis in GeV/c. The first term denotes the uncertainty arising from multiple scattering, and the second term the measurement error [59; 63]. The momentum resolution improves to $(\sigma_{p_\perp}/p_\perp)^2 = 0.0095^2 + (0.0026 p_\perp)^2$ when the vertex detector hit information is added to the fit [64].

3.2.4 Cherenkov Ring Imaging Detector (CRID)

The barrel portion of the Cherenkov Ring Imaging Detector (CRID) [65] allows efficient charged particle identification over a wide momentum range, so is crucial to the A_s measurement and will be described in more detail in Chapter 4.

The operating principle of the CRID is based on the Cherenkov effect. Charged particles traversing a dielectric medium with a velocity exceeding the phase velocity of light in that medium emit a coherent wave front of Cherenkov photons. The emission angle, θ_C, to the track is given by $\cos\theta_C = \frac{1}{\beta n}$ where n denotes the index of refraction and the particle's velocity, v, occurs in $\beta = v/c$. The Cherenkov photons are imaged on an array of Time Projection Chambers (TPCs), filled with C_2H_6 gas and an admixture of the gaseous photocathode additive tetrakis-dimethylamino-ethylene (TMAE). Photons with an energy greater than 5.4 eV ionize TMAE which releases photoelectrons into the drift gas. These photoelectrons drift to the instrumented ends of the TPCs. The conversion position can be inferred from the drift time, the wire address,

and the charge division on the wire. The ring of reconstructed photoelectrons allows the velocity of the particle to determined. Together with the momentum measurement provided by the CDC, the five charged particle candidates $e^{\pm}, \mu^{\pm}, \pi^{\pm}, K^{\pm}, p/\bar{p}$ can be distinguished.

3.2.5 Liquid Argon Calorimeter (LAC)

The Liquid Argon Calorimeter (LAC) [66] provides energy measurements of charged and neutral particles. It follows the general detector partition into barrel and endcaps. The barrel extends radially from 1.8 m to 2.9 m, proving coverage between 35^o and 145^o in the polar angle. The encaps extend the coverage down to 8^o. About 98% of the solid angle is covered by the LAC. The LAC is a lead-argon sampling calorimeter consisting of lead plates immersed in liquid argon. The lead plates induce particle showers and collect the charge caused by charged particles ionizing argon as they pass through it. The lead consists of alternating layers of grounded plates and tiles held at -2 kV, separated by plastic spacers and immersed in liquid argon. Several tiles from adjacent layers form projective towers, covering about 33 mrad in polar angle and azimuth. These are connected to amplifiers to measure the charge deposited. The LAC is segmented into four radial layers denoted EM1, EM2, HAD1, and HAD2. The naming convention is related to the primary role of the sections. In the EM sections, the 2.0 mm thick lead plates are separated by 2.75 mm Ar gaps. The HAD sections consist of 6.0 mm thick lead plates with identical Ar gap size. The first two layers, EM1 and EM2, contain most of the energy from electromagnetic showers in 21 radiation lengths of material. The outer two layers, HAD1 and HAD2, extend the containment to hadronic showers in 2 absorptions lengths of material. The EM and HAD sections combined contain 49 radiation lengths and 2.8 absorptions lengths of material. Figure 3.16 shows a schematic view of the LAC modules. About 99% of the energy of a 45 GeV electron is contained in the EM sections, and 90-95% of the total energy of a hadronic Z^0 decay [67] is contained by the entire

LAC. The energy resolution [64; 66] for the LAC is approximately $15\%/\sqrt{E}$ for electromagentic showers and $60\%/\sqrt{E}$ for hadronic showers, with the energy E given in GeV.

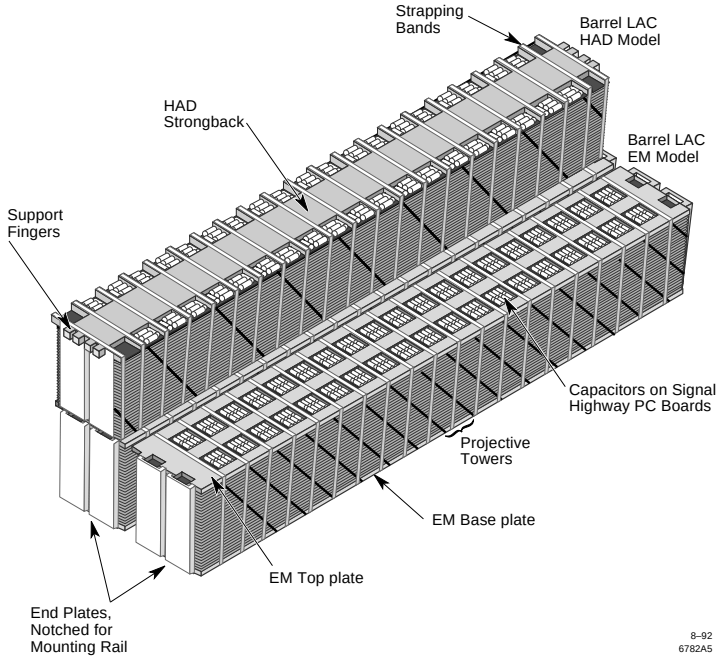

Figure 3.16: EM and HAD modules in the barrel LAC.

3.2.6 Warm Iron Calorimeter (WIC)

The Warm Iron Calorimeter (WIC) [68] serves multiple roles. Primary roles are the flux return for the solenoid and the structural support for the SLD, also it has been instrumented to provide muon identification and additional calorimetry information. The intent to use the WIC for containing the 5-10% energy from hadronic showers leaking through the LAC was not realized due to problems in the calibration of its energy response. The WIC is constructed from 18 layers of Iarocci streamer tubes [69] contained in 3.2 cm gaps between 5 cm thick steel plates. Figure 3.17 illustrates a section of the WIC. The Iarocci tubes are long, rectangular plastic extrusions with central copper-beryllium anode wires, and filled with 88% CO_2, 9.5% isobutane, and 2.5% Ar. The tubes feature

external copper cathode readouts, square readout pads for calorimetric measurements, and long strips for muon tracking, arranged in separate, perpendicular arrays.

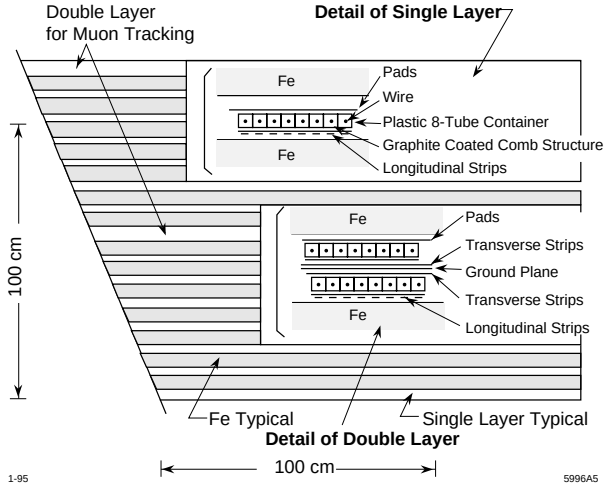

Figure 3.17: Cutaway view of a WIC section, including details of single layers and double layers.

3.3 SLD Event Trigger

The 8.3 ms SLC beam crossing time simplifies the design of data trigger techniques which decide if data should be recorded to tape. The data acquisition at the SLD utilizes a FASTBUS architecture. Data from the various detector sub-systems reach "slave" modules, which depend on the sub-system being read out via fiber optics connections. The slave modules process data from the sub-systems, as summarized in Table 3.2.

The data from these slave modules is pooled in ALEPH event builder (AEB) modules [72] which, as the name implies, assemble complete data events by combining the data from each sub-system. A dedicated trigger AEB performs the data triggering. The trigger criteria are given in more detail in Ref. [70; 71] and are summarized below. Except for the Bhabha trigger, all sub-systems of the detector are written out when a trigger occurs.

Table 3.2: The slave modules for the different detector sub-systems.

Detector sub-system	Slave module
VXD2 and VXD3	Vertex Data Acquisition (VDA)
CDC and CRID	Waveform Sampling Module (WSM)
LAC	Calorimeter Data Module (CDM)
WIC	Digital Readout Module (DRM)

- Energy trigger: requires at least 8 GeV of total deposited energy in the EM and/or HAD calorimeter towers in the LAC. Only towers above the threshold of 60 (120) ADC counts for EM (HAD) towers, corresponding to 246 MeV (1.298 GeV), contribute.

- Tracking trigger: occurs if at least 2 charged tracks, separated by at least 120^o, pass through at least 9 superlayers of the CDC. In addition, the CDC cells hit by these tracks must match a configuration in a pre-calculated CDC cell pattern map. A CDC cell hit is recorded if at least 6 of its 8 sense wires record pulses above threshold. The pattern map contains all possible trajectories of charged tracks above $p_\perp > 250$ MeV/c.

- HAD trigger: combines the first two triggers by requiring one track traversing at least 9 CDC superlayers and some energy deposition in the LAC.

- Muon trigger: one charged track with 9 CDC superlayers hit and calorimetric hits in the opposite WIC octant satisfy this trigger.

- WAB trigger: enables the recording of wide angle Bhabha events by requiring two charged back-to-back tracks in the CDC. Even short track pieces, dismissed by the tracking trigger, may satisfy this requirement.

- Bhabha trigger: requires at least 12.5 GeV of total energy in both the north and south EM2

sections of the LUM. Background splashes on the luminosity monitor do not trigger detector readout.

- Random trigger: occurs every 20 seconds. This trigger writes out data for background studies, independent of the status of other triggers.

The software controlling data taking at the SLD runs on a Digital Equipment Corporation VAX/VMS computer cluster. Data is written to tape via fiber optic connections to a silo located in the SLAC computing center. A typical SLD event is roughly 250-300 kbytes. About 40%, 25%, and 25% in size is contributed by the CRID, the drift chambers, and the VXD, respectively. Background conditions, varying with the tuning of the SLC, have a strong impact on the event size. Typical trigger rates were about 0.2 Hz (0.5 Hz) for the 1993-6 (1997-8) data taking periods under low background conditions. It is estimated that the combined efficiency for the three hadronic triggers (Energy, Tracking, HAD) exceeds 96% [70] for accepting hadronic events.

3.4 SLD Monte Carlo

Modern Particle Physics experiments rely on detailed Monte Carlo simulations to model both, underlying physical processes and the detector response. The simulation process consists of two steps. The generation of simulated events starts with the production of generator level events, followed by a full detector simulation of the SLD detector response.

The JETSET 7.4 [46] event generator, based on the LUND fragmentation model with parameters tuned to hadronic e^+e^- annihilation data [73], was used to generate the 1994-8 SLD Monte Carlo. JETSET 6.3 was used for the 1993 SLD Monte Carlo, with similar tuning. For c and b quarks, the Peterson fragmentation function [74] was employed, and the B hadron decay model [64; 75] developed at SLD was tuned to ARGUS [76] and CLEO [77] data. In the next step, acceptance,

efficiency, and resolution effects are modeled in a detailed Monte Carlo simulation of the detector. The SLD utilizes the standard GEANT 3.21 [78] package which tracks particles through the various sub-detectors, accounting for e.g. the magnetic field, scattering, and energy loss. The description of the showering in calorimeters is based on GEANT EGS4 [79] and GEANT GHEISHA [80] for electromagnetic and hadronic interactions, respectively. Random trigger data are overlaid with the results of the simulation to simulate both, beam-related backgrounds and electronic noise in the hardware, in the real data. Finally, simulated data and real data are processed by the same SLD reconstruction package.

The detailed simulations of tracking [61], calorimetry [55; 67], and CRID response [6] give confidence that the detector response is properly modeled. Inclusive distributions of single-particle and event-topology observables in hadronic events are found to be well described by the SLD simulation [71].

Chapter 4

Particle Identification with the SLD CRID

The SLD Cherenkov Ring Imaging Detector (CRID) [47; 65], provides the SLD with efficient particle identification which is an important feature of the A_s measurement. In this chapter, the operational principles of the CRID are described in more detail. A more thorough discussion of ring imaging detectors can be found in Ref. [81]. Here, we describe some general properties of Cherenkov radiation and Cherenkov ring imaging with the CRID, and describe the alignment process performed by the author. We conclude with an overview of the CRID performance in particle identification.

4.1 Principles of Cherenkov Ring Imaging

Charged particles travelling through a dielectric medium at a velocity exceeding the phase velocity of light in that medium emit photons in a coherent wave front, similar to a shock wave in hydrodynamics. This radiation was discovered by Cherenkov [82] in 1934, and explained within classical electrodynamics in 1937 by Frank and Tamm [83]. In 1940, Ginzburg [85] provided the quantum mechanical calculation which entailed only small further modifications.

The Cherenkov photons are emitted continuously in conical sheets at an angle of θ_C to the direction of travel of the charged particle:

$$\cos\theta_C = \frac{1}{\beta n} \tag{4.1}$$

where $\beta = v/c$ denotes the normalized velocity of the particle, and n is the index of refraction of the medium. This relation implies that the particle must exceed a threshold velocity, $\beta_{thres} = 1/n$, equivalent to a threshold momentum, $p_{thres} = mc/\sqrt{n^2-1}$, to radiate.

The number of Cherenkov photons, dN, in the photon wavelength interval, $d\lambda$, is given by the Frank-Tamm relation [83; 84]:

$$\frac{dN}{d\lambda} = \frac{2\pi}{\lambda^2}\alpha z^2 L \sin^2\theta_C \tag{4.2}$$

in terms of α, the electromagnetic fine structure constant, L, the path length of the particle, and ze, the charge of the particle, where e denotes the electron charge. This relation shows that for constant n, Cherenkov photons are predominantly produced at short wavelengths. The number of photons detected by a Cherenkov device with detection efficiency $\epsilon(\lambda)$ is:

$$N_{det} = 2\pi\alpha z^2 L \int_{\Delta\lambda} \frac{\epsilon(\lambda)}{\lambda^2}\left[1 - \frac{1}{\beta^2 n^2(\lambda)}\right] d\lambda \tag{4.3}$$

where the wavelength dependence for n indicates a dispersive medium. For approximately constant n, i.e. away from absorption bands, the number of detected photons is $N_{det} = N_o z^2 L \sin^2\theta_C$, with $N_o = 2\pi\alpha \int_{\Delta\lambda}(\epsilon(\lambda)/\lambda^2)d\lambda$ describing the response of the Cherenkov detector.

In 1960, Roberts [86] first proposed the principle of Cherenkov ring imaging which is based on focusing of the conical Cherenkov sheets into a focal plane, and using the radius of the Cherenkov ring, together with the measured momentum, for particle identification. The first useful device was built in 1977 by Séguinot and Ypsilantis [87], employing an admixture of benzene as photosensitive substance in a gas-filled multiwire proportional chamber. Thus detectors of larger size, capable of resolving single photons with good spatial resolution, became feasible. Further progress followed with the advent of improved photosensitive materials, able to shift the sensitivity down to the dominant UV photon energies, such as TMAE (tetrakis-dimethylamino-ethylene [88]), and the use

of time projection chambers (TPCs) with transparent windows. Both the DELPHI RICH [89] and the SLD CRID [47] share a similar design, and represent the first large scale use of Cherenkov ring imaging technology in multi-purpose collider detectors.

4.2 SLD CRID Design

The CRID consists of barrel and endcap systems. The barrel CRID, shown in Figure 4.1, utilizes two Cherenkov radiators. The liquid C_6F_{14} radiator is contained in 40 quartz-windowed trays of 1 cm liquid thickness. The gaseous radiator, consisting of 85% C_5F_{12} and 15% N_2, is 40 cm thick. The 40 quartz-windowed TPCs contain C_2F_6 with an admixture of 0.1% TMAE. Cherenkov photons from the liquid radiator pass directly into the TPC, whereas the photons from the gas radiator are focused by an array of 400 spherical mirrors into rings on the TPCs. The endcap CRID, depicted in Figure 4.2, uses only the gaseous C_4F_{10} radiator. Each endcap CRID contains 5 TPCs, filled with 85% C_2H_6, 15% CO_2 and a 0.1% TMAE admixture, and 60 mirrors. Each endcap TPC is quartz-windowed at only one side.

The barrel CRID allows particle identification in the region $|\cos\theta| < 0.68$, and the endcap CRIDs were designed to cover $0.82 < |\cos\theta| < 0.98$. In both the barrel and endcap CRID TPCs the Cherenkov photons ionize the TMAE, and the photoelectrons are drifted to multiwire proportional chambers (MWPC) located at the outer end of the TPCs.

Due to problems in the endcap tracking, the endcap CRID could never show its full physics potential. Therefore we focus exclusively on the barrel CRID in the following sections. Details on the hardware perfomance of the endcap CRID can be found in Ref. [5; 7; 90].

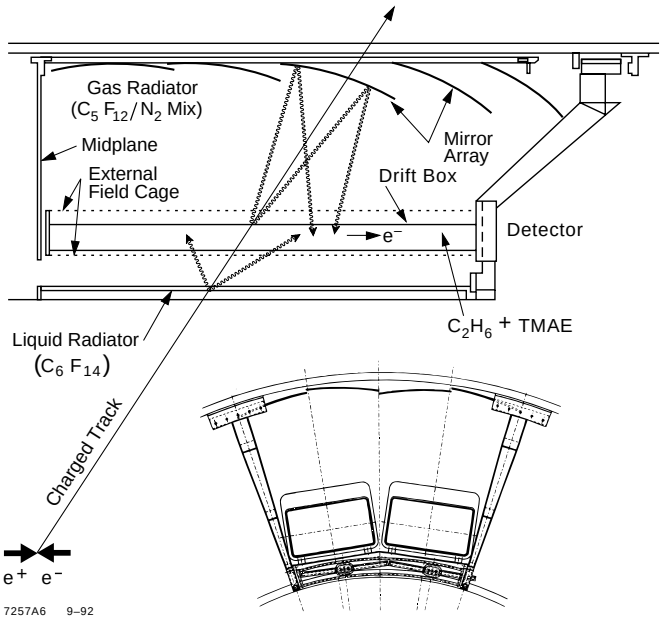

Figure 4.1: The barrel CRID, showing one sector in (top) axial view and (bottom) transverse view.

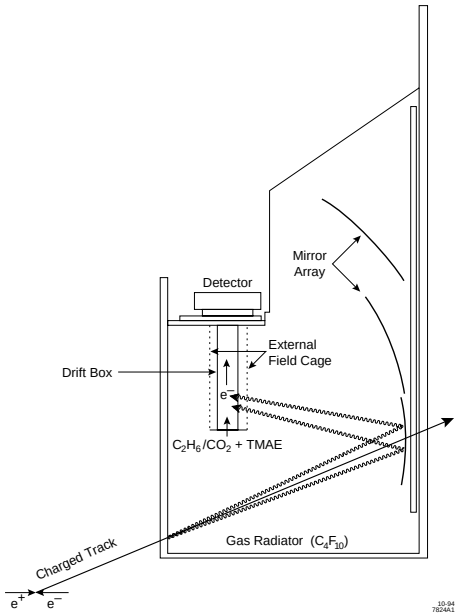

Figure 4.2: One endcap CRID sector in axial view.

4.2.1 Cherenkov Radiators in the Barrel CRID

In order to provide particle identification over a large momentum range, a combination of two different radiator materials, the liquid C_6F_{14} and the gaseous C_5F_{12}/N_2, were chosen for the barrel CRID. The liquid (gaseous) radiator covers the lower (higher) momentum region. These materials were selected for their refractive indices, providing coverage in particle identification with minimum momentum gap, their transmission in the relevant UV wavelengths, relatively low chromatic dispersion, and compatibility with other CRID materials. The liquid C_6F_{14} and gaseous C_5F_{12}/N_2 radiators feature indices of refraction of $n_{liq} = 1.2723$ [91] and $n_{gas} = 1.0017$ [92], respectively, at $\lambda = 190$ nm. Figure 4.3 illustrates the Cherenkov angle curves for $\pi^{\pm}$, $K^{\pm}$ and $p/\bar{p}$ as a function of momentum for the two radiators. The momentum thresholds for the 5 charged particle candidates $e^{\pm}$, $\mu^{\pm}$, $\pi^{\pm}$, $K^{\pm}$ and $p/\bar{p}$ are summarized in Table 4.1.

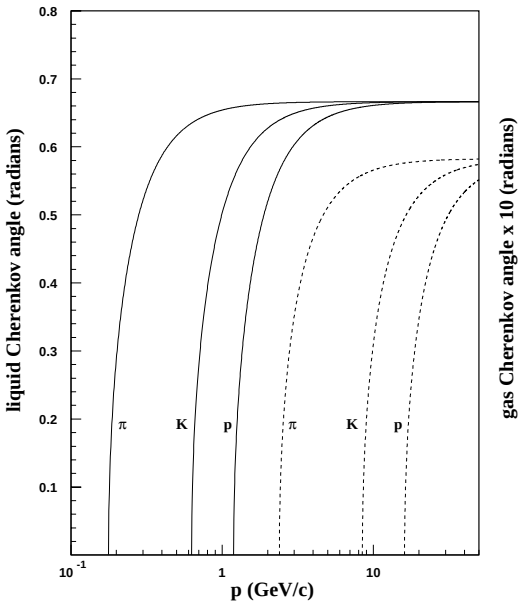

Figure 4.3: The Cherenkov angle for the (solid line) liquid and (dashed line) gas radiators in the barrel CRID as a function of momentum for the three long lived hadronic particle species.

Table 4.1: Momentum thresholds for the barrel CRID radiators in GeV/c.

Radiator	$e^{\pm}$	$\mu^{\pm}$	$\pi^{\pm}$	$K^{\pm}$	$p/\bar{p}$
C_5F_{12}/N_2	0.009	1.811	2.393	8.463	16.084
C_6F_{14}	0.001	0.134	0.177	0.628	1.193

Figure 4.4 displays the separation power between the two barrel CRID radiators for the e/π, π/K, and K/p particle combinations. The barrel CRID allows π/K separation at the 3 σ level from 0.3 GeV/c to almost 30 GeV/c, i.e. over almost two orders of magnitude.

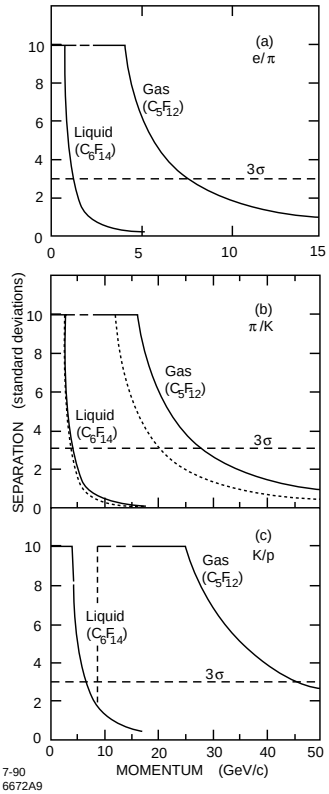

Figure 4.4: Separation power of the two barrel CRID radiators for three particle combinations.

4.2.2 Single Electron Sensitive Detector for the Barrel CRID

In the barrel CRID, an array of 40 time projection chambers (TPC) serves as detection device for the Cherenkov photons. The TPC is filled with C_2H_6 drift gas and contains a 0.1% admixture of the photocathode TMAE, introduced into the drift gas by bubbling the drift gas through liquid TMAE. The TMAE additive is ionized by the UV Cherenkov photons and releases single photoelectrons into the drift gas. Under a 400 V/cm electric field inside the TPC, these photoelectrons drift parallel to the SLD magnetic field to a multiwire plane (MWPC). A TPC is illustrated in Figure 4.5. The TPC volume is 126.8 cm long and 30.7 cm wide, with a thickness that tapers from 9.2 cm at the instrumented detector end to 5.6 cm at the high voltage (HV) end, in order to prevent electrons being lost near the TPC faces due to transverse diffusion. The two TPC windows consist of fused quartz, and the sides are constructed from G-10 fiberglass epoxy. The inner and outer surfaces of these four long sides are covered with metal traces on a 3.175 mm pitch, whose potentials are determined by a resistor ladder connecting the 1.5 kV detector end with the -55 kV HV end.

Both the TMAE quantum efficiency and the transmission of fused quartz are shown in Figure 4.6. The photoelectrons are detected by an anode wire plane, with one TPC containing 93 carbon wires, 10.35 cm long and 7 μm in diameter, arranged in a row with 3.175 mm pitch. The x, y, z TPC coordinate system used in the reconstruction of the photoelectron coordinates is also depicted in Figure 4.5. The x, y, z photoelectron coordinates are reconstruced from the wire address, charge division on the wire, and drift time information, respectively, within 1 mm resolution for each coordinate, yielding about 4 mrad resolution on the Cherenkov angle. The TPC detector end is shown in more detail in Figure 4.7. The array of field shaping wires and blinds is designed to guide the photoelectrons to the anode wires. The blinds help prevent photons produced in the electron avalanche near the anode from re-entering the TPC volume. The 1500 V cathode voltage

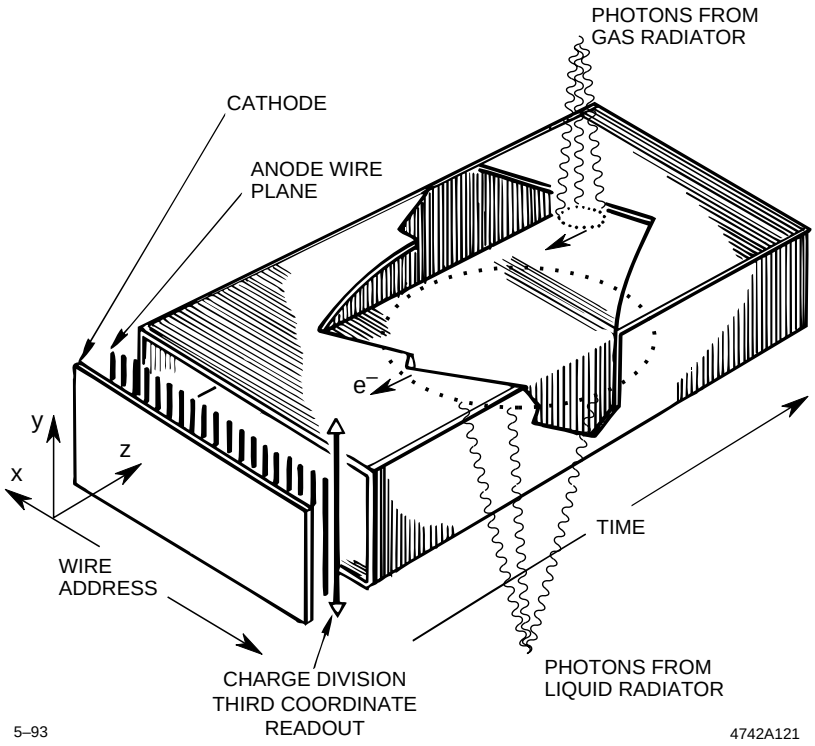

Figure 4.5: View of a barrel CRID TPC.

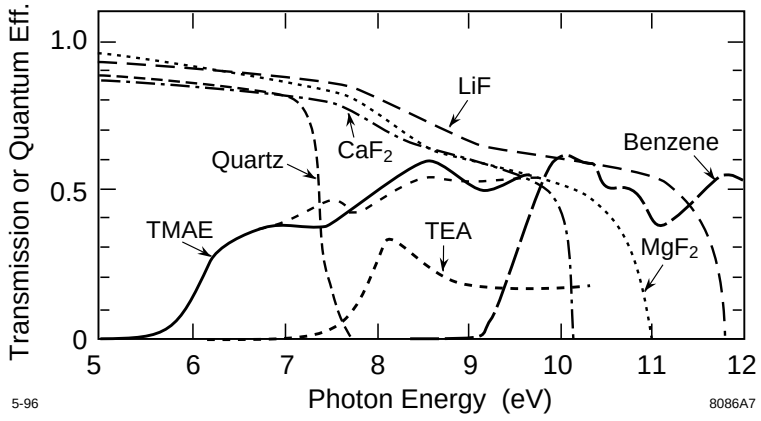

Figure 4.6: Quantum efficiency and transmission, as a function of photon energy, for several materials. Note the properties of quartz and TMAE for UV photon wavelengths.

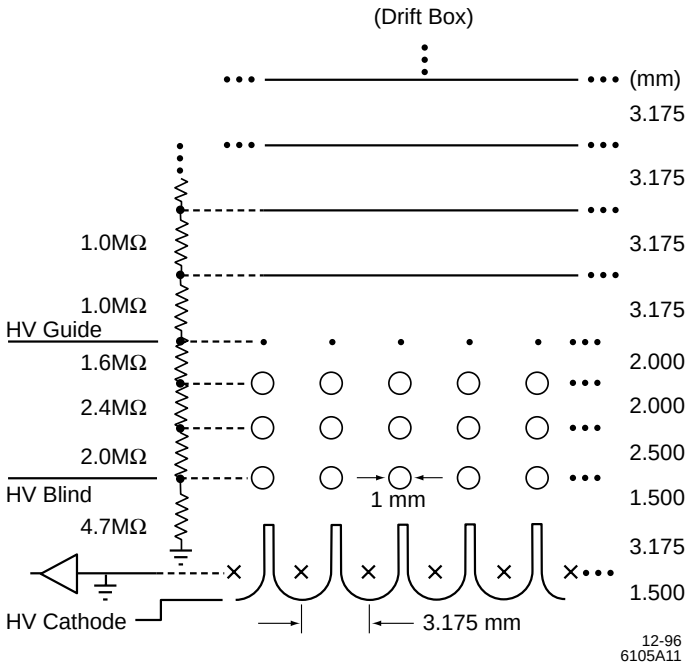

Figure 4.7: TPC detector end, with field shaping wires and blinds directing the photoelectrons to the anode wire plane.

leads to a gas gain of $2 - 3 \times 10^5$.

The preampifier signals from the wire planes are sampled in 67.2 ns buckets and stored in Analog Memory Units (AMUs), and digitized in Analog to Digital Converters (ADCs). The Data Correction Units (DCUs) zero-suppress the amplitudes and apply a pedestal correction. Additional processing occurs in the Waveform Sampling Modules (WSMs), before the digitized amplitude information is sent to ALEPH Event Builders (AEBs) which format the data for permanent storage (tape). The pulse leading edge time, pulse height and width, and a 32 bit quality word characterizing the pulse, are stored. The CRID readout electronics and data processing are described in more detail in Ref. [94].

The long-term operational performance of the barrel CRID detector, including experience with

wire aging and wire breakage rates, circulation and purification of gas and liquid radiators, electronics performance, monitoring of CRID hardware, estimates of Cherenkov N_o and the average number of photoelectrons per ring for gas and liquid radiators, is discussed in detail in Ref. [95].

4.3 Barrel CRID Alignment

The offline processing of CRID information begins with the CRID calibration, which takes into account the drift velocity, timing offsets, and electrostatic and magnetic field distortions. These corrections are applied to the coordinate system within the individual TPC. The drift velocity of the photoelectrons, as well as the influence of magnetic field distortions, are determined with an array of optical fibers injecting UV photons from a Xe flashlamp into the TPCs at regular intervals.

Remaining geometrical mis-alignments with respect to the CDC of the entire barrel CRID structure and the 40 individual TPC boxes were investigated and, generally, corrected. The barrel CRID TPC alignment for the 1996-8 data, presented here, extends previous work [7] on the 1993-5 data.

The TPC alignment is based on the comparison of the positions of charged tracks, extrapolated from the CDC, with the location of saturated hits caused by minimum ionizing particles (MIPs) passing through the TPCs. The TPC alignment consists of two successive steps. First we correct for global shifts and rotations of the entire barrel CRID structure with respect to the CDC, and then we align the individual TPC boxes. The 40 TPC boxes are numbered 0–19 (20–39) on the South (North) side of the detector. In the following description of the alignment procedure, we will refer to the TPC x, y, z coordinate system illustrated in Figure 4.5.

In principle, there are six degrees of freedom for the global alignment of the barrel CRID

structure, and another six degress of freedom for each TPC. However, the extrapolated track-MIP comparison is complicated by diffusion of the electrons on their drift towards the MWPC, which is different for the roughly 1000 photoelectrons deposited by MIPs than for single photelectrons from Cherenkov rings.

Due to the problem with electron diffusion, a detailed z alignment is not attempted, but the z coordinate corresponding to the earliest arrival time of the ionization trail is used. The z differences between extrapolated and detected track positions increase almost linearly with z, i.e. drift time. Therefore, we first perform a simple calibration to adjust roughly for diffusion by assuming $z_{ion} - z_{extrap} = c_1 z_{extrap} + c_2$. The constants c_1 and c_2 can be determined simultaneously. As illustrated in Figure 4.8, the residual of this expression is typically smaller than 1 mm over the length of the TPC box. This precision is adequate for the determination of the azimuthal and radial alignments. TPC z is used for subdividing the TPC into several z slices to measure TPC $\Delta x/\Delta z$ tilts. The $\Delta x/\Delta y$ roll angle around the TPC z axis cannot be determined by an extrapolated track-MIP comparison due to the small TPC width, which provides too short a lever arm for alignment.

The use of saturated hits allows 4 degress of freedom for each TPC, i.e. the azimuthal shift (TPC x) and tilt (TPC $\Delta x/\Delta z$) and the radial shift (TPC y) and tilt (TPC $\Delta y/\Delta z$), to be aligned. However, in the case of saturated hits, the TPC y coordinate is derived from charge division of two saturated amplifiers, and the TPC x coordinate remains as the only reliable parameter for both the azimuthal and radial TPC alignment. The TPC x position of the saturated hits is not well defined at the level of accuracy required, but we may assume that equal diffusion at both ends of the track segment leaves the measured center quite unaffected. The variable used for the azimuthal alignment is $x_{center} = (x_{entry} + x_{exit})/2$, where x_{entry} and x_{exit} refer to the azimuthal TPC entry and exit position of the track. Tracks with momentum $p > 1.5$ GeV/c, which do not

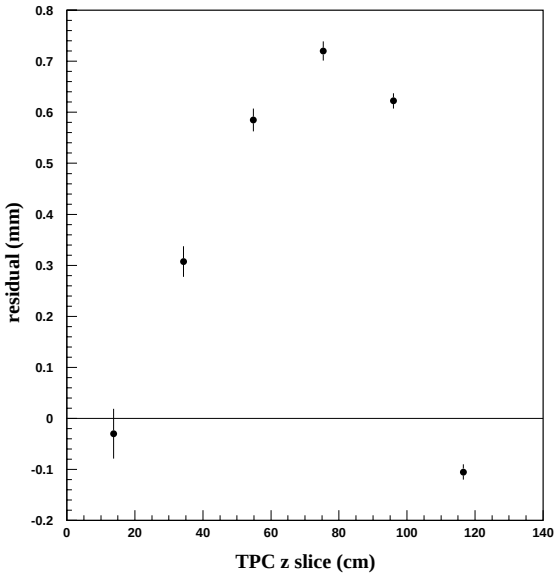

Figure 4.8: First step in the alignment procedure, showing the residual of the TPC z calibration.

bend appreciably within the TPC box, are used for the azimuthal alignment.

In 1995, the CDC was taken out of the SLD for the installation of VXD3, and we may expect to observe effects on the global alignment in the data. The TPC x offsets for the high voltage TPC end ("MIDPLANE") and the instrumented end ("ENDS") of the TPC are shown in Figure 4.9 for the 1996 data using the 1994-5 alignment constants. The sinusoidal offsets indicate a shift of the barrel CRID structure with respect to the CDC by about 2 mm. Also shown are the tilts which indicate a rotational offset of the entire CRID at the 0.5 mrad level.

We succeeded in reducing this global discrepancy by introducing shifts and a rotation in the alignment affecting the entire barrel CRID structure. Figure 4.10 illustrates how the sinusoidal variation is diminished by a vertical shift of 1.7 mm. The remaining offsets are further smoothened by a combination of a 0.2 mm horizontal shift, followed by a 0.16 mrad rotation about the beam

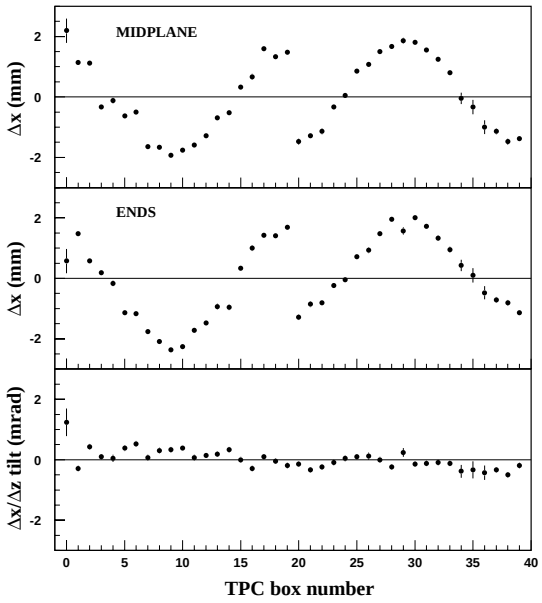

Figure 4.9: 1996 azimuthal alignment with 1994-5 geometrical constants, showing (top) Δx at MIDPLANE, (middle) Δx at ENDS, and (bottom) $\Delta x/\Delta z$ tilts for all 40 TPC boxes.

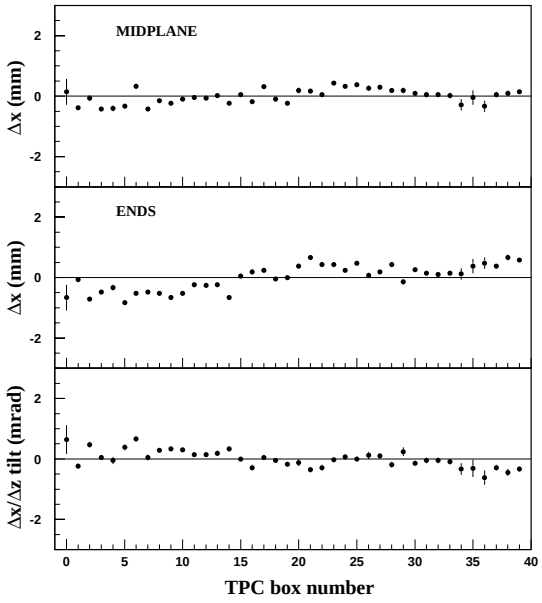

Figure 4.10: 1996 azimuthal alignment after a global 1.7 mm vertical shift.

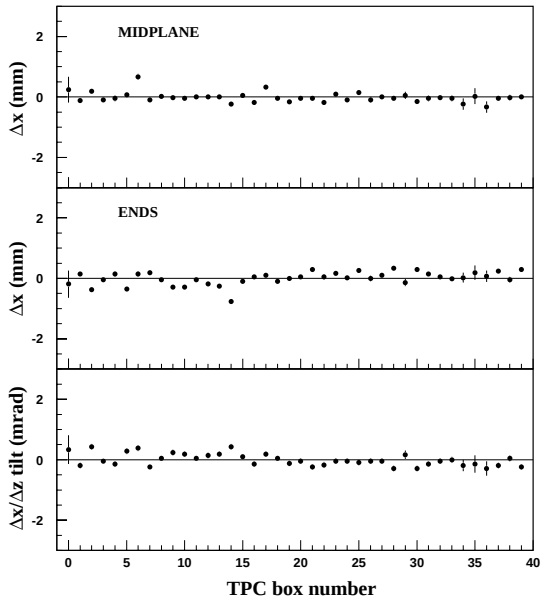

Figure 4.11: 1996 azimuthal alignment after a combination of a global 1.7 mm vertical shift and global 0.2 mm horizontal shift, followed by a global 0.16 mrad rotation about the beam axis.

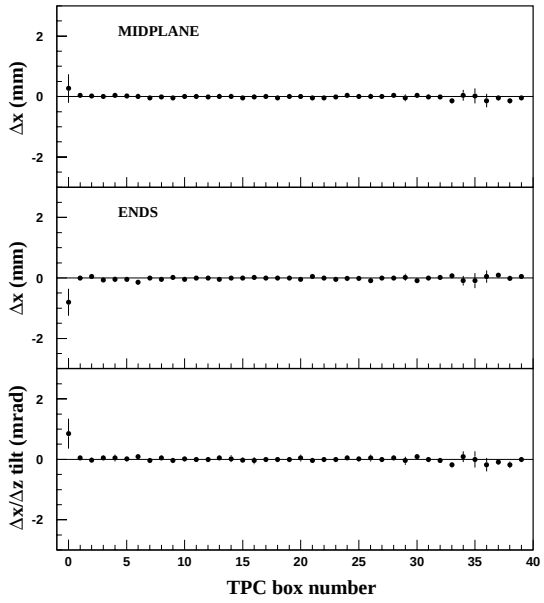

Figure 4.12: 1996 azimuthal alignment with new constants, shown for all 40 TPC boxes.

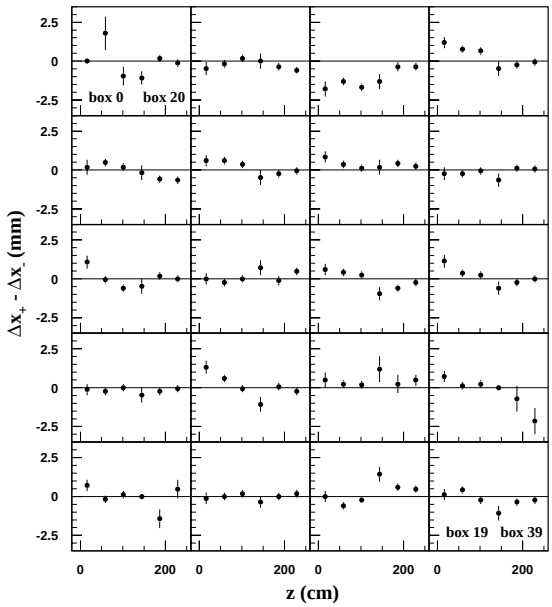

Figure 4.13: 1996 radial alignment with 1994-5 constants, shown for all 40 TPC boxes.

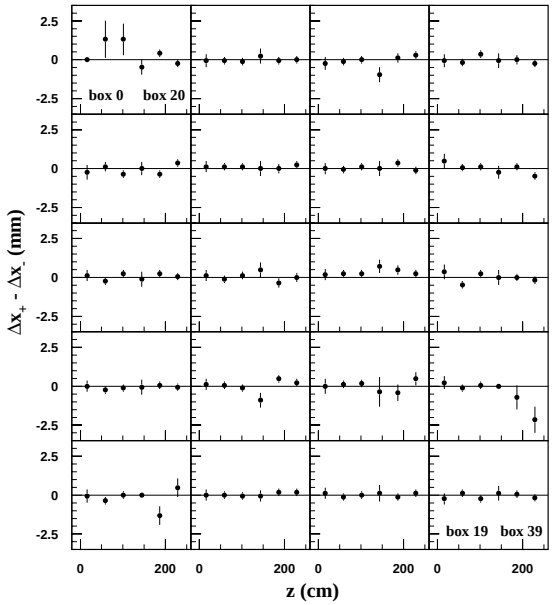

Figure 4.14: 1996 radial alignment with new constants, shown for all 40 TPC boxes.

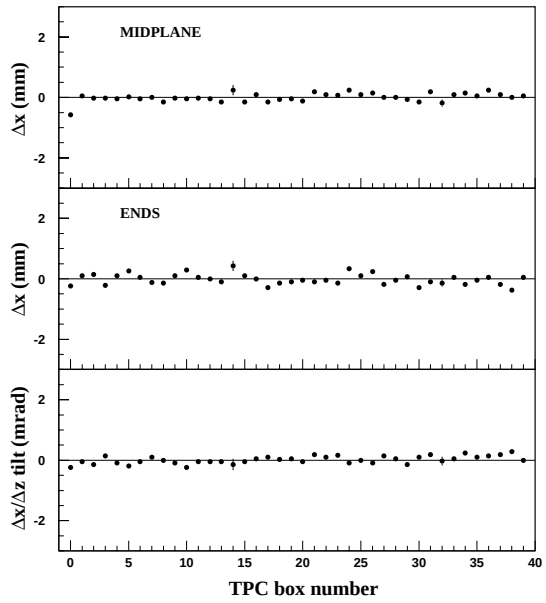

Figure 4.15: 1997 azimuthal alignment with 1996 constants, shown for all 40 TPC boxes.

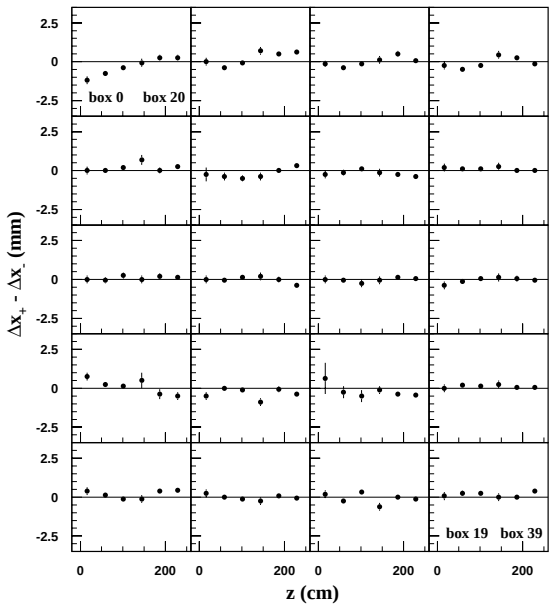

Figure 4.16: 1997 radial alignment with 1996 constants, shown for all 40 TPC boxes.

axis, as shown in Figure 4.11.

After the global alignment, we tune the alignment of the individual TPC boxes. Several iterations on the array of TPC boxes further improve the azimuthal alignment, leading to the result for the 1996 data depicted in Figure 4.12. The radial alignment cannot make use of the relatively stiff tracks used for the azimuthal alignment, but employs tracks in the momentum range of 0.25 GeV/c $< p <$ 0.8 GeV/c that enter the TPC at a shallower angle and curve within the TPCs. The TPCs are divided into three drift time slices, and the x offsets of positively and negatively charged tracks, curving into opposite directions, are used to monitor the radial mis-alignment. Statistical fluctuations are reduced by investigating the difference between the x offsets of positively and negatively charged tracks, $\Delta x_+ - \Delta x_-$. In Figure 4.13, pairs of corresponding South/North TPC boxes are shown grouped together, and this difference is illustrated for three z slices per box for the 1996 data with the 1994-5 constants. For the radial alignment, radial offsets and tilts are determined by straight line fits to $\Delta x_+ - \Delta x_-$ for each box. Azimuthal and radial alignments are coupled, and several iterations are performed until good alignment is achieved for both. Figure 4.14 shows the result of the radial alignment for the 1996 data after some tuning.

The alignment presented so far refers to 1996 R13 data. The alignments for the later data reconstructions, R14 and R15, using the 1996 R13 constants, showed somewhat more scatter, but were fully adequate after correcting a few individual TPC boxes. Similarly, the improved 1996 data constants were applied to the 1997 R15 data and finally to the 1997-8 R16 data of the current reconstruction. No global mis-alignments were observed in the 1997-8 data. As an example, Figure 4.15 and Figure 4.16 illustrate the azimuthal and radial alignments of 1997 R16 data with improved 1996 constants. Only small additional corrections to individual boxes are needed. The alignment for 1998 R16 data looks similar.

Improvements in the combined CDC and VXD3 tracking performance are expected to be

applied to 1996-8 data in the near term. It would be desirable to extend these improvements to the 1993-5 data, in order to create a uniform SLD data reconstruction. The CRID group plans to revisit the alignment of the barrel CRID TPC boxes after the final tracking improvements, in order to create the final CRID reconstruction of the 1993-8 SLD data set. However, these refinements are not very important for the A_s measurement.

4.4 Particle Identification with a Maximum Likelihood Method

After both internal and geometrical TPC alignments, the CRID information is used to reconstruct the Cherenkov angle [6; 96] of each TPC hit (photoelectron) associated with a charged track. For the purpose of particle identification, the CRID software employs a maximum likelihood method [96; 97] which optimizes the use of information and provides a simple framework for combining liquid and gas Cherenkov information to distinguish the 5 long lived particle candidates, $e^{\pm}$, $\mu^{\pm}$, $\pi^{\pm}$, $K^{\pm}$ and $p/\bar{p}$. The sum of all five particle identification likelihoods is normalized to 1. Particle identification is based on differences between the logarithms of these likelihoods.

The likelihood function, $\mathcal{L}$, represents the probability, for a particular hypothesis, of observing the data distribution. For the purpose of particle identification, the hypothesis is a certain set of particle assignments,$\{h_k\}$, for each track k, assuming a backgound model $b(\vec{x})$. The probability to observe n photoelectrons, if $\bar{n}$ denotes the number of expected number of photoelectrons for hypothesis $\{h_k\}$, is given by Poisson statistics:

$$P_{(n|\bar{n})} = \frac{\bar{n}^n}{n!} e^{-\bar{n}} \tag{4.4}$$

If $P(\vec{x})$ denotes the probability of a certain photoelectron being located in a differential volume $d\vec{x}^3$, then $\rho(\vec{x}) = \bar{n}P(\vec{x})$ is the expected number density of photoelectrons in $d\vec{x}^3$, and the likelihood

function is given by:

$$\mathcal{L} = P_{(n|\bar{n})} P(\{\vec{x_i}\}) = \bar{n}^n e^{-\bar{n}} \prod_{i=1}^{n} P(\vec{x_i}) = e^{-\bar{n}} \prod_{i=1}^{n} \rho(\vec{x_i}). \tag{4.5}$$

where the permutations of the n photoelectrons are taken into account, and the index i runs over all observed photoelectrons. $\rho(\vec{x})$ consists of a term representing the Cherenkov ring produced by each track, and a background term, $b(\vec{x})$, independent of tracks:

$$\rho(\vec{x}) = b(\vec{x}) + \sum_{k} \rho_{k,h_k}(\vec{x}), \tag{4.6}$$

where $\rho_{k,h_k}(\vec{x})$ represents the density due to track k for particle hypothesis h_k.

The set $\{h_k\}$ which maximizes $\mathcal{L}$ needs to be determined. Assuming that the most probable hypothesis h_k for track k is approximately independent of the hypotheses for other tracks $\{h_j\}_{j \neq k}$, the iteration continues until the set $\{h_k\}$ is stable. The likelihood for a hypothesis h_k can be written as:

$$\mathcal{L}_{k,h_k} = e^{-M_{k,h_k}} \prod_{i} \left(b_k + \rho_{k,h_k}(\vec{x_i})\right), \tag{4.7}$$

where b_k denotes the background independent of track k, and M_{k,h_k} describes the expected number of photoelectrons after taking total internal reflection into account. The logarithm of the relative likelihood, $\mathcal{L}'_{k,h_k}$, is used in physics analyses:

$$\log \mathcal{L}'_{k,h_k} = -M_{k,h_k} + \sum_{i} \log(1 + \frac{\rho_{k,h_k}(\vec{x_i})}{b_k(\vec{x_i})}). \tag{4.8}$$

The method uses a simplified, i.e. uniform, background $b(\vec{x})$. Starting with the pion hypothesis for the $\{h_k\}$, the CRID algorithm for particle identification typically converges after only 2–3

iterations. Figure 4.17 shows sample plots of gas rings reconstructed in Cherenkov space, i.e. in coordinates $\theta_C \sin\phi_C$ and $\theta_C \cos\phi_C$, where θ_C denotes the Cherenkov angle and ϕ_C is the azimuthal angle in the plane perpendicular to the track.

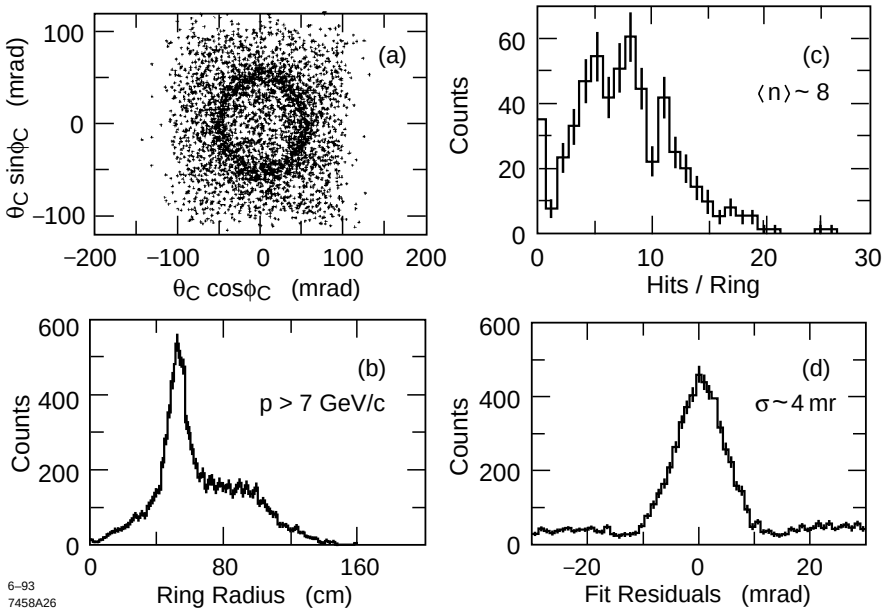

Figure 4.17: CRID gas rings: (a) in Cherenkov space, (b) radii, (c) number of photoelectrons per ring, (d) radii fit residuals.

4.5 Barrel CRID Physics Performance

The physics performance of the barrel CRID was first studied for the charged hadron spectra of $\pi^{\pm}$, $K^{\pm}$, and $p/\bar{p}$ in Z^0 decays [6]. In this benchmark analysis, the particle identification efficiencies for these hadron species, depicted in Figure 4.18 in the form of a 3×3 matrix, were calibrated from data where possible. The notation $a \to b$ denotes the efficiency for a true particle a to be identified by the barrel CRID as a particle of type b. A combination of vertexing and invariant mass cuts was used to select a high purity $\pi^{\pm}$ sample from $K^0_s \to \pi^+\pi^-$ and τ decays. Due to low statistics, $p/\bar{p}$ from $\Lambda^0(\bar{\Lambda}^0) \to p(\bar{p})\pi^{\mp}$ decays were only used for cross checks. The other elements were derived

from the Monte Carlo simulation. Further corrections were applied to correct for effects of particle mis-identification in the calibration sample and differences in track quality cuts. The particle identification efficiencies show a varying degree of overlap in the momentum coverage provided by the combination of liquid and gaseous barrel CRID radiators. In the main diagonal elements, the identification efficiencies peak at over 80%. The off-diagonal elements show mis-identification rates which are mostly well below 5%. Figure 4.19 shows the measured production fractions of these $\pi^{\pm}$, $K^{\pm}$, and $p/\bar{p}$ as a function of track momentum. The sum of the three fractions is a well satisfied consistency check.

Both the barrel CRID and the DELPHI RICH [89] represent the first use of Cherenkov ring imaging techniques on the large scale required for multi-purpose collider detectors. The barrel CRID works at approximately the projected design performance [95], and ring imaging detectors are now a standard technology employed in a new generation of experiments such as BaBar and CLEO III.

Several interesting and unique measurements have been performed with the CRID at the Z^0 resonance. Some examples are: the studies of charged hadron production [6; 9] and ϕ and K^{*0} vector meson production [7] in separate samples of light flavor, $c\bar{c}$, and $b\bar{b}$ events; correlation studies [98] between pairs of identified $\pi^{\pm}$, $K^{\pm}$, and $p/\bar{p}$; the observation of light leading hadrons [9]; and the use of $K^{\pm}$ to tag D [99] and B [100] meson decays inclusively.

The CRID is crucial to the analysis presented in this thesis. The remaining Chapters describe the data analysis performed on the full 1993-8 SLD data sample. The result is discussed, and the conclusions provide a comparison with previous measurements.

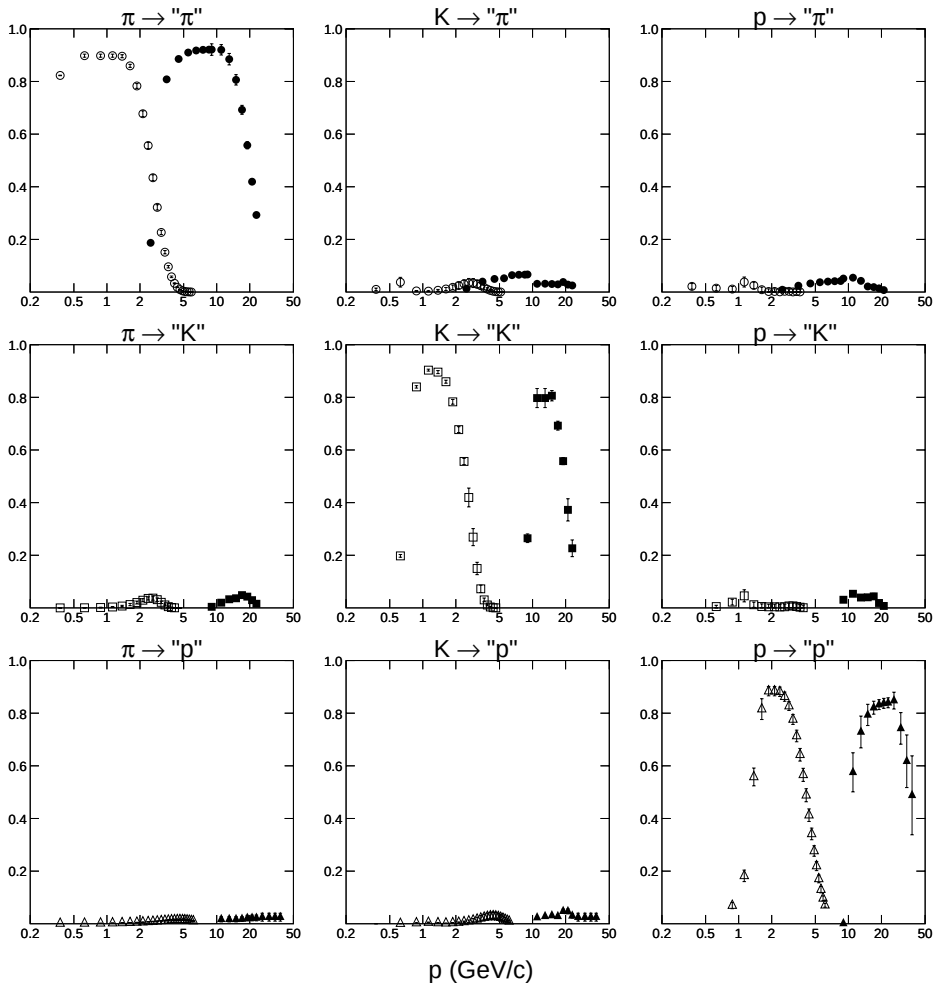

Figure 4.18: The barrel CRID particle identification efficiencies as a function of track momentum. The off-diagonal elements give the mis-identification rates.

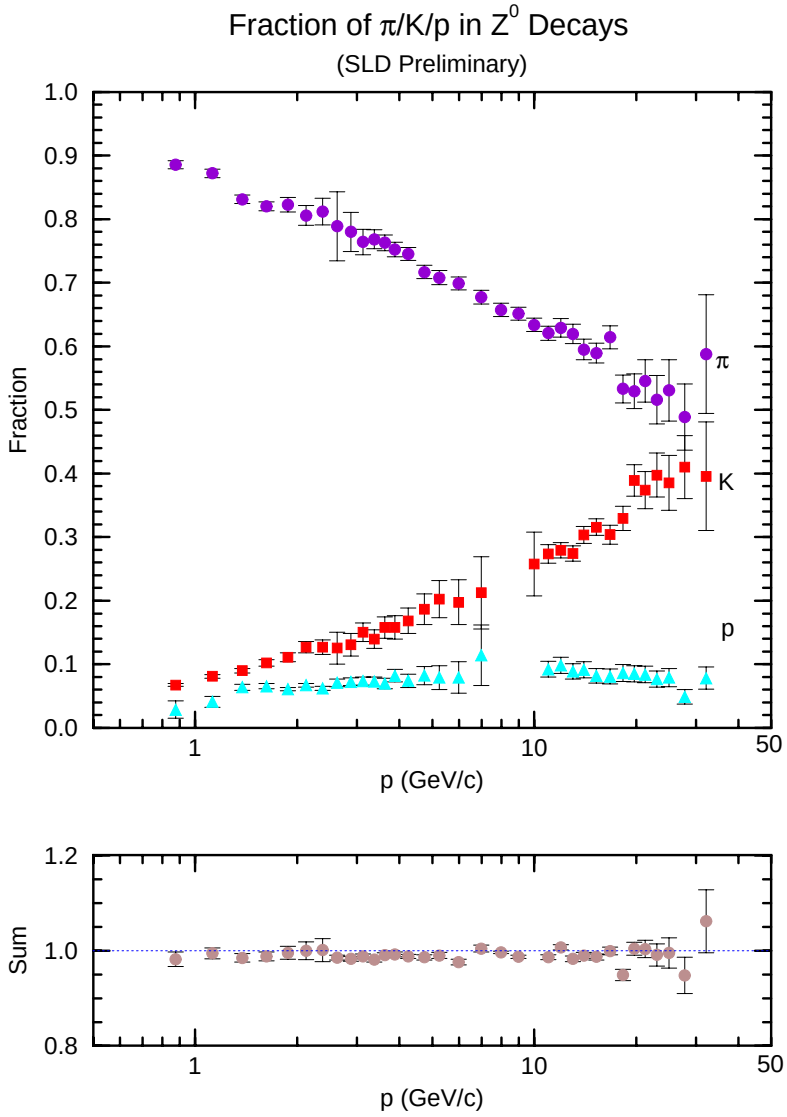

Figure 4.19: The $\pi^{\pm}$, $K^{\pm}$, and $p/\bar{p}$ production fractions as a function of track momentum. The sum of the fractions, shown below, is a well satisfied consistency check.

Chapter 5

Hadronic Event Selection

The main analysis begins with the selection of the hadronic event sample, which is common to all SLD hadron analyses. Next, tracking information from the kinematics of heavy flavor decays is used to suppress heavy flavor ($c\bar{c} + b\bar{b}$) events, resulting in a light flavor ($u\bar{u} + d\bar{d} + s\bar{s}$) sample tagged with high purity and efficiency.

5.1 Hadronic Event Filter

Before the data on tape can be used for physics analysis, off-line filter algorithms process information from the calorimetry and tracking (LAC, WIC and CDC) to select potential Z^0 candidates by rejecting a substantial fraction of the background. The Energy Imbalance Trigger (EIT) uses LAC information to select events with minimum energy and good forward-backward energetic balance, whereas the Track Trigger requires at least one track with momentum $p > 1$ GeV/c. Hadronic Z^0 candidates are required to pass at least one of these two filters. The EIT (Pass 1) filter imposes cuts based on the LAC quantities listed in Table 5.1 where $NEMHI$ denotes the number of LAC EM towers above the 60 ADC counts high threshold, ELO sums the energy deposited in all LAC EM (HAD) towers above the 8(12) ADC counts low threshold, and similarly, EHI sums the energy deposited in all LAC EM (HAD) towers above the 60 (120) ADC counts high threshold. The first and third requirements have been designed to reject SLC-based background events (beam-gas events), and the last requirement specifically removes events containing large

numbers of SLC-related muons.

Table 5.1: Summary of EIT (Pass 1) filter requirements.

1.	$NEMHI > 0$ for both detector hemispheres
2.	$NEMHI \geq 10$
3.	$ELO < 140$ GeV$_{\|min-Iscale}$
4.	$EHI > 15$ GeV$_{\|min-Iscale}$
5.	$2 \cdot EHI > 3 \cdot (ELO - 70$ GeV$)$

The EIT Pass 1 filter rejects an estimated 97% of the background events which had passed the SLD readout trigger system and were written to tape. The combination of readout triggers and EIT Pass 1 filter results in an estimated selection efficiency of 92% [70] for hadronic Z^0 decays. Events surviving the EIT Pass 1 filter are classified by the EIT Pass 2 filter into hadronic, μ-pair, or WAB event candidates. Finally, the filtered events are processed by a detector reconstruction algorithm and written out to data summary tapes (DST). Physics analyses run on DSTs or their compressed mini/micro DST versions.

5.2 Hadronic Event Selection

After passing hadronic event candidates through the filtering procedure described above, the standard cuts [61; 101] summarized in Table 5.2 are applied to the data to select well measured tracks and a hadronic event sample well contained within the fiducial volume of the barrel SLD detector.

The thrust axis, $\hat{t}$, determined from LAC energy clusters rather than charged tracks in order to avoid a bias close to the edge of the CDC acceptance, is defined as the axis that maximizes the thrust, T, of the event:

$$T = \frac{\sum_{clusters} |\vec{p} \cdot \hat{t}|}{\sum_{clusters} |\vec{p}|} \tag{5.1}$$

Table 5.2: Summary of hadronic event selection requirements.

1.	EIT filter passed
2.	VXD, CDC and LAC operational
3.	Precisely determined interaction point (IP)
4.	e^- beam polarization measurement available
5.	Minimum of 7 charged tracks with $p_\perp > 0.2$ GeV/c and $doca_{rz}^{IP} < 5$ cm
6.	Minimum of 3 charged tracks with at least 2 VXD hits each
7.	Minimum of 18 GeV visible energy, assuming the $\pi^\pm$ mass for each track
8.	$\lvert\cos\theta_{thrust}\rvert < 0.71$, where the thrust axis polar angle, θ_{thrust}, is measured with respect to the e^+ beam direction

where the 3-momentum, $\vec{p}$, of the energy cluster is calculated assuming the IP as origin and the pion mass for the particle that caused the energy deposition. The $|\cos\theta_{thrust}| < 0.71$ requirement ensures good containment of the event within the barrel portion of the detector. The IP requirement is imposed to allow the flavor tagging technique, described below, to be applied, and the polarization requirement ensures that only events with well determined electron beam polarization enter the event sample.

Figure 5.1 gives the distributions for the number of charged tracks, the number of VXD-linked charged tracks, the visible energy, and $\cos\theta_{thrust}$ for the 1993-8 data sample after all event selection cuts have been applied. We observe quite good agreement between the data and the Monte Carlo simulation. Table 5.3 summarizes the selected hadronic event statistics for the three different data run periods. The estimated non-hadronic background of less than 0.2% is dominated by $Z^0 \to \tau^+\tau^-$ events.

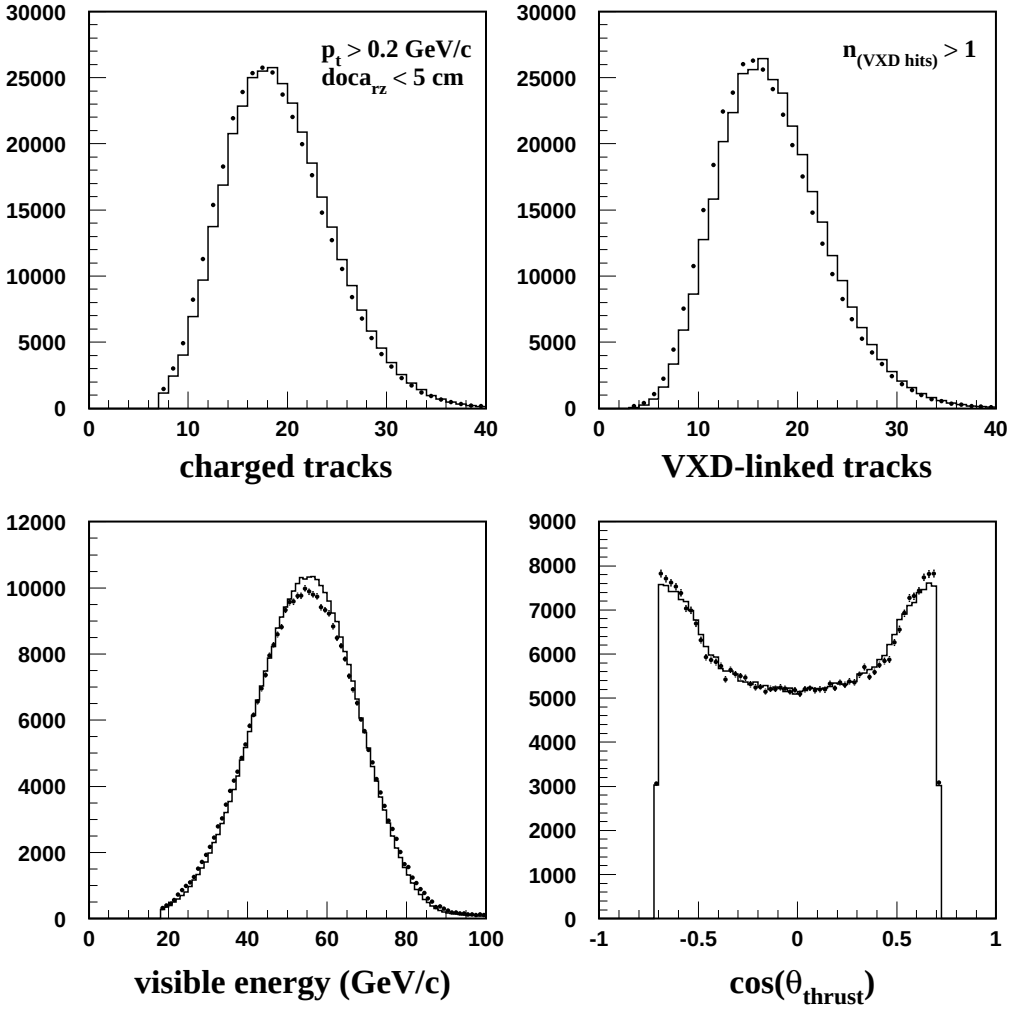

Figure 5.1: Distribution of several hadronic event selection variables, with the dots (histograms) denoting the data (Monte Carlo simulation).

Table 5.3: Selected hadronic event sample for the 1993-1998 data runs.

Run period	Reconstruction	Hadronic events
1993-5	R12a	90,646
1996	R15	34,314
1997-8	R16	217,361
Total:		342,321

5.2.1 Precise Determination of the Interaction Point

The position of the IP is important for the flavor tagging technique. The transverse and longitudinal components of the IP position are determined in two steps.

After extrapolating all charged tracks in a hadronic event back to the center of the SLD beam pipe, and fitting for a common vertex, an event-by-event transverse IP position is obtained with an error ellipse of about 100 (15) μm along the major (minor) axis. However, given the small and stable SLC interaction region, a more precise estimate of the average transverse IP position can be derived by averaging over a set of 30 sequential hadronic events. This procedure essentially removes the thrust axis dependence and the bias from secondary displaced vertices, and leads to an isotropic uncertainty. The iterative algorithm used for this procedure typically converges after about 5 iterations with $\chi^2/dof < 1.3$. The average transverse IP position is thus determined to a precision of $\sigma_{IP} \simeq 7(5)$ μm for the VXD2 (VXD3) data, and was cross checked using the xy impact parameters of tracks in $Z^0 \to \mu^+\mu^-$ events, as shown in Figure 5.2. Both muon tracks were extrapolated back to the IP and their extrapolation errors were subtracted. The width of the resulting destribution is 7 ± 2 μm, consistent with the resolution derived from the hadronic sample.

In the next step, the longitudinal position of the IP is determined on an event-by-event basis,

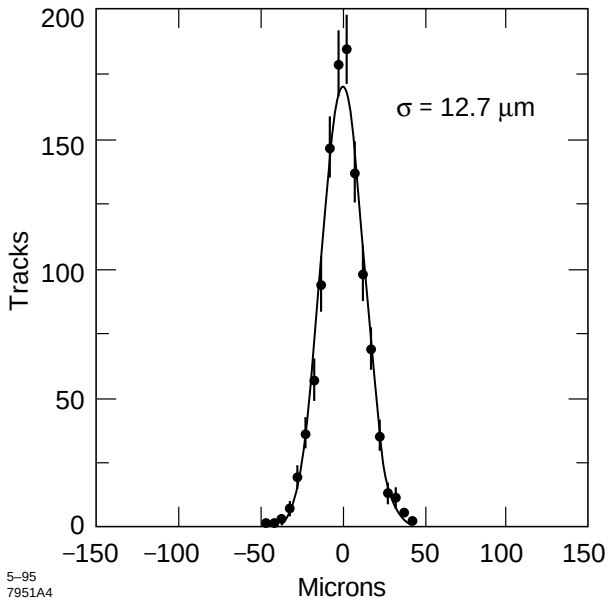

Figure 5.2: xy impact parameter of tracks in $\mu^+\mu^-$ events. A resolution of about 7 (5) μm for the VXD2 (VXD3) data is obtained after correcting for track extrapolation uncertainties.

since the longitudinal distribution of the IP position is much larger than its transverse spread. Tracks with associated VXD hits in an event are extrapolated to the point of closest approach in the transverse plane to the average IP position, determined previously. The z position of this point is calculated, and if its xy impact parameter is less than 500 μm and 3 σ from the average transverse IP position, it is used to determine the median z position of the event. Resolutions on the z position [102] of 32 (36, 52) μm for $u\bar{u} + d\bar{d} + s\bar{s}$ ($c\bar{c}$, $b\bar{b}$) events have been obtained with VDX2 from the Monte Carlo simulation. With VXD3, the resolutions on the z position improve to 9 (17) μm for $u\bar{u} + d\bar{d} + s\bar{s}$ ($b\bar{b}$) events.

5.3 Flavor Tagging with the Normalized 2-D Impact Parameter

The analysis proceeds by suppressing the heavy flavor ($c\bar{c}$ and $b\bar{b}$) background in order to reduce the effects of their decays. This is advantageous because it will allow the use of relatively low-momentum strange particles to tag $s\bar{s}$ events.

A light flavor ($u\bar{u} + d\bar{d} + s\bar{s}$) sample of rather high purity can be obtained with high tagging efficiency by making use of a technique [103] which exploits the exquisite tracking capabilities of the SLD. The method employs the impact parameters of charged tracks to separate light from heavy event flavors according to the number of tracks significantly displaced from the IP. This approach is based on the Z^0 decay properties of heavy B mesons, which typically propagate about 3 mm before decaying into secondary particles. D mesons travel roughly half this distance. The decay kinematics of these heavy hadrons leads to secondary particles with large impact parameters with respect to the IP, in contrast to light flavor events. Figure 5.3 presents a schematic comparison of light and heavy flavor decay topologies. This technique was improved [104; 105] by associating an algebraic sign to the impact parameter. As illustrated in Figure 5.4, charged tracks crossing the jet axis in front of (behind) the IP are assigned a positive (negative) sign. This parameter is referred to as the signed impact parameter.

Since the SLD tracking performs best in the plane perpendicular to the beam, we use a two dimensional version of the signed impact parameter technique. To reduce the effects of track reconstruction uncertainties and material interactions, only well reconstructed quality tracks [61; 101] are used. These tracks are required to have at least 40 CDC hits, a track fit quality of $\chi^2_{CDC}/dof < 5$, at least 1 VXD hit, the first CDC hit occuring within 39 cm radially from the IP to constrain the extrapolation distance to the VXD, and to extrapolate to the IP within 1 cm radially and 1.5 cm longitudinally to reject tracks originating from material interactions.

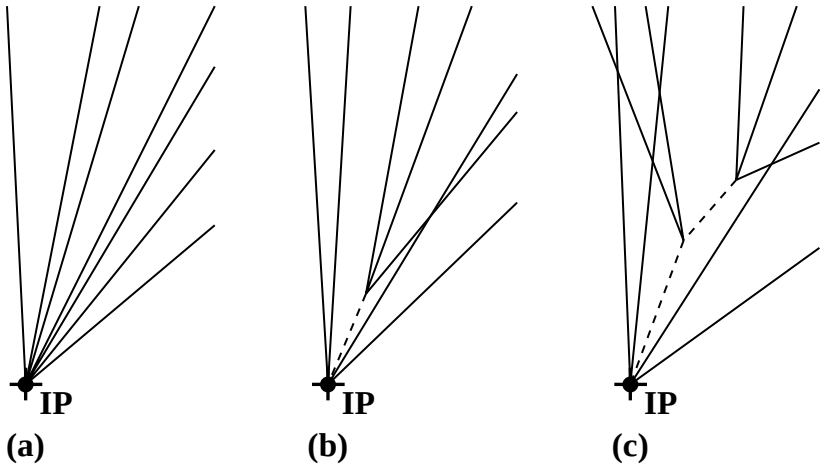

Figure 5.3: Schematic comparison of hadronic Z^0 decay topologies, showing (a) a light flavored event, (b) a secondary D hadron vertex in a $c\bar{c}$ event, and (c) a secondary (tertiary) B (D) hadron vertex in a $b\bar{b}$ event.

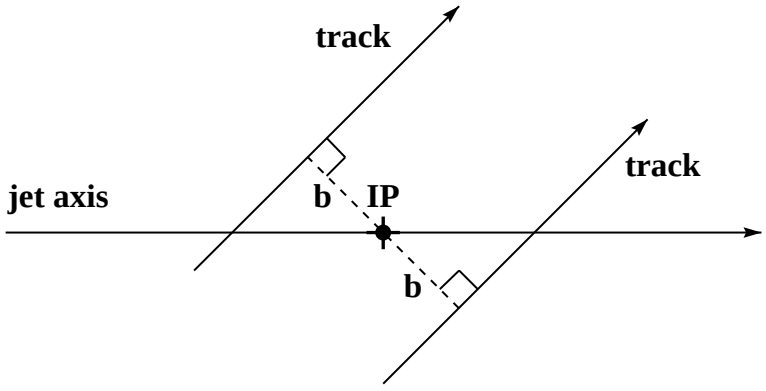

Figure 5.4: The impact parameter is assigned a positive (negative) sign if the charged track crosses the jet axis in front of (behind) the IP.

Pairs of oppositely charged tracks forming a good candidate vertex (generically referred to as V^0) and consistent with a γ conversion, a K_s^0 or a $\Lambda^0/\bar{\Lambda}^0$ candidate are removed. Furthermore, after combining the VXD and the CDC information, the tracks must have a track fit quality of $\chi^2_{VXD+CDC}/dof < 5$, and the 2-D impact parameter of the track to the IP has to satisfy $b < 3$ mm, with an uncertainty of $\sigma_b < 250$ μm.

After applying these track selection criteria, efficiency corrections [61] depending on the track dip angle and momentum are applied to provide good agreement between the distribution of quality tracks observed in data and the Monte Carlo simulation. Figure 5.5 shows the signed 2-D impact parameter for data and the Monte Carlo simulation. For the purpose of tagging the event flavor, we define a significant track as a quality track with a normalized impact parameter of $b/\sigma_b > 2.5$, and count the number of significant tracks, n_{sig}, per event. The tails of the signed 2-D impact parameter distribution are in good agreement. However the simulated core is too narrow, leading to discrepancies between data and Monte Carlo in the n_{sig} distribution. These differences can be removed by smearing the simulated impact parameter, as described in detail in Ref. [106]. Here, we use an equivalent scheme which we apply directly to the n_{sig} distribution. For each event, we increase n_{sig} by 1 with a probability independent of event flavor. Figure 5.6 illustrates the resulting n_{sig} distribution for data and the simulation.

As expected, events with very few significant tracks are mostly light flavor, whereas heavy flavor events are characterized by many significant tracks. Thus we can divide the hadronic sample into two subsamples:

- $u\bar{u} + d\bar{d} + s\bar{s}$ enriched sample with $n_{sig} = 0$ or 1
- $c\bar{c} + b\bar{b}$ enriched sample with $n_{sig} > 1$.

We find good agreement in the n_{sig} distribution between data and the simulation. However, we

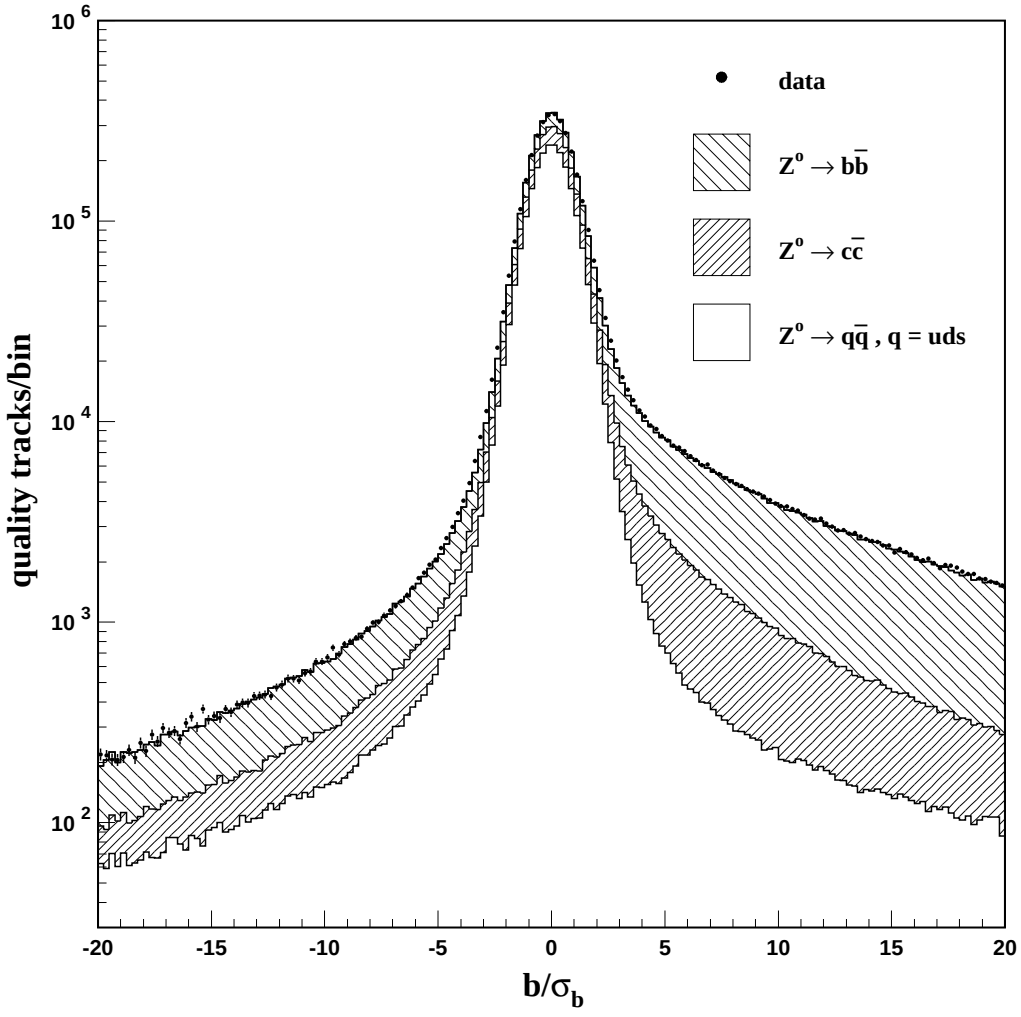

Figure 5.5: The normalized 2-D impact parameter for data (dots) and Monte Carlo simulation (histograms).

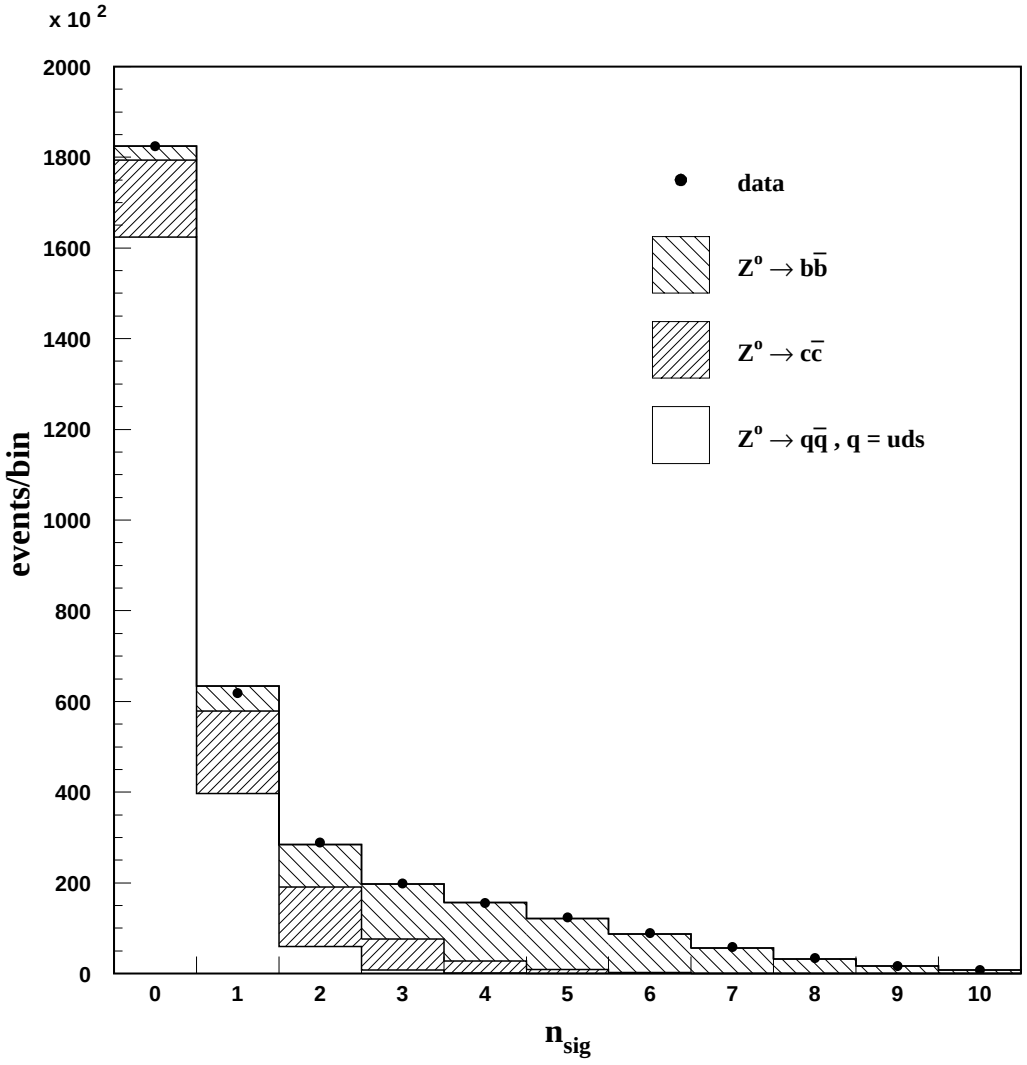

Figure 5.6: The number of significant tracks, n_{sig}, per event for data (dots) and Monte Carlo simulation (histograms). Note the separation between light and heavy flavors.

remove the small difference in normalization in the $n_{sig} = 1$ bin by randomly removing simulated events from that bin. The small systematic effect of this correction will be discussed in Chapter 8.

The $n_{sig} = 0$ or 1 sample, consisting of 244,385 events, is tagged as the light flavor sample and will be used in all subsequent studies. The event statistics of the light flavor tag for the different run periods is summarized in Table 5.4. The overall tagging efficiency $\epsilon(u\bar{u} + d\bar{d} + s\bar{s}) = 96.2\%$ and purity $\Pi(u\bar{u} + d\bar{d} + s\bar{s}) = 82.3\%$ are derived from the Monte Carlo simulation.

Table 5.4: Selected light flavor-tagged event sample for the 1993-1998 data runs.

Run period	$n_{sig} = 0$ or 1 events
1993-5	67,381
1996	24,769
1997-8	152,235
Total:	244,385

At the SLD, the technique outlined so far (with $b/\sigma_b > 3.0$) has been used for several different analyses to categorize the hadronic event sample into $u\bar{u} + d\bar{d} + s\bar{s}$, $c\bar{c}$, and $b\bar{b}$ enriched $n_{sig} = 0$, $n_{sig} = 1$ or 2, and $n_{sig} > 2$ samples (e.g. [5–7; 61]), respectively. For the A_s measurement, we have improved the light flavor tagging criteria in order to select a $u\bar{u} + d\bar{d} + s\bar{s}$ sample with high efficiency and high purity. The heavy flavor background contributes a relatively small systematic uncertainty to the A_s measurement (see Chapter 8).

Chapter 6

Selection of $s\bar{s}$ Events

The phenomena of leading strange particle production and strangeness suppression in the fragmentation process are crucial to the A_s measurement. This chapter introduces the concept of rapidity correlations which provide model-independent experimental evidence for leading particle production. The selection of $K^{\pm}$, $\Lambda^0/\bar{\Lambda}^0$ and K_s^0 is described, and the use of these strange particles to select a high-purity $s\bar{s}$ event sample is motivated. We discuss the polar angle distributions of the tagged strange quark, obtained after signing the thrust axis with the strangeness of the tagged particle.

6.1 Experimental Approach to A_s

The fragmentation process in hadronic jets can be probed more deeply by studying correlations [98; 107; 108] in the kinematic quantity rapidity between pairs of identified charged hadrons. The following discussion is based on Ref. [98] in which rapidity correlations in light flavor tagged events are investigated for the three particle species $\pi^{\pm}$, $K^{\pm}$ and $p/\bar{p}$. It is conventional in these studies to define the rapidity, y, for each charged particle track:

$$y = \frac{1}{2} \ln \left(\frac{E + p_{\parallel}}{E - p_{\parallel}} \right) \tag{6.1}$$

in terms of E, the energy of the particle calculated from the measured momentum and the appropriate hadron mass, and $p_{\parallel}$, the projection of the momentum along the thrust axis. The absolute value of the difference between the rapidities of each pair of identified particles:

$$|\Delta y| = |y_1 - y_2|, \tag{6.2}$$

is a suitable scale-independent variable for probing the fragmentation process. Figure 6.1 shows the $|\Delta y|$ distribution for each of the six pairs of the three identified hadron types. We observe a significant excess of opposite charge pairs over same charge pairs at small values of $|\Delta y|$. This signifies a short range correlation. For KK and pp pairs, this confirms local conservation of strangeness and baryon number, respectively. Excesses are seen in πK, Kp and πp and suggest charge ordering for all types of pairs in the fragmentation process.

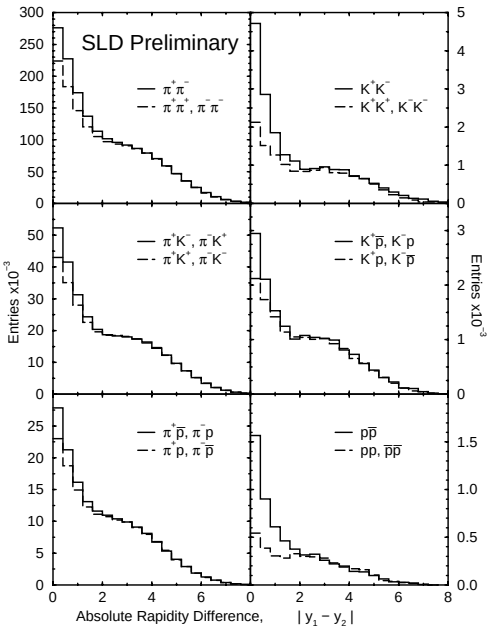

Figure 6.1: Rapidity differences for (solid) opposite charge pairs and (dashed) same charge pairs of identified $\pi^{\pm}$, $K^{\pm}$ and $p/\bar{p}$.

For the A_s measurement, $|\Delta y|$ distributions at high momentum are of special interest. Figure 6.2 shows a clear separation between pairs in the same jet ($|\Delta y| < 2.5$) and those in opposite jets ($|\Delta y| > 4$) after requiring $p > 9$ GeV/c for both tracks. The large excess of opposite charge pairs for all pair types at small $|\Delta y|$ confirms that locality also holds at high momenta.

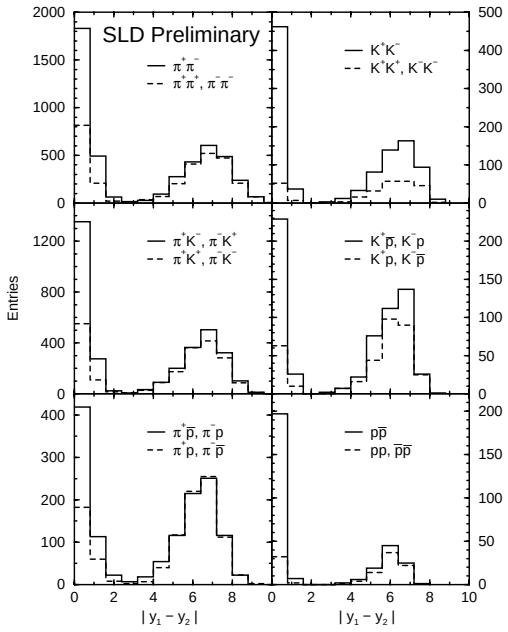

Figure 6.2: Rapidity differences for (solid) opposite charge pairs and (dashed) same charge pairs of identified $\pi^{\pm}$, $K^{\pm}$ and $p/\bar{p}$ with $p > 9$ GeV/c.

Long range correlations, i.e. excesses of opposite charge pairs at large $|\Delta y|$, are observed to various degrees. A particular strong long range correlation is observed for K^+K^- pairs. These pairs are predominantly produced in $s\bar{s}$ events, which can generate such a pair of opposite strangeness, located in opposite event hemispheres, and no additional strange particles. In contrast, we would expect approximately equal numbers of equal sign and opposite sign KK pairs from $u\bar{u}$ and $d\bar{d}$ events. The KK long range correlations have been observed previously in other experiments [108], but only the long range correlation measurements from the SLD presented here, identified with

the CRID, are sufficiently precise to allow quantitative conclusions. For $|\Delta y| > 4$, the predictions of the Monte Carlo simulation are generally consistent with the data. In Chapter 8, we make use of correlations to reduce the model dependence of the A_s measurement.

After the light flavor event selection described in the previous chapter, $Z^0 \to s\bar{s}$ event candidates are selected by the presence of identified high-momentum strange particles. These high-momentum particles are likely [8] to contain an initial $s/\bar{s}$ quark, but could also contain an initial $u/\bar{u}$ quark or an initial $d/\bar{d}$ quark or be from the decay of a D or B hadron. The average multiplicities [19] for several strange particles in hadronic Z^0 decays are summarized in Table 6.1. For the A_s measurement, it will be advantageous to use relatively abundant high-momentum strange particles which can be identified with high efficiency and purity. Based on previous SLD particle production studies [9] on $\pi^{\pm}$, $K^{\pm}$, $p/\bar{p}$ [6], K^0 and $\Lambda^0/\bar{\Lambda}^0$ [5], and $K^*(892)^0$ and $\phi(1020)$ [7], we choose $K^{\pm}$, K^0_s, and $\Lambda^0/\bar{\Lambda}^0$. The other three particle species in Table 6.1 have $K^{\pm}$ or K^0_s among their decay products. $K^{\pm}$ and $\Lambda^0/\bar{\Lambda}^0$ provide information on the sign of the strange quark, whereas the unsigned K^0_s is used to enhance the $s\bar{s}$ purity of the tagged sample.

Table 6.1: Average multiplicities for several strange particles in hadronic Z^0 decays.

Strange particle	Average multiplicity
$K^{\pm}$	2.39 ± 0.12
K^0	2.013 ± 0.033
$K^*(892)^0$	0.747 ± 0.028
$K^*(892)^{\pm}$	0.715 ± 0.059
$\Lambda^0/\bar{\Lambda}^0$	0.372 ± 0.009
$\phi(1020)$	0.109 ± 0.007

The heavy flavor ($c\bar{c} + b\bar{b}$) background is already suppressed by applying the signed impact

parameter technique. We require at least one strange particle in each event hemisphere to substantially increase the $s\bar{s}$ purity of the tagged sample by reducing the $u\bar{u} + d\bar{d}$ background, compared to a single tag using only the strange particle with the highest momentum in an event. This strategy reduces the model dependence of the result, and is implemented by analysis cuts which suppress the non-$s\bar{s}$ background and enhance the analyzing power of the signal to a level where useful constraints on these quantities can be obtained from the data.

6.2 Selection of Strange Particles

Identified $K^{\pm}$, $\Lambda^0/\bar{\Lambda}^0$ or K_s^0 are used to select $Z^0 \to s\bar{s}$ event candidates. The strange particle selection aims at achieving high tagging efficiency with good particle purity. The $K^{\pm}$ identification relies exclusively on the CRID, whereas the selection of K_s^0 uses the long flight distance, accuracy of pointing back to the primary interaction point, and reconstructed mass. The $\Lambda^0/\bar{\Lambda}^0$ is reconstructed with a combination of both methods.

6.2.1 Selection of $K^{\pm}$

The CRID allows $K^{\pm}$ to be separated from $p/\bar{p}$ and $\pi^{\pm}$ with high purity over a wide momentum range. However, the CRID efficiency matrix for $\pi^{\pm}$, $K^{\pm}$ or $p/\bar{p}$ identification (see Figure 4.18) shows a gap for $K^{\pm}$ in the momentum range of 3 GeV/c $< p <$ 9 GeV/c due to the limited overlap of liquid and gas radiators. We are interested in high-momentum $K^{\pm}$, and we therefore use the CRID gas system to identify $K^{\pm}$ with momentum $p >$ 9 GeV/c.

Since the SLD can collect data independently for each subsystem, the primary requirement is that the barrel CRID is operational, i.e. the high voltage is turned on and a valid drift velocity

calibration is available. During part of the 1993 data run, the drift velocity was calibrated improperly due to hardware problems related to the Xe flashlamps. All other run periods are unaffected by this problem. The CRID typically was energized after other systems due to the higher sensitivity to damage from background radiation. Once a sense wire in a CRID TPC was broken, the relevant TPC was turned off since it cannot take further data until repaired. The breakage rate of 3–5 wires per run period [95] is mostly due to material fatigue caused by the total accumulated radiation dose. During a run, an attempt is made to repair TPCs with broken wires in order to minimize their impact. The light flavor tagged data fractions for which the CRID was operational are summarized in Table 6.2. The differences in the CRID operation fractions are mostly due to the number of dead TPCs due to broken wires and general variations in the background conditions during data runs.

Table 6.2: Fraction of events with CRID operational in the three data run periods.

Run period	CRID operational
1993-5	89.1%
1996	77.9%
1997-8	83.0%

In the next step, we check each charged track candidate for good associated CRID information to ensure that it extrapolates through an active region of the CRID gas radiator and through a live CRID TPC. We require each track to possess good gas system information, and to be within the acceptance of the radiator and mirrors in the gas system of $|\cos\theta| < 0.68$. This removes tracks with poor CRID information or tracks that are likely to have scattered or interacted before exiting the CRID. These requirements are implemented as a quality bit in the standard CRID return code for each track. Additional track cuts were investigated: requiring $doca_{xy}^{IP} < 1$ mm for the distance of closest approach transverse to the beam axis, and $doca_{rz}^{IP} < 5$ mm for the distance of closest

approach along the axis from the measured IP, were found to be useful.

As discussed in more detail in Section 4.4, the CRID particle identification is based on a maximum likelihood method [96; 97]. For the remaining tracks, the momentum requirement $p > 9$ GeV/c is applied, and log-likelihoods, $\log \mathcal{L}_k$, are calculated for the CRID gas radiator for each of the three charged hadron hypotheses $\pi^{\pm}$, $K^{\pm}$ and $p/\bar{p}$. Figure 6.3 illustrates the log-likelihood separation between $K^{\pm}$ and $\pi^{\pm}$ candidates, and $K^{\pm}$ and $p/\bar{p}$ candidates. The simulation provides a qualitative description of the data. The effect of the quantitative differences on the final result for A_s is small and will be discussed in Chapter 8.

A track is tagged as a $K^{\pm}$ by the CRID gas system if both requirements:

$$\log \mathcal{L}_{K^{\pm}} - \log \mathcal{L}_{p/\bar{p}} > 3, \tag{6.3}$$

$$\log \mathcal{L}_{K^{\pm}} - \log \mathcal{L}_{\pi^{\pm}} > 3, \tag{6.4}$$

are satisfied. The discrepancies in Figure 6.3 between data and the simulation have been investigated [6; 9] using data. It was found that the $K^{\pm}$ identification efficiency is too high in the simulation by $(3.0 \pm 1.5)\%$, and that the mis-identification of the $p/\bar{p}$ and $\pi^{\pm}$ background is described correctly in the simulation within 25% uncertainty. Figure 6.4 shows the momentum distribution of identified $K^{\pm}$ for the data and the Monte Carlo simulation. We expect the simulated spectrum to be too soft, as has been observed earlier [6]. This effect is partially canceled by the higher simulated $K^{\pm}$ identification efficiency. Thus data and the simulation agree well in the total number of tagged $K^{\pm}$ candidates. The observed agreement between data and the simulation in the $K^{\pm}$ single tag rate is important since we attempt to constrain features of double tag rates using the data, as discussed in Chapter 8.

The simulated purity of the $K^{\pm}$ sample as a function of momentum is depicted in Figure 6.5.

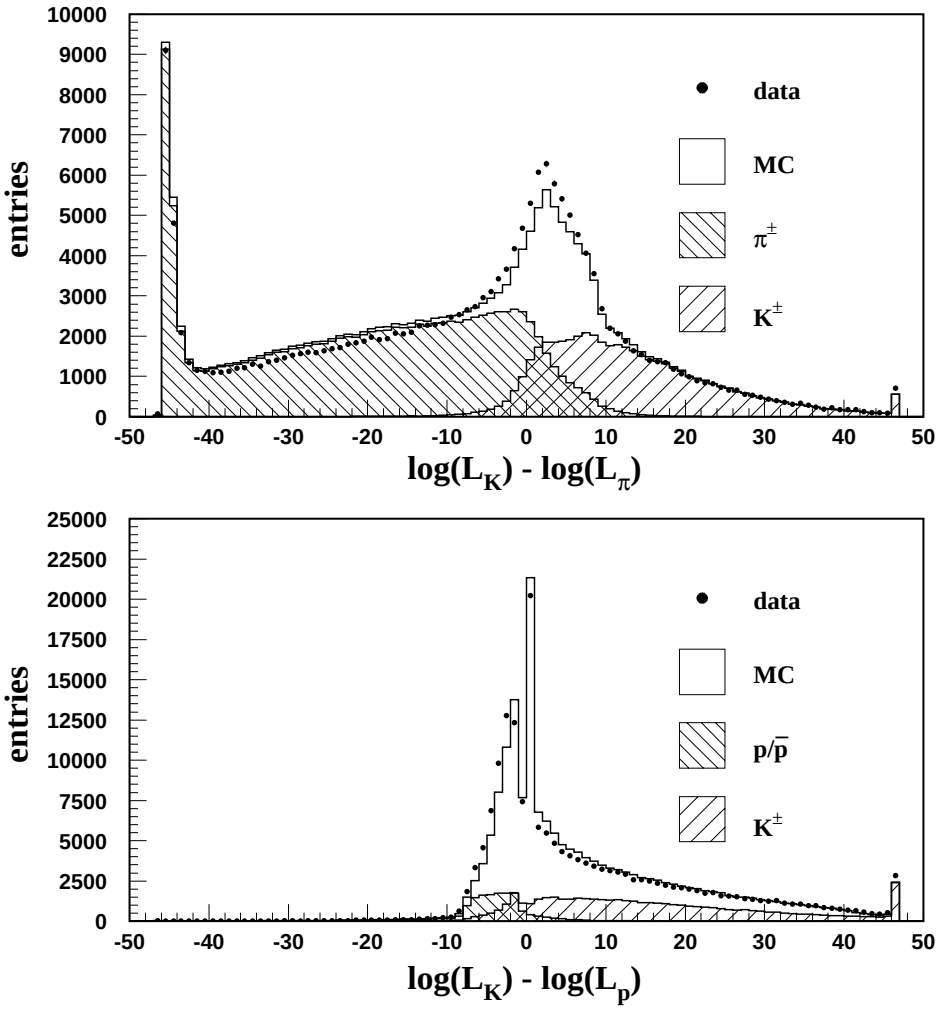

Figure 6.3: The log-likelihood separation between (top) $K^{\pm}$ and $\pi^{\pm}$ candidates and (bottom) $K^{\pm}$ and $p/\bar{p}$ candidates. The dots show the data, and the histograms represent the prediction of the Monte Carlo simulation. The hatched histograms indicate the true $K^{\pm}$, $\pi^{\pm}$, and $p/\bar{p}$ composition, respectively.

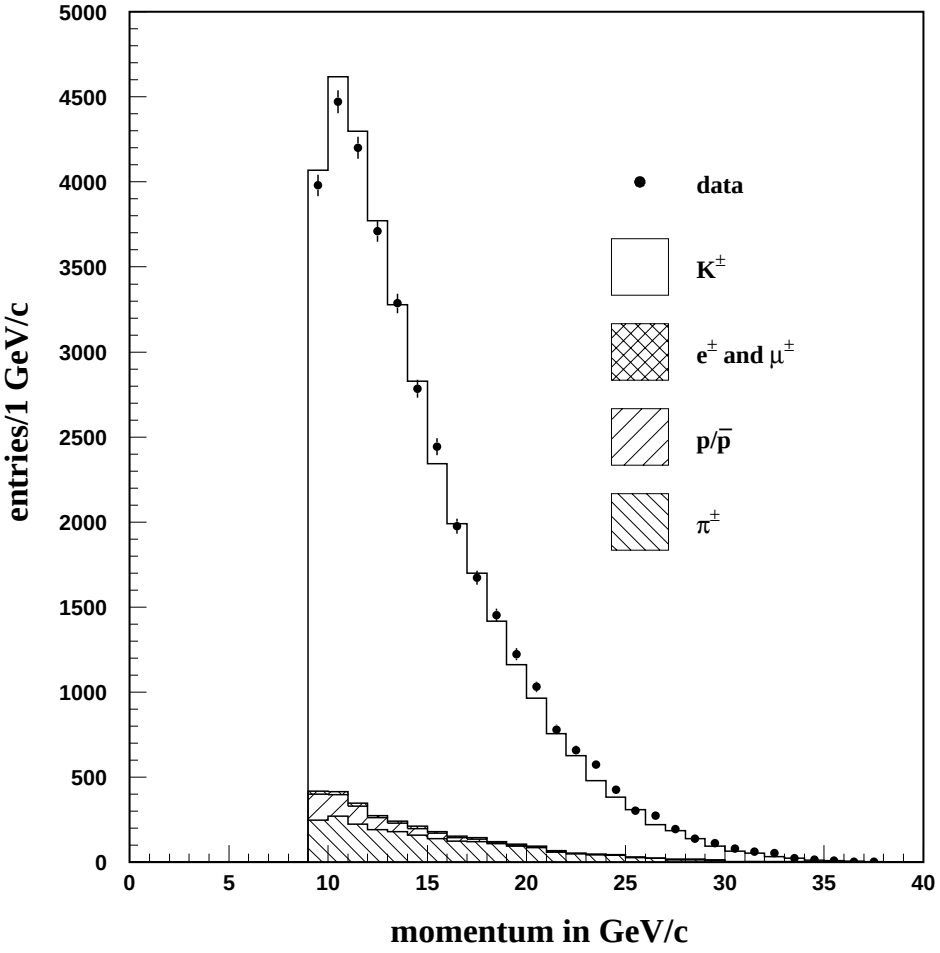

Figure 6.4: The momentum spectrum of identified $K^{\pm}$ candidates. The dots show the data, and the histogram represents the prediction of the Monte Carlo simulation. The background from $\pi^{\pm}$, $p/\bar{p}$, $e^{\pm}$ and $\mu^{\pm}$ in the tagged sample is also indicated. The momentum cut at $p > 9$ GeV/c is given by the $K^{\pm}$ threshold of the CRID gas radiator.

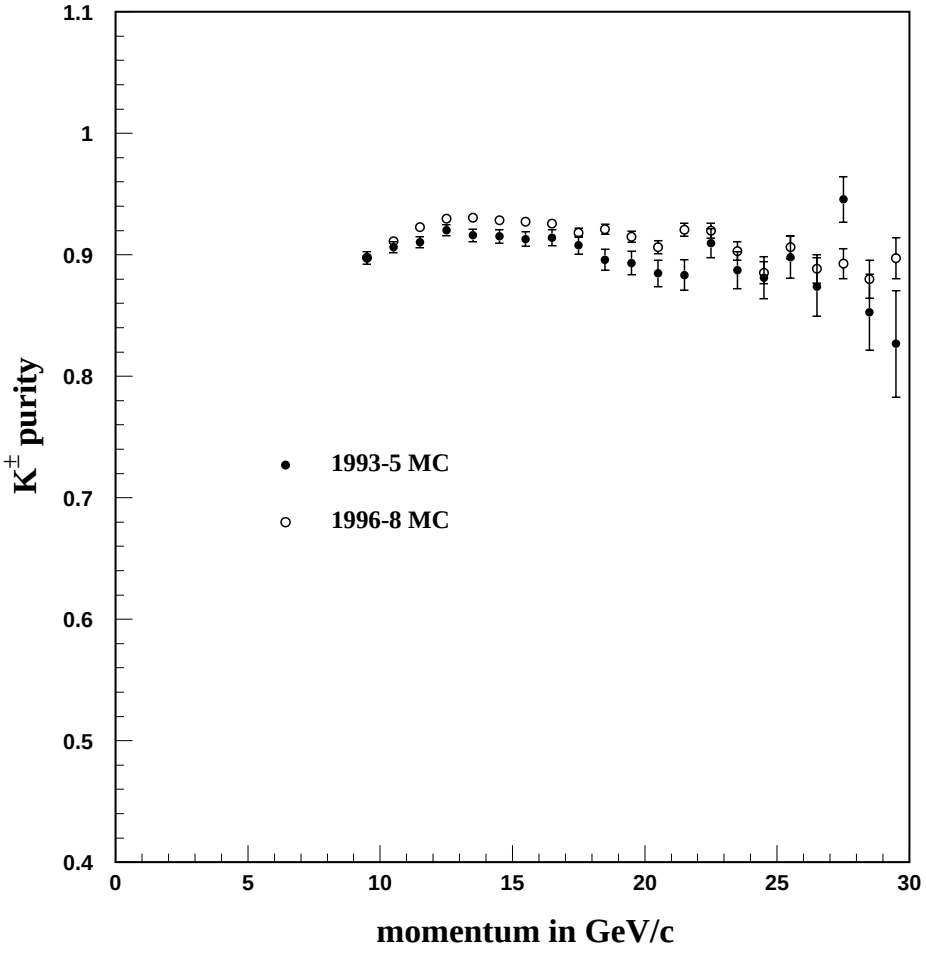

Figure 6.5: The purity of the identified $K^{\pm}$ sample as a function of track momentum, as estimated from the Monte Carlo simulation. The uncertainties shown are statistical only.

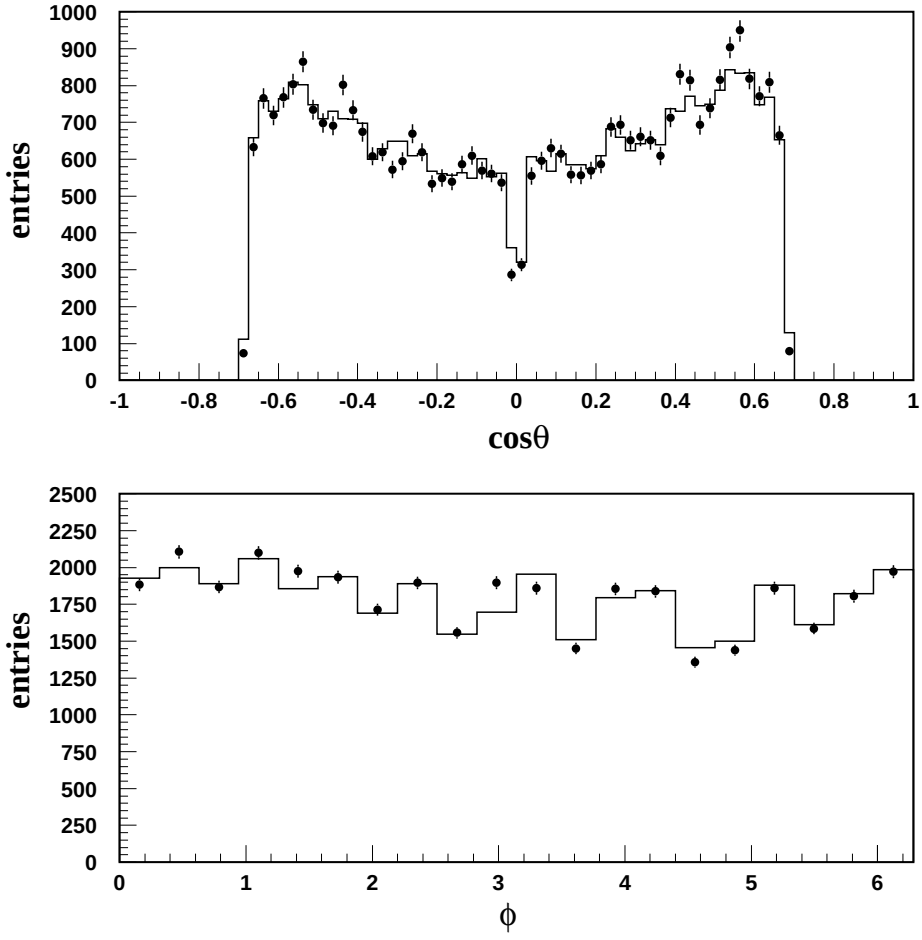

Figure 6.6: The angular acceptance of the identified $K^{\pm}$ sample for the (top) polar and (bottom) azimuthal angle. In the bottom plot, the corresponding TPC boxes in the North and South detector hemispheres are added, e.g. the leftmost bin combines TPC boxes 0 and 20. The dots show the data, and the histograms represent the prediction of the Monte Carlo simulation.

The average purity of the $K^{\pm}$ sample was estimated using the simulation to be 91.5%, with background contributions of 6.3% $\pi^{\pm}$, 1.8% $p/\bar{p}$ and 0.4% for $e^{\pm}$ and $\mu^{\pm}$ combined. Figure 6.6 gives the polar and azimuthal angle distributions of the tagged $K^{\pm}$ sample. The variations in the azimuthal angle show the effect of dead TPCs. The simulation is in good agreement with the data. Table 6.3 summarizes the number of selected $K^{\pm}$ for the three different data run periods.

Table 6.3: Selected $K^{\pm}$ candidate sample for the 1993-1998 data runs.

Run period	$K^{\pm}$ sample
1993-5	9,487
1996	3,551
1997-8	22,910
Total:	35,948

6.2.2 Selection of $\Lambda^0/\bar{\Lambda}^0$ and K^0_s

The generic name of V^0 decay arises from the pair of oppositely charged tracks originating at a neutral decay vertex. We are interested in the charged decay modes of $\Lambda^0(\bar{\Lambda}^0) \rightarrow p(\bar{p})\pi^{\mp}$ ($BR = (63.9 \pm 0.5)\%$ [19]) and $K^0_s \rightarrow \pi^+\pi^-$ ($BR = (68.61 \pm 0.28)\%$ [19]). The reconstruction of the $\Lambda^0(\bar{\Lambda}^0)$ and K^0_s candidates makes use of their long flight distance, accuracy of pointing back to the primary interaction point, and reconstructed mass. In the case of the $\Lambda^0/\bar{\Lambda}^0$, we use CRID information to identify the $p/\bar{p}$ candidate.

In the first step of the reconstruction, a sample of well reconstucted V^0 candidates with momentum $p > 5$ GeV/c is selected. For each of the two tracks forming the V^0 candidate, we require a momentum transverse to the beam direction of $p_{\perp} > 150$ MeV/c, a track acceptance within $|\cos\theta| < 0.9$, and a minimum of at least 30 hits in the CDC. The V^0 candidates are reconstructed

from pairs of oppositely charged tracks if they are separated by less than 15 mm at their point of closest approach, and if their χ^2_{vtx} fit to a common vertex has a probability of larger than 2%.

In this analysis, we want to select high-momentum $\Lambda^0/\bar{\Lambda}^0$ and K^0_s. We therefore apply a momentum cut of $p > 5$ GeV/c since the tagging efficiencies [5] for $\Lambda^0/\bar{\Lambda}^0$ and K^0_s drop rapidly below that momentum. V^0 candidates containing tracks which were previously identified as $K^{\pm}$ candidates are removed. The selected V^0 sample consists of $\Lambda^0/\bar{\Lambda}^0$, K^0_s, as well as gamma conversions and fake decay candidates. The next steps describe the cuts used to purify this sample.

On average, the charge multiplicity in hadronic Z^0 decays is roughly 20 charged tracks, leading to a large combinatorial background, i.e. to fake decays. The following cuts are designed to reduce this background. The V^0 candidate is required to have a normalized flight distance with respect to the IP of $l_{norm} > 5$, where the normalization is given by the estimated uncertainty on the decay length resulting from uncertainties of the position of the secondary vertex and the IP. Figure 6.7 shows the normalized decay length for data and the Monte Carlo simulation.

The combinatorial background is further reduced by requiring that each charged track in a secondary vertex reconstucted outside the VXD has at most one associated VXD hit. Finally, the accuracy with which the V^0 candidate points back to the IP is an effective means of reducing the combinatorial background. In the plane perpendicular to the beam direction, we require the angle, ϕ_{2D} [5], between the momentum of the V^0 candidate and the line connecting the IP with the secondary vertex, to be within $\phi_{2D} < C \cdot (2 + 20/p_{\perp} + 5/p^2_{\perp})$, where ϕ_{2D} is given in units of mrad, $p_{\perp}$ is given in in units of GeV/c, and we use $C = 1.75$ for $\Lambda^0/\bar{\Lambda}^0$ candidates and $C = 2.50$ for K^0_s candidates.

The V^0 finding algorithm computes the invariant masses for $\Lambda^0/\bar{\Lambda}^0$, K^0_s and gamma conversion candidates by assigning the appropriate masses to the two tracks, and using the momenta of the two tracks at the position of the fitted secondary vertex. The background from gamma

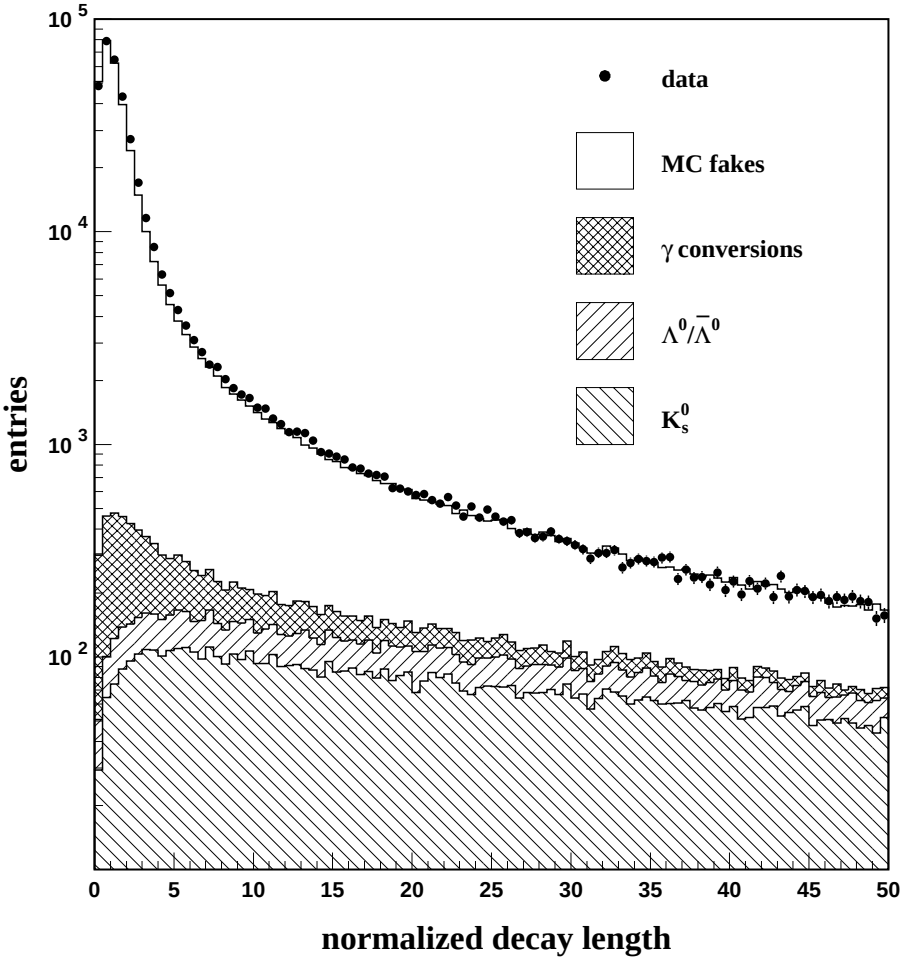

Figure 6.7: The normalized decay length for V^0 candidates with $p > 5$ GeV/c. The dots show the data, and the prediction of the Monte Carlo simulation is represented by the histogram. The contributions of fake decays, γ conversions, $\Lambda^0/\bar{\Lambda}^0$ and K_s^0 are indicated separately.

conversions, reconstructed assuming the electron mass for both charged tracks, is removed by requiring $m_{ee} > 100$ MeV/c^2.

For K_s^0 candidates, we calculate $m_{\pi\pi}$ by assigning the charged pion mass to each track, and for $\Lambda^0/\bar{\Lambda}^0$, we compute $m_{p\pi}$ using the proton mass for the higher momentum track and the pion mass for the other track. The mass assignments for the $\Lambda^0/\bar{\Lambda}^0$ arise from its decay kinematics, which results in a higher momentum of the $p/\bar{p}$ in the laboratory frame than the $\pi^{\mp}$ for $\Lambda^0/\bar{\Lambda}^0$ with momentum above 301 MeV/c.

Additional cuts are imposed to select the $\Lambda^0/\bar{\Lambda}^0$ and K_s^0 samples. The invariant mass cuts on the $m_{p\pi}$ and $m_{\pi\pi}$ distributions, i.e. the different mass resolutions $\sigma_{m_{p\pi}}$ and $\sigma_{m_{\pi\pi}}$ described below, are parametrized as linear functions of the V^0 momentum.

In the case of the $\Lambda^0/\bar{\Lambda}^0$ candidate, we next use information from the CRID to identify the $p/\bar{p}$ candidate. Since the $\Lambda^0/\bar{\Lambda}^0$ will be used to sign the strangeness of the event hemisphere, we also remove the background from K_s^0. We identify the $p/\bar{p}$ candidate if the log-likelihood separation between this hypothesis and the π^+/π^- hypothesis satisfies $\log\mathcal{L}_{p/\bar{p}} - \log\mathcal{L}_{\pi^{\pm}} > 0$. If CRID information on the $p/\bar{p}$ candidate is unavailable, we increase the cut on the normalized flight distance with respect to the IP to $l_{norm} > 10$, and require $|m_{\pi\pi} - m_{K_s^0}| < 2\sigma_{m_{\pi\pi}}$. Figure 6.8 gives the $m_{p\pi}$ distribution for the selected $\Lambda^0/\bar{\Lambda}^0$ sample. The simulated $m_{p\pi}$ peak is too narrow compared to the data, but the agreement between data and the Monte Carlo simulation is good in the sidebands, giving confidence that the estimated level of background is reliable.

The $\Lambda^0/\bar{\Lambda}^0$ candidates are identified by requiring $|m_{p\pi} - m_{\Lambda^0}| < 2\sigma_{m_{p\pi}}$. The momentum distribution for the selected $\Lambda^0/\bar{\Lambda}^0$ sample is displayed in Figure 6.9. The simulation spectrum is expected to be too soft [109]. This effect is offset by our simulated $\Lambda^0/\bar{\Lambda}^0$ tagging efficiency being too high. Thus there is quite good agreement for $p > 15$ GeV/c. However, the Monte Carlo simulation predicts too many low-momentum $\Lambda^0/\bar{\Lambda}^0$ candidates. For the reason given in the

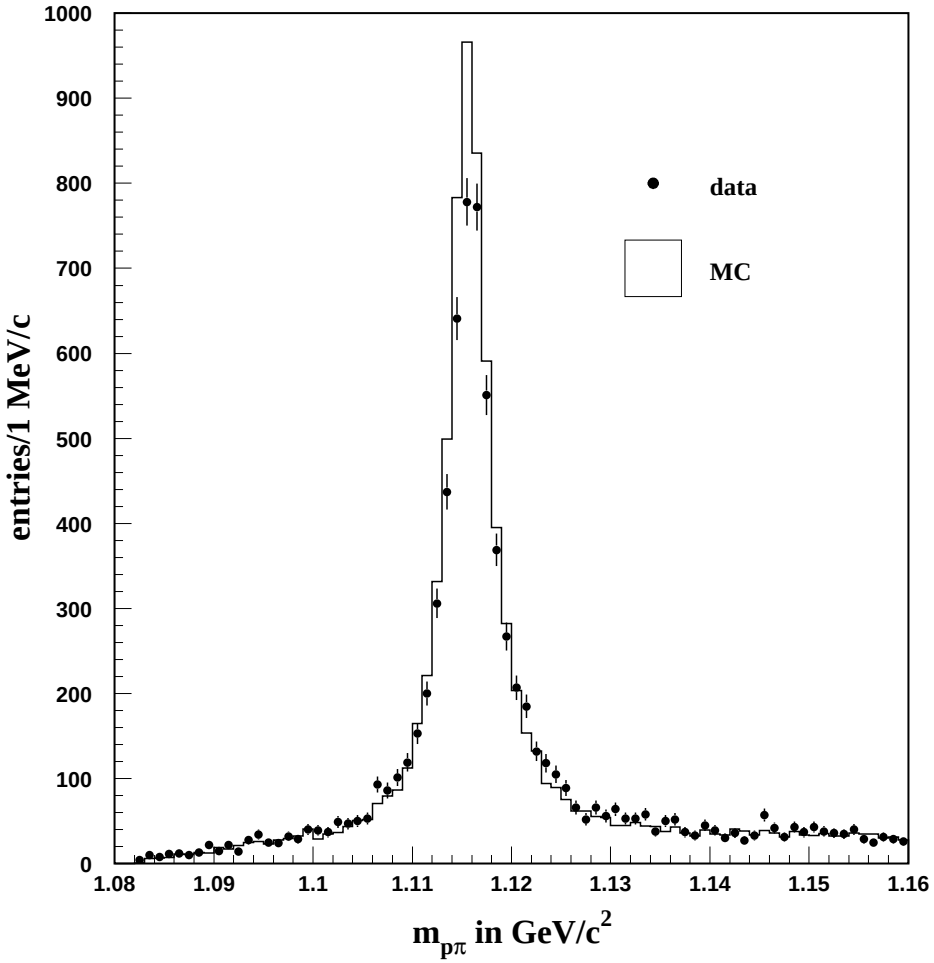

Figure 6.8: The invariant mass $m_{p\pi}$ of $\Lambda^0/\bar{\Lambda}^0$ candidates with momentum $p > 5$ GeV/c. The dots (histogram) represent the data (Monte Carlo simulation).

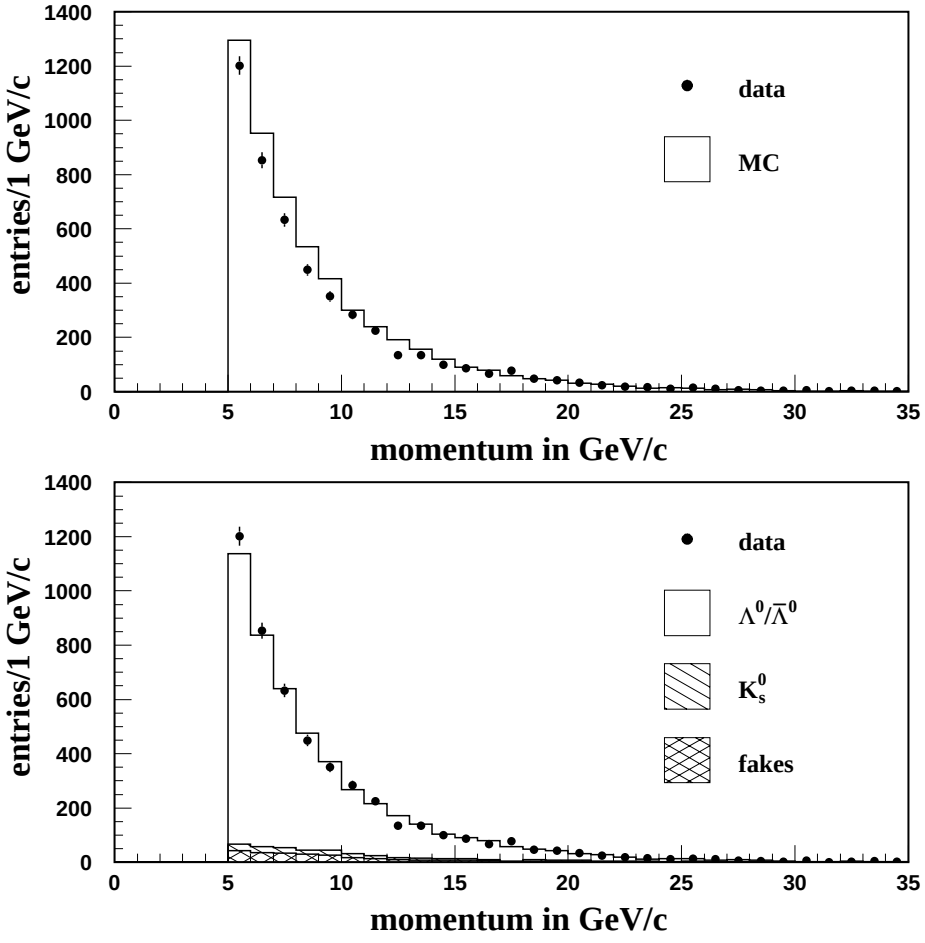

Figure 6.9: The momentum of the selected $\Lambda^0/\bar{\Lambda}^0$ candidate sample (top) before and (bottom) after applying a momentum-independent correction to the number of simulated true $\Lambda^0/\bar{\Lambda}^0$ with $p < 15$ GeV/c. The dots represent the data, and the background from K_s^0 and fakes is indicated. The γ conversion background is negligible.

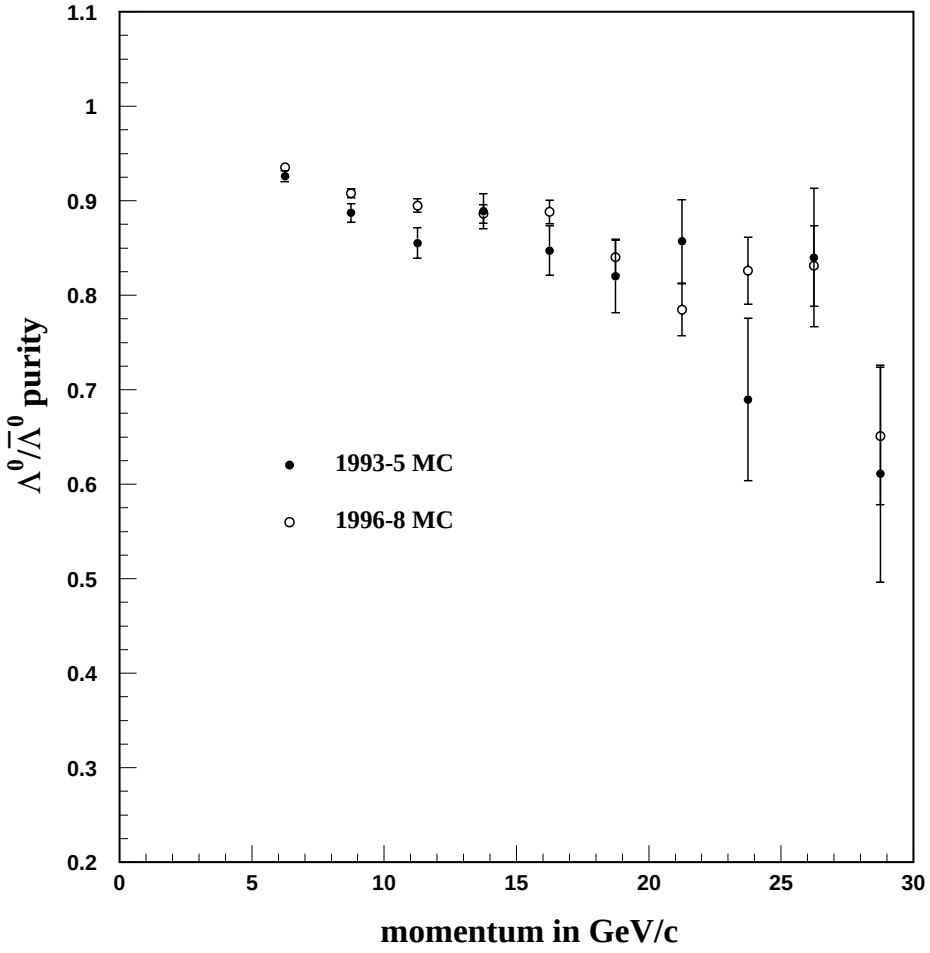

Figure 6.10: The purity of the selected $\Lambda^0/\bar{\Lambda}^0$ candidate sample as a function of momentum, as estimated from the Monte Carlo simulation. The uncertainties shown are statistical only.

case of the $K^{\pm}$ sample, we correct this discrepancy in the simulation. We apply a momentum-independent correction factor to the number of simulated true $\Lambda^0/\bar{\Lambda}^0$ candidates with $p < 15$ GeV/c, which rejects a total of 12.5% of the simulated true $\Lambda^0/\bar{\Lambda}^0$ sample within this momentum region. However, this procedure maintains the absolute background which is seen from the $m_{p\pi}$ sidebands in Figure 6.8 to be well simulated. The effect of this correction on the final result will be discussed in Chapter 8.

The corrected simulation predicts that the purity of the $\Lambda^0/\bar{\Lambda}^0$ sample is 90.7%, with background contributions of 5.5% fake decays and 3.8% K^0_s. The background from γ conversions is negligible. Figure 6.10 illustrates the purity of the selected $\Lambda^0/\bar{\Lambda}^0$ sample as a function of momentum. Table 6.4 summarizes the number of selected $\Lambda^0/\bar{\Lambda}^0$ candidates for the three different data run periods.

Table 6.4: Selected $\Lambda^0/\bar{\Lambda}^0$ candidate sample for the 1993-1998 data runs.

Run period	$\Lambda^0/\bar{\Lambda}^0$ sample
1993-5	1,249
1996	482
1997-8	3,114
Total:	4,845

For the selection of the K^0_s sample, candidates containing tracks which were previously identified as $\Lambda^0/\bar{\Lambda}^0$ are removed. Pairs of tracks with $|m_{\pi\pi} - m_{K^0_s}| < 2\sigma_{m_{\pi\pi}}$ are identified as K^0_s. For the K^0_s sample, the remaining $\Lambda^0/\bar{\Lambda}^0$ contamination presents no difficulty since the K^0_s candidate cannot be used to sign the strangeness of a tag. Figure 6.11 shows the $m_{\pi\pi}$ distribution for the selected K^0_s sample. Figure 6.12 gives the momentum distribution for the K^0_s sample. Similar to the case for the $\Lambda^0/\bar{\Lambda}^0$, we expect the simulated K^0_s spectrum to be too soft [109], with the effect being

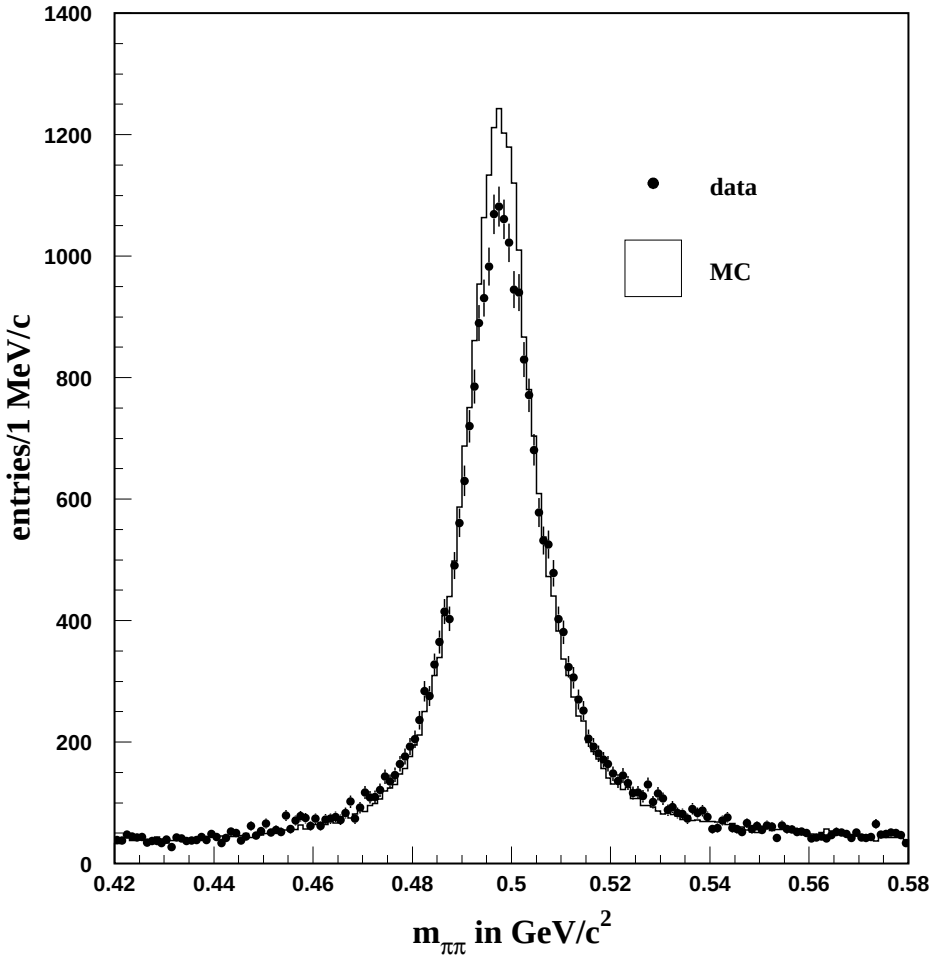

Figure 6.11: The invariant mass $m_{\pi\pi}$ of K^0_s candidates with momentum $p > 5$ GeV/c. The dots (histogram) represent the data (Monte Carlo simulation).

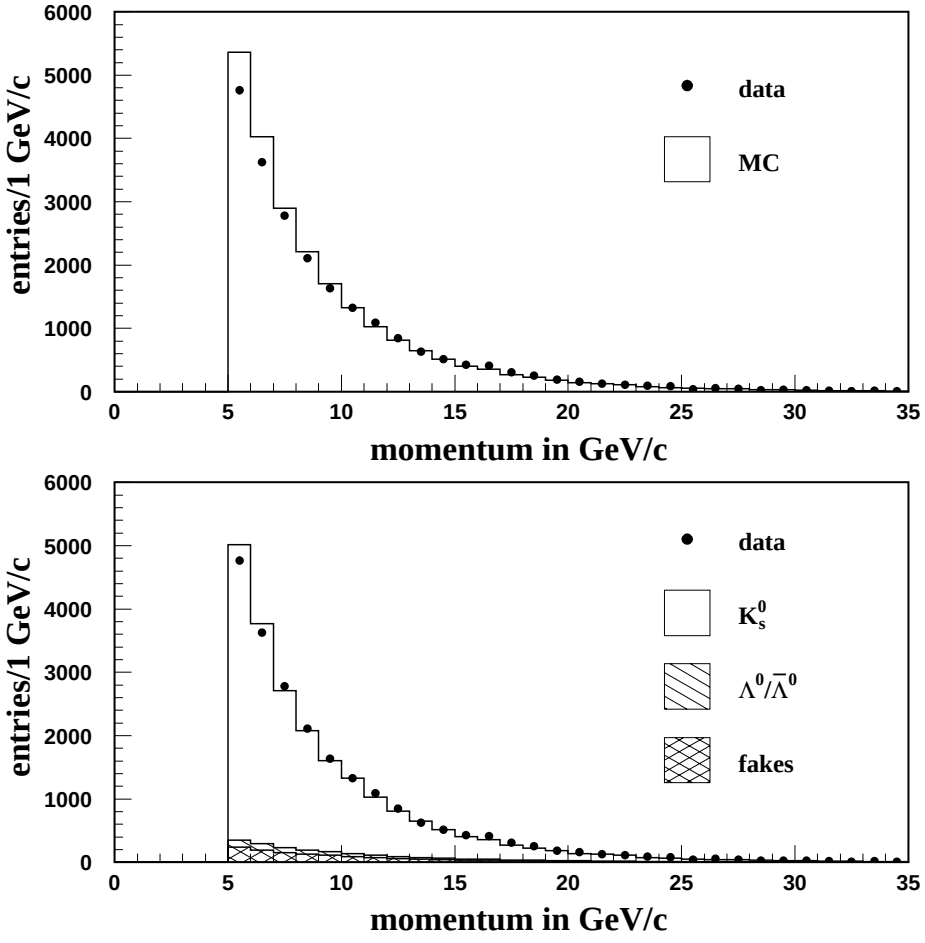

Figure 6.12: The momentum of the selected K_s^0 candidate sample (top) before and (bottom) after applying a momentum-independent correction to the number of simulated true K_s^0 with $p < 10$ GeV/c. The dots represent the data, and the background from $\Lambda^0/\bar{\Lambda}^0$ and fakes is indicated. The γ conversion background is negligible.

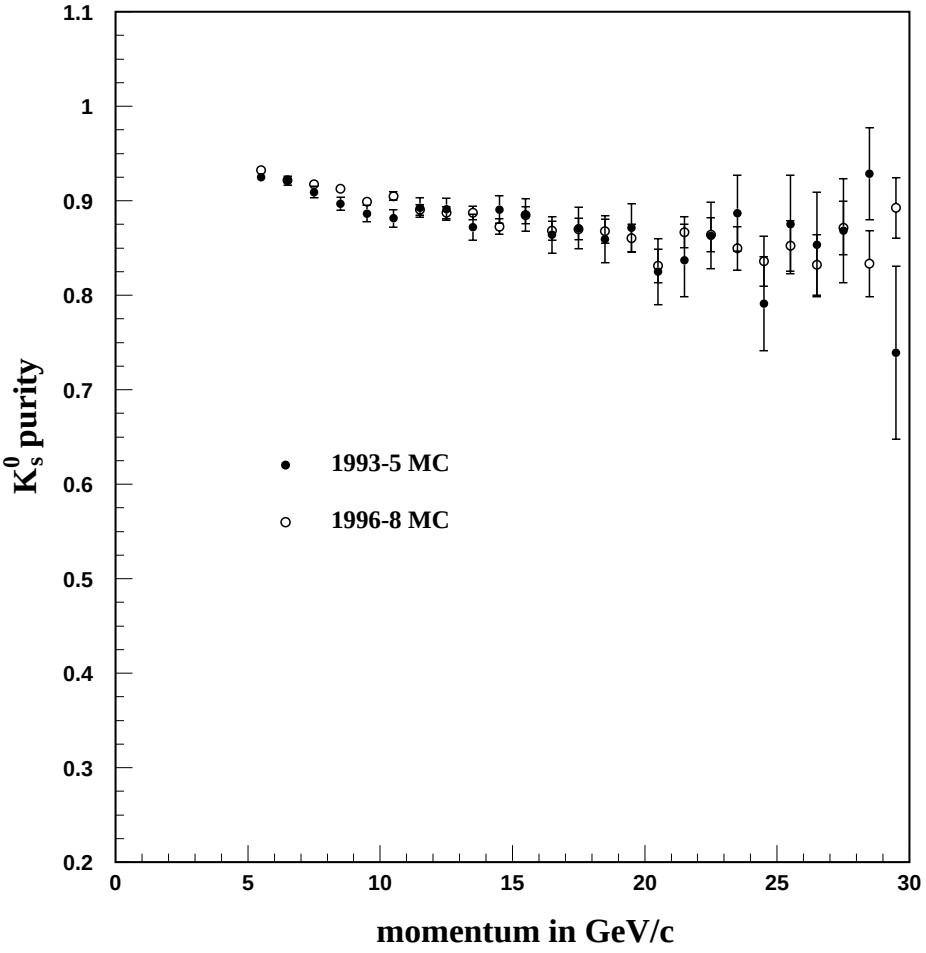

Figure 6.13: The purity of the selected K^0_s candidate sample as a function of momentum, as estimated from the Monte Carlo simulation. The uncertainties shown are statistical only.

offset by our simulated K_s^0 tagging efficiency being too high. The resulting agreement for $p > 10$ GeV/c is rather good. However, the Monte Carlo simulation predicts too many low-momentum K_s^0 candidates, and we correct this discrepancy in the simulation. We apply a momentum-independent correction factor to the number of simulated true K_s^0 candidates with $p < 10$ GeV/c which rejects a total of 6.9% of the simulated true K_s^0 sample within this momentum region. The procedure maintains the absolute background which is seen from the $m_{\pi\pi}$ sidebands in Figure 6.11 to be well simulated. The effect of this correction on the final result will be discussed in Chapter 8.

The corrected simulation predicts that the purity of the K_s^0 sample is 90.7%, with backgrounds of 6.3% fake decays and 3.0% $\Lambda^0/\bar{\Lambda}^0$. The background from γ conversions is negligible. Figure 6.13 depicts the purity of the selected K_s^0 sample as a function of momentum. The number of selected K_s^0 candidates for the three different data run periods is given in Table 6.5.

Table 6.5: Selected K_s^0 candidate sample for the 1993-1998 data runs.

Run period	K_s^0 sample
1993-5	5,529
1996	2,362
1997-8	13,885
Total:	21,776

6.3 Tagging of the High Purity $s\bar{s}$ Sample

The $K^{\pm}$, $\Lambda^0/\bar{\Lambda}^0$ and K_s^0 samples are used to tag s and $\bar{s}$ jets. Each event is divided into two hemispheres by a plane perpendicular to the thrust axis, and each of the two hemispheres is required to contain at least one identified strange particle. For hemispheres with multiple strange particles we only consider the one with the highest momentum. We require at least one of the

two hemispheres to have definite strangeness (i.e. to contain a $K^{\pm}$ or $\Lambda^0/\bar{\Lambda}^0$). In events with two hemispheres of definite strangeness, the two hemispheres are required to have opposite strangeness (e.g. K^+K^-). Thus 5 tagging modes can be formed. Compared with a single tag, this procedure substantially increases the $s\bar{s}$ purity at the expense of $u\bar{u} + d\bar{d}$ contamination, and thus reduces the model dependence of the measurement, as discussed in Chapter 8.

Table 6.6 summarizes the event statistics of the selected sample for data and simulation for each of the 5 tagging modes. The number of events for each mode shown is in good agreement with the Monte Carlo prediction. The $K^{\pm}K^0_s$ and K^+K^- modes dominate the event sample, the $K^+\Lambda^0, K^-\bar{\Lambda}^0$ and $\Lambda^0K^0_s, \bar{\Lambda}^0K^0_s$ modes have similar and rather low statistics, and the statistics for the $\Lambda^0\bar{\Lambda}^0$ mode is very small.

Table 6.6: Summary of the selected event sample for 5 tagging modes in data and simulation.

Mode	Data Events	MC prediction
K^+K^-	1290	1312.2
$K^+\Lambda^0, K^-\bar{\Lambda}^0$	219	213.5
$\Lambda^0\bar{\Lambda}^0$	17	13.7
$K^{\pm}K^0_s$	1580	1617.3
$\Lambda^0K^0_s, \bar{\Lambda}^0K^0_s$	193	194.1
Total:	3299	3350.8

The simulated flavor compositions for the 5 tagging modes are listed in Table 6.7. We may expect that modes with two signed tagged hemispheres possess higher $s\bar{s}$ purity as compared to modes using the unsigned K^0_s. In fact, the K^+K^- mode has the highest $s\bar{s}$ purity, followed by the $K^+\Lambda^0, K^-\bar{\Lambda}^0$ mode. The background contributions from $u\bar{u}$ and $d\bar{d}$ are roughly similar. In the K^+K^- mode, for example, the primary $u(\bar{u})$ quark can produce a leading $K^+(K^-)$ by picking up an $\bar{s}(s)$ quark from the vacuum; and in a $d\bar{d}$ event, the primary $d(\bar{d})$ quark may form

Table 6.7: Summary of the flavor composition, N_f (in %), and analyzing powers, a_f, of the selected event sample for 5 tagging modes in the simulation.

Mode	N_u	N_d	N_s	N_c	N_b	a_u	a_d	a_s	a_c	a_b
K^+K^-	8.4	5.5	72.9	12.9	0.4	-0.75	-0.36	0.95	0.90	0.76
$K^+\Lambda^0, K^-\bar{\Lambda}^0$	10.6	9.3	66.2	12.5	1.5	-0.32	0.02	0.89	0.78	0.66
$\Lambda^0\bar{\Lambda}^0$	12	10	57	13	8	0.4	0.0	0.7	0.2	0.8
$K^\pm K^0_s$	8.7	10.5	60.3	18.7	1.8	-0.47	-0.15	0.70	0.58	0.52
$\Lambda^0 K^0_s, \bar{\Lambda}^0 K^0_s$	9.9	18.5	50.1	17.3	4.2	0.15	-0.11	0.32	0.24	0.26

a $K^{*0} \to K^+\pi^-(\bar{K}^{*0} \to K^-\pi^+)$ by combining with an $\bar{s}(s)$ quark from the vacuum. The heavy flavor background is dominated by $c\bar{c}$. The combined $s\bar{s}$ purity of all modes is 65.0% in the simulation, and the predicted background in the selected event sample consists of 8.8% $u\bar{u}$, 8.9% $d\bar{d}$, 15.9% $c\bar{c}$, and 1.4% $b\bar{b}$ events. As discussed in Chapter 8, the relative light flavor background level, $(N_u + N_d)/N_s$, can be constrained from the data, and we may assume that the heavy flavor background, $(N_c + N_b)$, is well described by the simulation.

We define the analyzing power in $q\bar{q}$ events with respect to the quark, q:

$$a_q = \frac{N_q^r - N_q^w}{N_q^r + N_q^w} \tag{6.5}$$

where N^r denotes the number of $q\bar{q}$ events in which the tagging particle of negative strangeness is found in the true q hemisphere, and N_q^w gives the number of $q\bar{q}$ events in which the tagging particle of negative strangeness is found in the true $\bar{q}$ hemisphere. This definition leads to a positive analyzing power for $s\bar{s}$ events, since e.g. in the K^+K^- mode, a leading $K^-(K^+)$ tagging the $s(\bar{s})$ hemisphere forms a right sign tag. Table 6.7 shows the simulated analyzing power for the 5 tagging modes. As is the case for the $s\bar{s}$ flavor compositions, modes with two signed tagged hemispheres are expected to have high $s\bar{s}$ analyzing power. The K^+K^- mode has a substantially higher

$s\bar{s}$ analyzing power than the other modes, followed again by the $K^+\Lambda^0, K^-\bar{\Lambda}^0$ mode. Negative analyzing powers, e.g. for the K^+K^- mode in $u\bar{u}$ events, arise from the primary $u(\bar{u})$ quark combining with an $\bar{s}(s)$ quark from the vacuum to produce a leading $K^+(K^-)$. The average $s\bar{s}$ analyzing power for all modes is predicted by the simulation to be 0.81.

Tagging modes with high $s\bar{s}$ flavor fraction and analyzing power and good statistics will be useful for the analysis. Table 6.6 and Table 6.7 indicate that the K^+K^- mode and the $K^\pm K_s^0$ mode fulfill these criteria.

The $K^+\Lambda^0, K^-\bar{\Lambda}^0$ mode has high $s\bar{s}$ flavor fraction and analyzing power, but the statistics is small. Furthermore, the calibration procedure for a_s and $(N_u + N_d)/N_s$, presented in Chapter 8, applies to the K^+K^- mode and the $K^\pm K_s^0$ mode, but a similar calibration cannot be performed on the tagging modes involving a $\Lambda^0/\bar{\Lambda}^0$ due to the lack of statistics.

We note that the $K^+\Lambda^0, K^-\bar{\Lambda}^0$ mode, the $\Lambda^0 K_s^0, \bar{\Lambda}^0 K_s^0$ mode, and the $\Lambda^0\bar{\Lambda}^0$ mode have been helpful in providing cross checks, e.g. the number of tagged events in data and the simulation agrees for these modes, and the simulated a_s values fit into the pattern set by the K^+K^- mode and the $K^\pm K_s^0$ mode. However, given their small statistical contribution and the absence of a calibration scheme which allows us to address their light flavor systematics, we omit the $K^+\Lambda^0, K^-\bar{\Lambda}^0$ mode, the $\Lambda^0 K_s^0, \bar{\Lambda}^0 K_s^0$ mode, and the $\Lambda^0\bar{\Lambda}^0$ mode from further consideration.

6.4 Polar Angle Distributions of the Strange Quark

The strangeness of the tagged particle is used to tag the strangeness of the event hemisphere. The initial s quark direction is approximated by the thrust axis, $\hat{t}$, of the event, signed to point in the

direction of negative strangeness:

$$x = \cos\theta_s = S\frac{\vec{p}\cdot\hat{t}}{|\vec{p}\cdot\hat{t}|}t_z, \tag{6.6}$$

where S and $\vec{p}$ denote the strangeness and the momentum of the tagging particle, respectively. The polar angle distributions of the tagged strange quark for the K^+K^- mode and the $K^\pm K^0_s$ mode are shown in Figure 6.14 and Figure 6.15, respectively, for left-handed and right-handed electron beams. Production asymmetries in $\cos\theta_s$, of opposite sign for the beams of negative and positive e^- beam polarization, are observed for each mode.

The $\cos\theta_s$ range of the distributions arises from the cut on the thrust axis in the hadronic event selection. The drop in the distributions in the outermost bins is caused by the $|\cos\theta| < 0.68$ acceptance cut for the identification of $K^\pm$ candidates by the CRID gas system, and the degrading reconstruction efficiency for K^0_s candidates in these bins.

In both modes, the signal is larger than the background, especially for the K^+K^- mode. The decay chain of the heavy primary quarks, $c \to s$ and $b \to c \to s$, respectively, can produce a K^-, causing the $c\bar{c} + b\bar{b}$ background to display a production asymmetry of the same sign to the entire distribution. The $c\bar{c}$ contribution dominates the heavy flavor background. The combined $u\bar{u} + d\bar{d}$ background shows a production asymmetry of the opposite sign to the entire distribution. We are especially sensitive to the slope and, to a lesser extent, to the size of the $u\bar{u}+d\bar{d}$ background in the sense that both will contribute sizable systematic uncertainties. In the next Chapter, we discuss how A_s is extracted from these polar angle distributions.

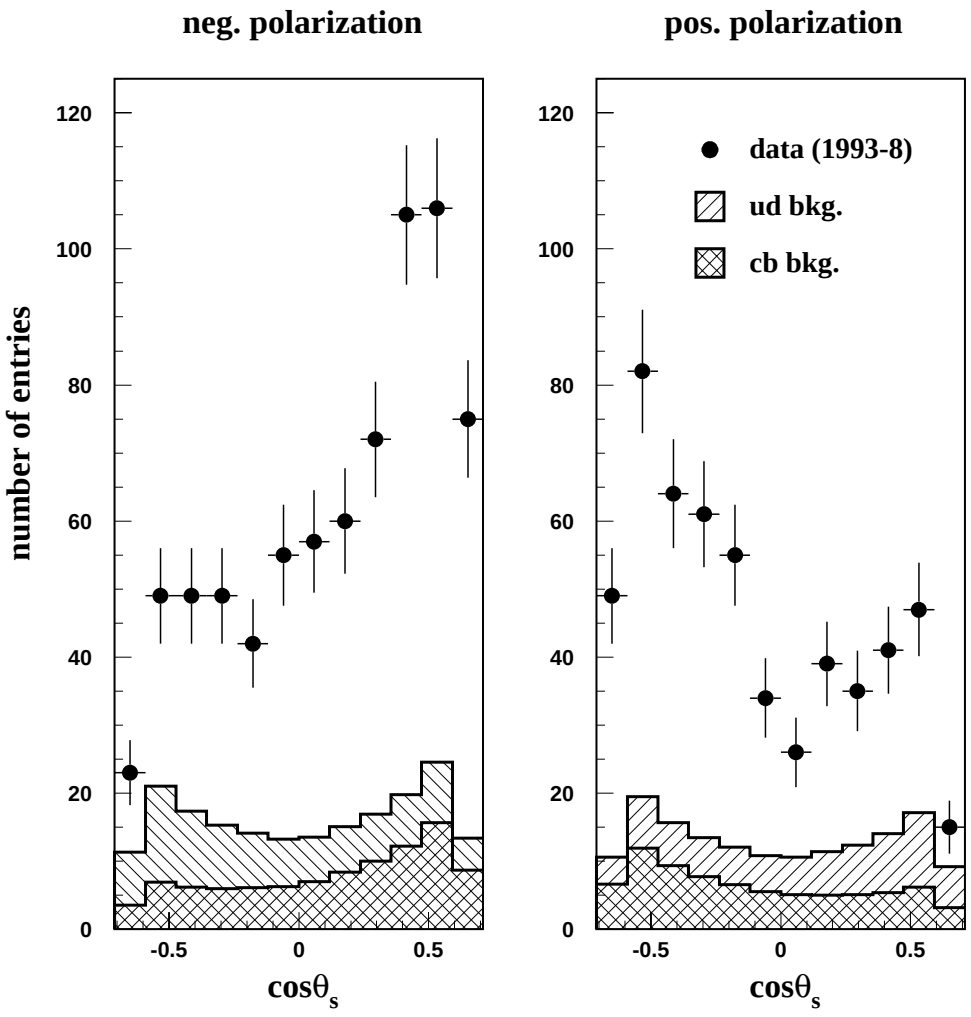

Figure 6.14: The polar angle distributions of the tagged strange quark, for (left) negative and (right) positive electron beam polarization, for the K^+K^- mode. The dots show data, and the estimates of the non-$s\bar{s}$ backgrounds are indicated by the hatched histograms.

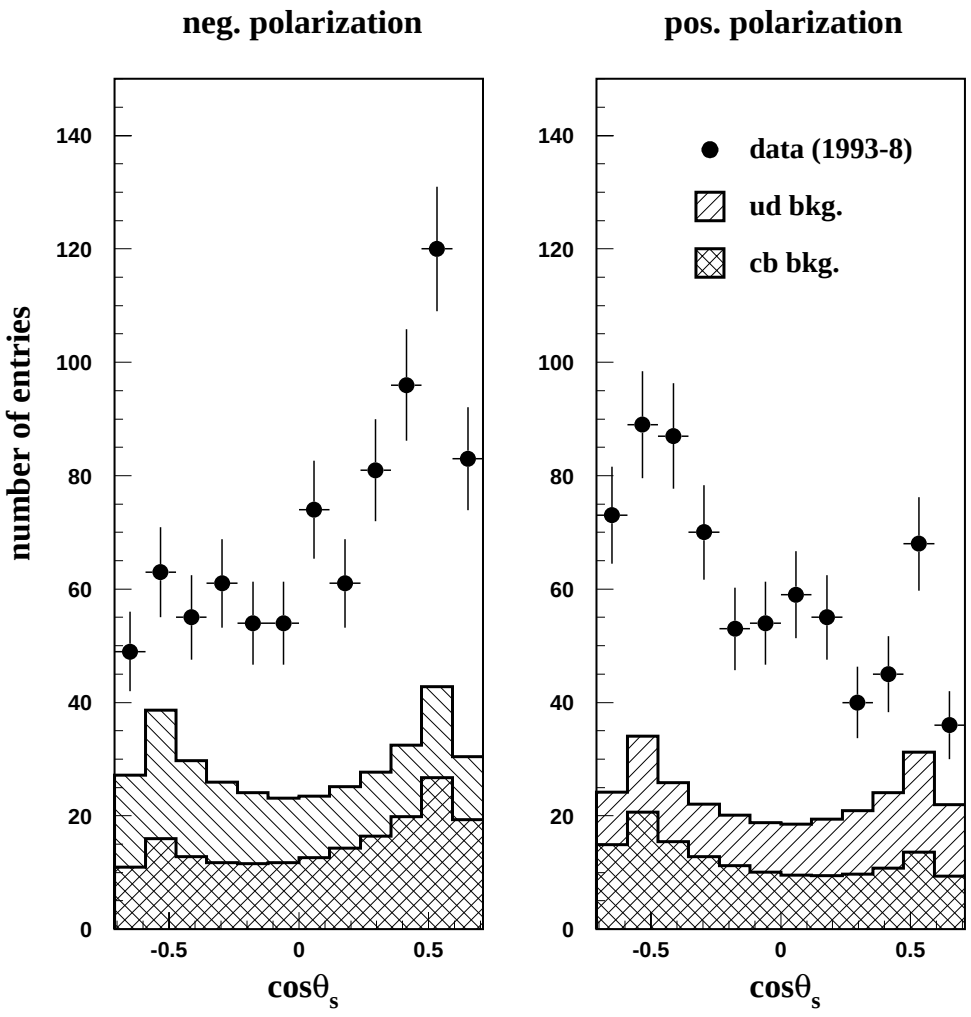

Figure 6.15: The polar angle distributions of the tagged strange quark, for (left) negative and (right) positive electron beam polarization, for the $K^{\pm}K^0_s$ mode. The dots show data, and the estimates of the non-$s\bar{s}$ backgrounds are indicated by the hatched histograms.

Chapter 7

Extraction of the Strange Quark Coupling, A_s

We derive A_s from the polar angle distributions of the tagged strange quark shown in Figure 6.14 and Figure 6.15 for the K^+K^- mode and the $K^\pm K^0_s$ mode respectively by means of a standard unbinned maximum likelihood method. This fitting procedure and the input parameters to the fit are discussed and the fit results are presented in this Chapter.

7.1 Unbinned Maximum Likelihood Method

Rather than using $\tilde{A}^f_{FB}$ in Equation (2.26) to extract A_s we apply an unbinned maximum likelihood procedure directly to the polar angle distributions. Since treating each event individually we maximize the use of information. We use the differential production cross section given in Equation (2.17) to construct the likelihood function $\mathcal{L}$:

$$\mathcal{L} = \prod_{k=1}^{N_{data}} \left\{ (1 - A_e P_e)(1 + x_k^2) + 2(A_e - P_e) \sum_f (N_f[1 + \delta] a_f A_f x_k) \right\} \tag{7.1}$$

where the product runs over the tagged events N_{data} in the tagging modes; A_f represents the coupling parameter; P_e is the longitudinal polarization of the electron beam; $x_k = (\cos\theta_s)_k$ gives the strangeness-signed thrust axis; $N_f = N_{events} R_f \epsilon_f$ denotes the number of events in the sample of flavor f ($f = u, d, s, c, b$) in terms of the number of selected hadronic events N_{events} $R_f =$,($Z^0 \to f\bar{f}$)/,($Z^0 \to$ hadrons) and the tagging efficiencies ϵ_f; $\delta = -0.013$ corrects for the effects

of hard gluon radiation [110]; and a_f denotes the analyzing power for tagging the f rather than the $\bar{f}$ direction. Understanding these input parameters and their uncertainties is essential to this analysis. Their impact on the A_s measurement is summarized below.

The properties of heavy flavor production [1] and decay have attracted substantial experimental attention. Our B hadron decay model [64; 75] was tuned to measurements performed by ARGUS [76] and CLEO [77]. The effectiveness of the $K^{\pm}$ has been studied at the SLD in A_c [99] and A_b [100] analyses. Therefore the parameters ϵ_c, ϵ_b, and a_c, a_b for the heavy flavors are taken from the Monte Carlo simulation since a number of independent measurements lead us to believe these parameters to be reliable within well defined uncertainties. The world average experimental measurements of the parameters A_c, A_b, R_c, R_b [1] were used. We thus employ the heavy flavor model to give an absolute prediction of the heavy flavor backgrounds and analyzing powers. The corresponding systematic uncertainties are small.

For the light flavors, the relevant parameters in the fitting function are derived where possible from the data to reduce the model dependence. The total number of light flavor events, N_{uds}, for each tagging mode is determined by subtracting the number of heavy flavor events, obtained from the simulation, from the number of tagged events. The values for the ratio N_{ud}/N_s and the $s\bar{s}$ analyzing power, a_s, depend on the tagging mode as shown in Table 6.7; these parameters are determined from the simulation and are constrained using the data. The $(u\bar{u} + d\bar{d})$ analyzing power, a_{ud}, for each mode is estimated to be $-a_s/2$. Our statistics is not high enough to obtain a useful constraint on that quantity from the data, and the corresponding systematic uncertainty is large. The coupling parameters A_u and A_d are set to the Standard Model values.

The experimental uncertainty in the polarization of the electron beam is well understood, and the values are summarized in Table 3.1. The effects of hard gluon radiation [110; 111] are taken into account, and the corresponding uncertainty is small. The measured uncertainty on A_e [1] is very

small. The systematic uncertainties arising from the limited knowledge on the input parameters to the fit are described in more detail in Chapter 8.

7.2 Results of the Likelihood Fits

The likelihood fits yield for the K^+K^- mode:

$$A_s = 0.86 \pm 0.08(stat.) \tag{7.2}$$

and for the $K^\pm K^0_s$ mode:

$$A_s = 0.96 \pm 0.12(stat.). \tag{7.3}$$

Due to its high $s\bar{s}$ purity and high $s\bar{s}$ analyzing power the K^+K^- mode has a smaller statistical uncertainty than the $K^\pm K^0_s$ mode, although the $K^\pm K^0_s$ mode comprises more tags. For the purpose of evaluating the fit quality, we constructed histograms from the fitted values for A_s and the input parameters to the fits. The fit quality of the likelihood is good with a χ^2 of 18.5 and 23.1 for 24 bins for the K^+K^- mode and $K^\pm K^0_s$ mode, respectively. The results are consistent with each other and with the Standard Model value for A_s. Systematic uncertainties of different size are associated with the K^+K^- mode and the $K^\pm K^0_s$ mode. The systematic uncertainties are presented in the next Chapter.

Chapter 8

Systematic Uncertainties

The understanding of the parameters used as inputs to the fitting function and of their uncertainties is very important to this analysis. We expect the dominant contributions to the systematic uncertainty to come from the light flavor sector, and they are discussed first. The heavy flavor modelling leads to a relatively small uncertainty, due to the large number of experimental constraints on the relevant input parameters. Next, we discuss uncertainties associated with the polarization of the electron beam, hard gluon radiation, A_e, the corrections to the simulated n_{sig} distribution and the simulated K_s^0 (and $\Lambda^0/\bar{\Lambda}^0$) momentum spectra, and investigate the effect of a $|\cos\theta_s|$ dependence of a_s. The uncertainties resulting from the statistics of the simulated sample are investigated, and the systematic uncertainties are summarized.

8.1 Light Flavor Systematics

For the light flavors, there are few experimental constraints on the relevant input parameters to the fitting function (Equation (7.1)), i.e. ϵ_u, ϵ_d, ϵ_s, R_u, R_d, R_s, a_u, a_d, a_s, and A_u, A_d. The corresponding systematic uncertainties are therefore ill defined and potentially large. We used the JETSET fragmentation model to develop the analysis; it is important to establish a sufficient level of confidence in this model to evaluate the systematic uncertainties.

Qualitative features such as leading particle production [8], short range rapidity correlations between high-momentum KK and baryon-antibaryon pairs [98] and long-range correlations between

several particle species [98] have been observed experimentally, verifying the analysis method. However, these results are not sufficient to quantify the analyzing power of the strange particle tag or the $u\bar{u}$ and $d\bar{d}$ background. Our Monte Carlo simulation provides a reasonable description [8; 98] of the above observations, but relies on a number of assumptions to relate them to our input parameters. We have chosen to use our data as much as possible to constrain the least certain light flavor input parameters in the context of our Monte Carlo model. The total number of selected light flavor events is obtained from the data sample by subtracting the simulated heavy flavor contribution, which is reliable within well-defined uncertainties (see Section 8.2).

In Section 8.1.1, we describe the measurement of the sources of tags signed with incorrect strangeness in $s\bar{s}$ events from which we constrain a_s. The combined $u\bar{u} + d\bar{d}$ background, N_{ud}, is constrained by using data as described in Section 8.1.2. We also attempt to use data to constrain the combined analyzing power of $u\bar{u} + d\bar{d}$ events, a_{ud}. This approach minimizes the model dependence by measuring large systematic effects in the data, though it relies on the simulation for some details.

8.1.1 Analyzing Power in $s\bar{s}$ Events

The analyzing power in selected $s\bar{s}$ events can be diluted by two different mechanisms, as shown in Figure 8.1. In order to tag an s jet as an $\bar{s}$ jet, the jet must either contain a true K^+ or $\bar{\Lambda}^0$ that satisfies the selection cuts, or a π^+ or p that is mis-identified as K^+, or a fake $\bar{\Lambda}^0$. This observation along with the high $s\bar{s}$ purity of the tagged sample enables us to constrain the $s\bar{s}$ analyzing power from the data.

First we discuss the effect of particle mis-identification. For $s\bar{s}$ events, Table 8.1 lists the simulated fractions of K^+K^- and $K^\pm K^0_s$ tags consisting of two correctly identified particles (labeled

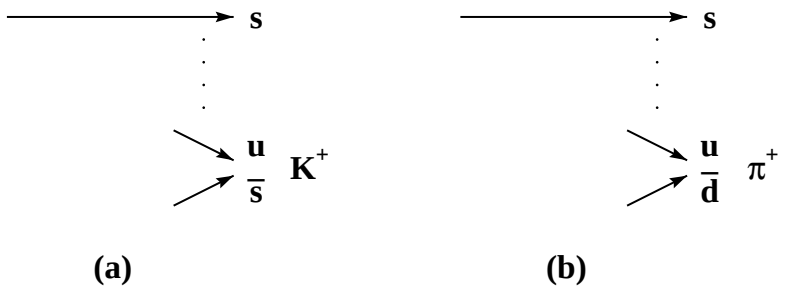

Figure 8.1: The analyzing power in $s\bar{s}$ events can be diluted by (a) an additional strange fragmentation particle, or (b) a mis-identified particle.

f_{cc}), one correctly identified and one mis-identified particle (f_{cm}), and two mis-identified particles (f_{mm}). A large fraction of the tags in $s\bar{s}$ events has both particles correctly identified, in particular in the case for K^+K^-. The simulated fraction of tags with two mis-identified particles is very small. The corresponding fractions of $s\bar{s}$ events having incorrectly signed strangeness, $g_{cc,cm,mm(w)} = N_s^w/(N_s^r + N_s^w) = (1 - a_s)/2$, are included in Table 8.1.

Table 8.1: Effect of particle mis-identification in $s\bar{s}$ events.

Mode	f_{cc}	$g_{cc(w)}$	f_{cm}	$g_{cm(w)}$	f_{mm}	$g_{mm(w)}$
K^+K^-	95.3%	0.022	4.6%	0.082	0.1%	0.5
$K^\pm K_s^0$	90.8%	0.138	9.0%	0.255	0.2%	0.5

For the purpose of evaluating the effect of particle mis-identification, we distinguish between two contributions, the uncertainty in $\pi^\pm$ and $p/\bar{p}$ production and the uncertainty in the mis-identification of $\pi^\pm$ and $p/\bar{p}$ as $K^\pm$, and the identification of a fake K_s^0. We rely on the simulation to predict the amount of $\pi^\pm$ and $p/\bar{p}$ production with $p > 9$ GeV/c in $s\bar{s}$ events. It is unclear how to evaluate a systematic uncertainty on this, so we apply a conservative estimate of this effect on the wrong sign fraction in $s\bar{s}$ events by varying it by $\pm 100\%$, as given in Table 8.2.

8. SYSTEMATIC UNCERTAINTIES

The rate of mis-identifying $\pi^{\pm}$ and $p/\bar{p}$ as $K^{\pm}$ has been measured in our data with a relative 25% uncertainty [6; 9]. The rate of fake K_s^0 is estimated from the sidebands of the corresponding invariant mass distributions (see Figure 6.11) with better precision. However, we also applied the conservative 25% to K_s^0 as in the case of the $K^{\pm}$. The corresponding uncertainty on the wrong sign fractions due to the particle mis-identification rates is summarized in Table 8.2.

Table 8.2: Summary of uncertainties on the fraction of $s\bar{s}$ events having incorrectly signed strangeness. The last column shows the systematic uncertainty on A_s.

Mode	$\pm 100\%$ $\pi^{\pm}$, $p/\bar{p}$ prod.	$\pm 25\%$ mis-ID	calibrated 3-kaon rate	$\delta A_s / A_s$
K^+K^-	13.9%	3.5%	18.5%	1.3%
$K^{\pm}K_s^0$	7.4%	1.8%	18.5%	8.6%

In the following, we investigate the second mechanism to dilute the analyzing power for selected $s\bar{s}$ events. If a non-leading high-momentum K^+ is produced in an s jet, then there must be an associated particle with strangeness -1 in the jet, which will also tend to have high momentum. Including the leading particle of negative strangeness, such a jet will contain one particle of positive strangeness and two particles of negative strangeness, all with relatively high momentum. We need to quantify how often this process happens. A conventional strangeness suppression factor, γ_s, parametrizes the probability of $s\bar{s}$ popping from the vacuum relative to $u\bar{u}$ and $d\bar{d}$. Measurements of γ_s [7; 9] have been performed in the context of the JETSET model at high momentum, assuming independence from event flavor and momentum, but these measurements are rather imprecise. We can avoid this model dependence by investigating the rate of production of these wrong-sign kaons in our data, i.e. we study events in which we find three identified $K^{\pm}$ and/or K_s^0 passing our selection cuts in the same hemisphere. Such an event sample is expected to be fairly pure in $s/\bar{s}$, since a $u/\bar{u}$ or $d/\bar{d}$ jet would have to contain either four strange particles or two strange particles

and one mis-identified particle in order to be selected.

We find 61 hemispheres in our data containing three identified $K^{\pm}$ and/or K^0_s. Our simulation predicts 67.2, including 9.3 $c\bar{c}+b\bar{b}$ and 15.3 $u\bar{u}+d\bar{d}$ hemispheres, which is consistent. We assume that the heavy flavor background is well simulated, and use the absolute prediction of the simulation. For the purpose of quantifying the consistency of data and the simulation, we subtract the predicted $c\bar{c}+b\bar{b}$ background from the data, and scale the number of remaining light flavor hemispheres by the simulated ratio $N_s/(N_u+N_d+N_s)$, which is rather insensitive to γ_s. We obtain a measured number of 38.2 ± 6.5 strange jets with 3 kaons. The Monte Carlo prediction of 42.6 ± 3.2 jets is consistent with the data, and the simulated a_s for each mode is used as our central value for the analyzing power in $s\bar{s}$ events. The statistical uncertainty on the data/MC ratio of 0.90 ± 0.17 provides a 18.5% constraint on the number of $s\bar{s}$ events that could have the wrong sign.

This constraint is not entirely model-independent, since we rely on the model to predict the fraction of these jets in which all three kaons pass the momentum cuts, as well as the fraction in which the wrong-sign kaon is chosen as the tagging particle rather than either of the right-sign kaons. We assume γ_s to be roughly the same for $u\bar{u}$, $d\bar{d}$ and $s\bar{s}$ events in the momentum range under consideration. We also assume equal production of charged versus neutral kaons, as in the simulation. We take these assumptions to be valid to a precision greater than the statistical uncertainty on the constraint, and therefore do not assign any additional systematic uncertainties. Thus, this procedure delivers a simultaneous calibration of the analyzing power in $s\bar{s}$ events for the K^+K^- and $K^{\pm}K^0_s$ modes.

In principle, particle mis-identification affects the calibration procedure. However, the simulation predicts that only 5% of 3-kaon $s\bar{s}$ hemispheres contain at least one mis-identified particle, compared to 18% in $u\bar{u}+d\bar{d}$ and 11% in $c\bar{c}+b\bar{b}$ hemispheres; we neglect the resulting small effect.

We applied the 18.5% uncertainty to the wrong-sign fraction, $N_s^w/(N_s^r + N_s^w)$, of the K^+K^- and $K^\pm K_s^0$ modes. As a cross check on the 3-kaon calibration, we have also counted hemispheres containing a K^+K^+ or K^-K^- pair, obtaining a consistent but less precise constraint.

For each tagging mode, we add the uncertainties on A_s arising from mis-identification and the 3-kaon calibration in quadrature, as shown in Table 8.2. These systematic uncertainties on A_s are low for the K^+K^- mode due to the very high a_s given by the double tag procedure and substantial for the $K^\pm K_s^0$ mode.

8.1.2 Light Flavor Background and Analyzing Power

The background from $u\bar{u} + d\bar{d}$ events must be understood in terms of both magnitude and slope. In the fit we constrain $N_{ud} + N_s$. A constraint on the remaining parameter, the relative $u\bar{u} + d\bar{d}$ background level, N_{ud}/N_s, can be derived in a way similar to the calibration of the analyzing power in $s\bar{s}$ events.

We make use of the fact that an even number of particles with positive and negative strangeness must be produced in a $u/\bar{u}$ jet or $d/\bar{d}$ jet. The study of short range correlations between KK pairs [98] shows that they appear in strange-antistrange pairs that have similar momenta. Therefore hemispheres containing K^+K^- or $K^\pm K_s^0$ pairs are an experimental sign of the $u\bar{u} + d\bar{d}$ background. However, $s\bar{s}$ hemispheres with three strange particles in which one was not identified contribute to this sample. Another approach is based on long range correlations between kaons of the same charge in both hemispheres [98]. The $u\bar{u} + d\bar{d}$ background is expected to have approximately equal rates of same charge, $K^\pm K^\pm$, and opposite charge, K^+K^- tagged events. The contribution of $s\bar{s}$ events to the same charge, $K^\pm K^\pm$, tagged sample is substantial.

Again, we distinguish between two ways for a $u/\bar{u}$ or $d/\bar{d}$ jet to be tagged; there must either be a real $K^\pm$ or K_s^0 passing the selection cuts or a mis-identified $\pi^\pm$ or $p/\bar{p}$, or fake K_s^0. First

we address the effect of particle mis-identification. For the combined $u\bar{u}$ and $d\bar{d}$ events, and in the notation used in the previous Section, Table 8.3 lists the fractions of simulated $u\bar{u}+d\bar{d}$ events tagged as signal in the K^+K^- and $K^\pm K_s^0$ modes, consisting of two correctly identified particles, one correctly identified and one mis-identified particle, and two mis-identified particles.

The fraction of tags with at least one mis-identified particle is larger in $u\bar{u}$ and $d\bar{d}$ events than in $s\bar{s}$ events, since leading particles in $u/\bar{u}$ and $d/\bar{d}$ jets are dominated by $\pi^\pm$, whereas $K^\pm$ and K_s^0 are strangeness suppressed.

Table 8.3: Effect of particle mis-identification in $u\bar{u}+d\bar{d}$ events.

Mode	f_{cc}	f_{cm}	f_{mm}
K^+K^-	69.9%	28.1%	2%
$K^\pm K_s^0$	75.2%	23.2%	1.6%

Again we consider two categories, the production of $\pi^\pm$ and $p/\bar{p}$ (fake K_s^0) rather than $K^\pm$ (K_s^0) and mis-identification rates of non-$K^\pm$ as $K^\pm$ (reconstruction of fake K_s^0). We use the simulation to predict the amount of non-$K^\pm$ (fake K_s^0) production above the momentum cut in $u\bar{u}$ and $d\bar{d}$ events. Since the evaluation of the corresponding systematic uncertainty is unclear, we apply a conservative estimate of this effect by varying the probability that a leading non-K is produced up to 1, and down by the same amount of 15%. The corresponding uncertainty on the $u\bar{u}+d\bar{d}$ fraction, N_{ud}, is summarized in Table 8.4. We also apply the same 25% uncertainty on the rate of $\pi^\pm$, $p/\bar{p}$, and K_s^0 mis-identification. This uncertainty on N_{ud} is also given in Table 8.4.

Next we discuss the calibration of the magnitude of the light flavor background by comparing the rates of K^+K^- or $K^\pm K_s^0$ pairs in data and the simulation. We count 1262 hemispheres in the data containing an identified K^+K^- pair and 983 hemispheres with an identified $K^\pm K_s^0$ pair. The respective Monte Carlo predictions of 1217.8, including 126.9 $c\bar{c}+b\bar{b}$ and 703.9 $s\bar{s}$ hemispheres, and

Table 8.4: Summary of uncertainties on the $u\bar{u} + d\bar{d}$ fraction.

Mode	±15% $\pi^{\pm}$, $p/\bar{p}$ prod.	±25% mis-ID	calibrated 2-kaon rate
K^+K^-	4.8%	8.0%	4.6%
$K^{\pm}K^0_s$	4.0%	6.6%	4.6%

1001.5, including 148.6 $c\bar{c}+b\bar{b}$ and 433.3 $s\bar{s}$ hemispheres, are consistent. Again we assume the heavy flavor background to be well simulated. After subtracting the predicted $c\bar{c} + b\bar{b}$ jet backgrounds, we scale the number of $u\bar{u} + d\bar{d}$ hemispheres by the simulated ratio $(N_u + N_d)/(N_u + N_d + N_s)$. In the data, we obtain 402.7 ± 15.6 $u\bar{u} + d\bar{d}$ jets with a K^+K^- pair, and 410.5 ± 18.2 $u\bar{u} + d\bar{d}$ jets with a $K^{\pm}K^0_s$ pair. The Monte Carlo predictions of 387.0 ± 9.7 and 419.7 ± 10.1 $u\bar{u} + d\bar{d}$ jets are consistent, and we use the simulated central values for N_u and N_d for the K^+K^- mode and the $K^{\pm}K^0_s$ mode. The statistical uncertainty on the corresponding data/MC ratios of 1.04 ± 0.05 for K^+K^- pairs and 0.98 ± 0.05 for $K^{\pm}K^0_s$ pairs provide 4.6% and 5.1% constraints on the $u\bar{u} + d\bar{d}$ background. We also count 503 same charge $K^{\pm}K^{\pm}$ tagged events in the data, compared to 558.7 in the simulation (a difference of two standard deviations) including 96.5 $c\bar{c} + b\bar{b}$ and 316.9 $s\bar{s}$ tags. The corresponding data/MC ratio of 0.88 ± 0.07 yields a 8.1% constraint on the $u\bar{u} + d\bar{d}$ background.

As for the a_s calibration, these constraints are not completely model-independent. However the three quantities are sensitive in different ways to N_{ud}, providing valuable complementarity. Rather than combining the constraints, we simply use the most precise constraint, a 4.6% variation on the $u\bar{u} + d\bar{d}$ background in the K^+K^- mode and $K^{\pm}K^0_s$ mode, and consider the other constraints as cross checks.

In addition, this calibration procedure is affected, in principle, by particle mis-identification.

8. SYSTEMATIC UNCERTAINTIES

The simulation predicts that 7% of all $u\bar{u}+d\bar{d}$ hemispheres with a K^+K^- pair contain at least one mis-identified particle, compared to 8% in $s\bar{s}$ hemispheres; the corresponding numbers for $K^\pm K^0_s$ pairs are 13% of all $u\bar{u}+d\bar{d}$ hemispheres, and 13% of all $s\bar{s}$ hemispheres. We neglect any additional uncertainties. The uncertainties on A_s arising from mis-identification and the 2-kaon calibration are added in quadrature for each tagging mode, as summarized in Table 8.5.

Table 8.5: Systematic uncertainties on A_s resulting from the light flavor background and analyzing power.

Source	$\delta A_s/A_s$ K^+K^-	$\delta A_s/A_s$ $K^\pm K^0_s$
N_{ud}/N_s	2.8%	3.9%
a_{ud}	4.7%	7.0%
A_{ud}	–	–
Total:	5.5%	8.1%

The above checks are also sensitive to the analyzing power of $u\bar{u}+d\bar{d}$ events, a_{ud}. However, with our event statistics we cannot obtain a meaningful constraint on this quantity. We therefore assume that a_{ud} must be negative, since u and d jets must produce a leading K^+ rather than K^-, and that the modulus of a_{ud} must be less than that of a_s, since there is always a companion particle of opposite strangeness in a u or d jet that will tend to dilute the analyzing power. We take these as hard limits, $-a_s < a_{ud} < 0$, and use the middle of the range for our central value. Assuming equal probability across this range, we assign an uncertainty equal to the range divided by $\sqrt{12}$, which is conservative since our expectation and the simulated prediction are well away from both limits. There are no precise measurements of A_u or A_d. We set A_u and A_d to their Standard Model values and assume that any deviation is smaller than the uncertainty on a_{ud}, and assign no additional systematic variation. The large systematic uncertainties associated with a_{ud} are summarized in Table 8.5.

8.2 Heavy Flavor Modelling

The characteristics of heavy flavor events relevant to this analysis have been measured in many experiments, and our simulation [46; 73; 78] has been tuned [75] to reproduce these results. In particular, the parameters R_c, R_b, A_c and A_b are measured [1] by SLD and others to good accuracy. Therefore, we evaluate the effect of their uncertainties by varying those parameters by the uncertainties on their world average values [1], as given in given Table 8.6.

Table 8.6: World average values [1] of A_c, A_b, R_c and R_b.

Parameter	Systematic variation
A_c	0.657 ± 0.031
A_b	0.890 ± 0.021
R_c	0.1731 ± 0.0044
R_b	0.21732 ± 0.00087

The resulting systematic uncertainties are summarized in Table 8.7. The systematic contribution on A_s from the uncertainties on A_b and R_b is negligible due to the very small $b\bar{b}$ background in the tagged sample and the experimental precision on A_b and R_b. The uncertainty from R_c delivers a small contribution due to the experimental precision on this quantity and the slope of the $c\bar{c}$ background in the tagged sample being similar to the signal. The total systematic contribution of all four parameters is dominated by A_c.

The B (D) hadron fragmentation [19] is understood from measurements of several quantities such as the fraction of the different B (D) hadron species, the mean decay multiplicity, the branching ratio of the b (c) quark to K, and the parameters in the B (D) hadron fragmentation function. To estimate the systematic effects of these measurements we use the approach described below.

First, we note that the $b\bar{b}$ background is heavily suppressed mostly due to the light flavor

Table 8.7: Systematic uncertainties resulting from the heavy flavor sector.

Parameter/ Source	$\delta A_s/A_s$ K^+K^-	$\delta A_s/A_s$ $K^\pm K^0_s$
A_c	0.6%	0.8%
A_b	$< 0.1\%$	$< 0.1\%$
R_c	$< 0.1\%$	0.1%
R_b	$< 0.1\%$	$< 0.1\%$
a_c	0.3%	2.6%
a_b	$< 0.1\%$	0.4%
ϵ_c	0.1%	0.5%
ϵ_b	$< 0.1\%$	$< 0.1\%$
Total:	0.7%	2.8%

tag, so the associated systematic uncertainty is small. In the case of the $c\bar{c}$ background in the tagged sample, the systematic uncertainties resulting from relevant properties of the D hadron fragmentation [19] can be evaluated first by varying each quantity in turn by plus and minus the error on its world average value. This is followed by a procedure which assigns weights to the simulated events to approximate a distribution generated with the parameter value in question. The Monte Carlo predictions for the $c\bar{c}$ fraction and the analyzing power are rederived, a new fit is performed, and the difference between the A_s value extracted and the central value is taken as a systematic uncertainty. This procedure has been performed in many SLD analyses (e.g. [99; 100; 113]), which gives confidence in our simplified approach which we discuss next.

There are two parts to the simulation of ϵ_c and ϵ_b, the efficiency to pass the light flavor tag and that to give an identified $K^\pm$ or K^0_s on the relevant hemispheres. For the light flavor tag, the uncertainties in the rates of tagging $c\bar{c}$ and $b\bar{b}$ events as light flavors in a rather similar way were studied in detail in Ref. [102], and conservative absolute uncertainties of 0.01 on all efficiencies were assigned. Since then there have been numerous improvements in the uncertainties on the input

parameters to the modelling of heavy flavors and in the quality of our detector simulation. However we keep the conservative 0.01 absolute uncertainty, which corresponds to relative uncertainties of 1.7% on ϵ_c and 8.9% on ϵ_b.

For the tagged event sample, the effectiveness of the $K^{\pm}$ to tag D and B meson decays inclusively has also been studied at the SLD to measure A_c [99] and A_b [100]. In both analyses, the rate of selecting events in the data with a tagged K^+ in one hemisphere and a K^- in the other is reproduced by the simulation within less than 10%. Our $K^{\pm}$ selection cuts in the A_s analysis are different, and we simply apply a conservative 15% relative uncertainty on ϵ_c and ϵ_b. The uncertainties on ϵ_c and ϵ_b, lead to uncertainties in $\delta A_s/A_s$, which we sum in quadrature, as listed in Table 8.7.

In the A_c and A_b analyses, the analyzing powers of the $K^{\pm}$ tags were calibrated from the data, and were found to be consistent with the simulation. The correct sign fraction of 0.293 ± 0.014 for the single $K^{\pm}$ tag in the A_b analysis corresponds to a wrong sign fraction of $f_w = N_w/(N_r + N_w) = 0.147 \pm 0.017$ for a corresponding double tag which has a tagged K^+ in one hemisphere and a K^- in the other. The tagged sample in the A_b analysis is very pure in true $K^{\pm}$ from B hadron decays. Our A_s sample is also very pure, but we use different $K^{\pm}$ selection criteria, in particular we apply a momentum cut of $p > 9$ GeV/c to the $K^{\pm}$. The simulation predicts that the wrong sign fractions for our K^+K^- mode and $K^{\pm}K^0_s$ mode are 20% lower than in the A_b analysis, for the single and double $K^{\pm}$ tag, respectively.

We simply take the larger 20% shift, rather than the measured uncertainty on the calibrated wrong sign fraction in the A_b sample, and apply it as the systematic variation on the wrong sign fraction of our $b\bar{b}$ events in the A_s sample. This approach yields relative uncertainties on a_b of 6.2% for the K^+K^- mode and 18.6% for the $K^{\pm}K^0_s$ mode.

The A_c analysis also includes a calibration of the analyzing power for K^+K^- double tagged

events, which is found to be consistent with the simulation. The A_c sample is also dominated by true $K^{\pm}$ emerging from D hadron decays. However, our simulated sample has substantially larger wrong sign fraction due to contributions from mis-identified $\pi^{\pm}$ and fragmentation products. We vary both of these contributions by 25% and take the sum of the effects on the wrong sign fractions in quadrature. This yields a 20% variation on the wrong sign fraction of our tagged $c\bar{c}$ events, corresponding to relative uncertainties on a_c of 2.3% for the K^+K^- mode and 14.7% for the $K^{\pm}K_s^0$ mode. The effect on A_s is shown in Table 8.7. We sum the uncertainties on A_s in quadrature for a total systematic uncertainty arising from the heavy flavor sector, which is a relatively small contribution compared to the systematic effect of the light flavor sector.

8.3 Uncertainties on other Quantities

Electron Beam Polarization

The average luminosity-weighted polarizations [49] of the electron beam and their uncertainties for the different run periods are summarized in Table 3.1. The resulting systematic uncertainty is $\delta A_s/A_s = 1.0\%$ for the K^+K^- mode and the $K^{\pm}K_s^0$ mode.

Hard Gluon Radiation

Final state gluon radiation, i.e. the emission of gluons from the primary quark and anti-quark, smears the primary s quark direction. The QCD correction, δ, is incorporated in the likelihood function (Equation (7.1)) to correct for this effect. Theoretical calculations of QCD corrections [110] for massive and massless quarks have been performed, and good reviews [111; 112] are available. In general, these calculations determine corrections to the initial quark direction. At the experimental level, however, we use the signed thrust axis to approximate the primary quark

direction.

This is advantageous in the sense that the use of the thrust axis reduces the effect of hard gluon radiation by selecting in most cases the s or $\bar{s}$ direction, whichever is least changed in a given event. The analysis flow makes use of high-momentum strange particles to tag both event hemispheres. Thus, the sensitivity to the QCD correction is further decreased since events without hard gluon radiation are tagged preferentially. As a consequence, the theoretical correction for hard gluon radiation is diminished by a bias factor which has been studied in detail at the SLD (see e.g. [99; 100; 112; 113]). The correction due to hard gluon radiation for the strangeness tag in both event hemispheres has been studied, resulting in an effective correction of $\delta = -0.013$. Since higher order QCD corrections affect this estimate, we follow the SLD convention and apply a conservative uncertainty of 0.006 to δ, which results in a relatively small systematic uncertainty of $\delta A_s/A_s = 0.6\%$ for the K^+K^- mode and the $K^\pm K^0_s$ mode.

Lepton Coupling A_e

Unlike $\tilde{A}^f_{FB}$ in Equation (2.26), the likelihood fit to the polar angle distributions reintroduces the well measured parameter A_e. However, the fit is insensitive to the value of A_e. We use $A_e = 0.1499 \pm 0.0021$ [1] which results in a negligible systematic uncertainty on A_s.

8.4 Further Systematic Checks

Correction to the Simulated n_{sig} Distribution

To obtain the n_{sig} distribution (see Figure 5.6), we first increased n_{sig} by 1 with a probability independent of event flavor. In addition, we removed the small remaining difference in normalization between data and the simulation in the $n_{sig} = 1$ bin by randomly removing simulated

events from that bin. Since we use the heavy flavor as an absolute prediction, we investigate the change in tagging efficiencies ϵ_c and ϵ_b caused by these corrections. We find that both corrections combined lead to changes of 2.8% and 3.3% for ϵ_c and ϵ_b, respectively. The resulting effect on A_s is negligible.

Corrections to the Simulated K_s^0 and $\Lambda^0/\bar{\Lambda}^0$ Momentum Distributions

We corrected the simulated $\Lambda^0/\bar{\Lambda}^0$ and K_s^0 momentum distributions (see Figure 6.9 and Figure 6.12) to improve the agreement between the data and the simulation for the single tag rates. We repeated the analysis with no such corrections. The resulting changes in the $s\bar{s}$ purity and the analyzing power in $s\bar{s}$ events are small, and we considered the systematic effect to be negligible.

Analyzing Power in $s\bar{s}$ Events as a Function of $\cos\theta_s$

Apart from small effects related to particle mis-identification, there is no physical reason why the analyzing power in $s\bar{s}$ events, a_s, should depend on $\cos\theta_s$. However, we used the simulation to investigate a dependence. Using the K^+K^- mode as an example, Figure 8.2 shows a_s as a function of $|\cos\theta_s|$. A straight line fit yields a slope of $m = 0.021 \pm 0.026$, which is consistent with zero. We obtain $\delta A_s/A_s = 0.3\%$ from a fit with this slope and the nominal value of a_s at $|\cos\theta_s| = 0.71/2$. Compared to the size of the other uncertainties, this effect is small and we do not include it as a systematic uncertainty.

8.5 Monte Carlo Statistics

The statistical uncertainties on the input quantities to the fitting function (Equation (7.1)) lead to systematic uncertainties. We consider the analyzing powers a_u, a_d, a_s, a_c, and a_b. Since we set $a_{ud} = -a_s/2$, we propagate the statistical uncertainty on a_s for a_{ud}. The systematic uncertainties

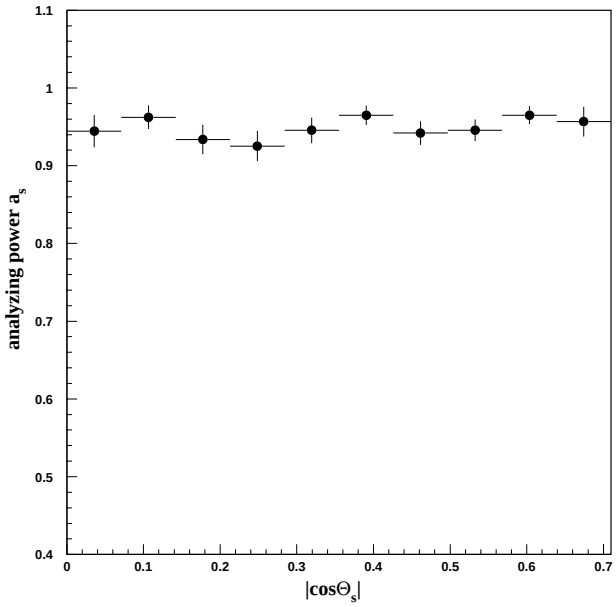

Figure 8.2: Analyzing power a_s as a function of $|cos\theta_s|$ for the K^+K^- mode.

on A_s arising from a_{ud}, a_s, a_c, a_b are added in quadrature, as listed in Table 8.8. For the variation of the statistical uncertainties on the flavor fractions, N_u, N_d, N_s, N_c, and N_b, we make an absolute prediction of the $c\bar{c}$ and $b\bar{b}$ backgrounds, and scale the remaining light flavor portion accordingly. The resulting systematic uncertainties on A_s are added in quadrature and are summarized in Table 8.8.

Table 8.8: Summary of systematic uncertainties from Monte Carlo statistics.

Source	$\delta A_s/A_s$ K^+K^-	$\delta A_s/A_s$ $K^\pm K^0_s$
analyzing powers a_f	0.6%	1.7%
flavor fractions N_f	0.9%	1.1%
Total:	1.1%	2.0%

8.6 Summary of Systematic Uncertainties

The systematic uncertainties associated with the A_s measurement are summarized in Table 8.9. The light flavor sector dominates the total systematic uncertainty. In particular, a_{ud} contributes the leading systematic uncertainty for the K^+K^- mode, and the systematic effects of a_s deliver the largest systematic uncertainty for the $K^\pm K^0_s$ mode. Uncertainties in the heavy flavors, the hard gluon radiation, and the electron beam polarization result in relatively small systematic contributions.

The individual systematic uncertainties are added in quadrature to yield a total systematic uncertainty of $\delta A_s/A_s = 5.9\%$ on the K^+K^- mode and $\delta A_s/A_s = 12.3\%$ on the $K^\pm K^0_s$ mode. The K^+K^- mode has a lower systematic uncertainty than the $K^\pm K^0_s$ mode due to its high analyzing power in $s\bar{s}$ events and low $u\bar{u} + d\bar{d}$ background.

Table 8.9: Summary of systematic uncertainties for the A_s measurement.

Source	Comments	Syst. variation	$\delta A_s/A_s$ K^+K^-	$\delta A_s/A_s$ $K^\pm K^0_s$
heavy flavor sector	MC/ world averages	Ref. [1; 73; 75]	0.7%	2.8%
hard gluon radiation	Stav-Olsen with bias correction	$(1.3 \pm 0.6)\%$	0.6%	0.6%
P_e	data	Table 3.1	1.0%	1.0%
a_s	calibration	Table 8.2	1.3%	8.6%
a_{ud}	$a_{ud} = -a_s/2$	Table 8.5	4.7%	7.0%
A_{ud}	Standard Model	–	–	–
N_{ud}/N_s	calibration	Table 8.4	2.8%	3.9%
MC statistics		Table 8.8	1.1%	2.0%
Total:			5.9%	12.3%

Thus we measure for the K^+K^- mode:

$$A_s = 0.858 \pm 0.079(stat.) \pm 0.050(syst.) \tag{8.1}$$

and for the $K^{\pm}K^0_s$ mode:

$$A_s = 0.964 \pm 0.120(stat.) \pm 0.119(syst.). \tag{8.2}$$

The total uncertainty on the K^+K^- mode is 10.9%, compared to 17.5% for the $K^{\pm}K^0_s$ mode. The two results are consistent. The major systematic uncertainties are completely positively correlated between the two modes so the uncertainties cannot be simply combined in the usual manner.

Chapter 9

Summary of Results

9.1 Analysis Result

This dissertation has presented a direct measurement of the parity-violating coupling of the Z^0 to strange quarks, A_s, derived from e^+e^- collision data containing approximately 550,000 hadronic decays of polarized Z^0 bosons. The average electron beam polarization was 73% and 74% during the 1993-5 and 1996-8 run periods, respectively. The particle identification capability of the Cherenkov Ring Imaging Detector is crucial to the analysis. Polarized $Z^0 \to s\bar{s}$ events are tagged by the presence in each event hemisphere of a high-momentum $K^{\pm}$, K^0_s or $\Lambda^0/\bar{\Lambda}^0$ identified using particle identification and/or a mass tag. The background from heavy flavor events is suppressed by precision measurements with the CCD-based vertex detector. The signed event thrust axis is used to approximate the direction of the initial s quark. The coupling A_s is derived from a maximum likelihood fit to the polar angle distributions of the tagged s quark measured with left- and right-handed electron beams. To reduce the model dependence of the measurement, the background from $u\bar{u}$ and $d\bar{d}$ events and the analyzing power of the method for $s\bar{s}$ events are constrained from the data. We obtain for the K^+K^- mode:

$$A_s = 0.86 \pm 0.08(stat.) \pm 0.05(syst.) \tag{9.1}$$

and for the $K^{\pm}K^0_s$ mode:

$$A_s = 0.96 \pm 0.12(stat.) \pm 0.12(syst.). \tag{9.2}$$

The two results are consistent. They are consistent with the Standard Model prediction of $A_s = 0.94$ (using $\sin^2\theta_W = 0.23$) and current averages for the bottom quark coupling from SLD, $A_b = 0.898 \pm 0.029$ [2], and from LEP, $A_b = 0.887 \pm 0.021$ [2]. For the purpose of the following discussion, we keep the corresponding result of the K^+K^- mode as our central measured value for A_s since it has the smaller total uncertainty. Our measurement provides a test of universality in the down-type quark sector with 11% precision. In order to shed more light on the possible difference between the measured value for A_b and the prediction of the Standard Model, substantially more data would be needed.

9.1.1 Comparison with other Experiments

Previously, measurements of the strange quark coupling have been performed by the DELPHI [3; 114] and OPAL [4] collaborations at LEP. These measurements differ significantly in their analysis methods and the way model dependencies are taken into account. In particular, since they do not have a polarized electron beam they measure the forward-backward asymmetries, A^s_{FB} and $A^{d,s}_{FB}$. To convert this into a value for the strange quark coupling, A_s, requires also the electron coupling, A_e, as described in Chapter 2.

The first study of the strange quark coupling was performed by the DELPHI collaboration [3]. They have measured the polar angle production asymmetries of $K^{\pm}$ in the momentum range $10 < p < 18$ GeV/c and $\Lambda^0/\bar{\Lambda}^0$ in the momentum range $11.41 < p < 22.82$ GeV/c, with a combined $s\bar{s}$ purity of 43%, to obtain $A^s_{FB} = 0.131 \pm 0.035(stat.) \pm 0.013(syst.)$. They have also used neutral hadronic calorimeter clusters with $E > 15$ GeV, created by neutrons and neutral

kaons. Assuming $d-s$ universality, they obtain $A_{FB}^{d,s} = 0.112 \pm 0.031(stat.) \pm 0.054(syst.)$ from a tagged sample of combined 69% $s\bar{s} + d\bar{d}$ purity.

The experimental technique chosen by DELPHI selects only the particle with the highest momentum to tag an $s\bar{s}$ event candidate (single tag). This method entails a considerable statistical advantage compared to our measurement, but at the expense of lower $s\bar{s}$ purity and large background contributions from $u\bar{u}$ and $d\bar{d}$ events. More recently, an updated DELPHI result [114] using only $K^{\pm}$ has been contributed to ICHEP 1998, making use of their full event sample. The $s\bar{s}$ purity is estimated to be 55% and 43% for the sample tagged in the barrel and endcap portions of the detector, respectively. The combined result is $A_{FB}^{s} = 0.108 \pm 0.015(stat.) \pm 0.007(syst.)$. However, no attempt is made to calibrate simulated light flavor fractions and analyzing powers from the data, and the extraction of the strange quark coupling from the measured production asymmetries is model dependent.

The OPAL collaboration has pursued a different and more comprehensive approach. They have used identified $\pi^{\pm}$, $K^{\pm}$, $p/\bar{p}$, K_s^0 and $\Lambda^0/\bar{\Lambda}^0$ with $x_p = 2p/E_{cm} \geq 0.5$, where E_{cm} denotes the center-of-mass energy in the event, to tag rather pure samples of light flavors and attempt to measure R_u, R_d, R_s, and A_u, A_d, A_s separately. They have determined most of the background contributions and analyzing powers from double-tagged events in the data by making use of broad assumptions on the fragmentation process. This method eliminates most of the model dependence, but results in limited statistical precision. In particular, they assume $d-s$ universality to obtain $A_{FB}^{d,s} = 0.068 \pm 0.035(stat.) \pm 0.011(syst.)$ from their entire data sample.

Using $A_e = 0.1499 \pm 0.0021$ [1], the published DELPHI measurements translate into $A_s = 1.165 \pm 0.311(stat.) \pm 0.116(syst.)$ and $A_{d,s} = 0.996 \pm 0.276(stat.) \pm 0.480(syst.)$, where we have neglected the small uncertainty on A_e. Their unpublished ICHEP98 result corresponds to $A_s = 0.961 \pm 0.133(stat.) \pm 0.062(syst.)$. Similarly, the OPAL measurement yields $A_{d,s} = 0.605 \pm$

$0.311(stat.) \pm 0.098(syst.)$. Our measurement is consistent with these and represents a substantial improvement in precision.

Figure 9.1 summarizes the status of world A_s and $A_{d,s}$ measurements. Our result and the A_s measurement from DELPHI can be combined for a world average value of $A_s = 0.89 \pm 0.08$, determined from the weighted mean using the total uncertainty for each, assuming all uncertainties to be independent from each other. Thus $b - s$ universality (see Table 2.5) is tested to 9%, but measurements of A_d rather than $A_{d,s}$ would be desirable to fully probe universality in the down-type quark sector.

9.2 Conclusion and Outlook

We have performed a direct measurement of the parity-violating coupling of the Z^0 to strange quarks, A_s, and found consistency with the Standard Model and previous A_b measurements. The measurement supports the predicted universality of the Z^0 to down-type quark couplings.

The SLD experiment will not take more data in the future, since the proposal for a new SLD run was not granted despite a very successful 1997-8 run and a strong physics case for more data. The technique for tagging strange events is now well established, and improvements with more data would benefit not only the A_s measurement, but would also open an experimental window to the light quark coupling parameters A_d and A_u. In the distant future one may contemplate measurements of coupling parameters at the Z^0 pole at the proposed 500-1000 GeV linear collider which may need to spend some period of time at this lower energy for calibration purposes.

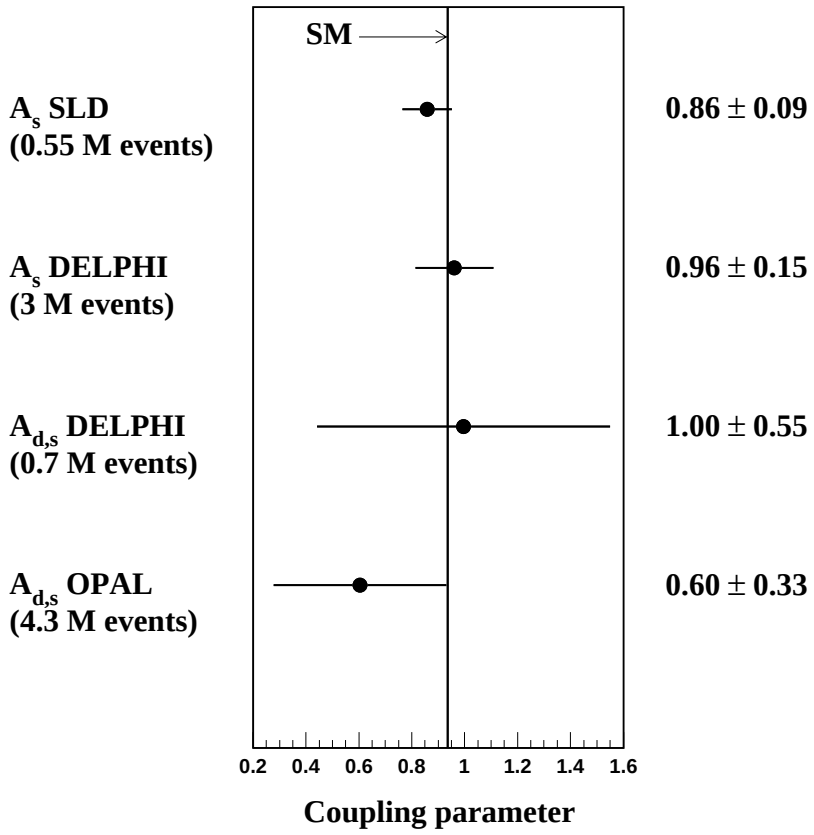

Figure 9.1: Summary of world A_s and $A_{d,s}$ measurements.

Appendix A

SLD Collaboration

K. Abe,[2] K. Abe,[19] T. Abe,[27] I.Adam,[27] T. Akagi,[27] N. J. Allen,[4] A. Arodzero,[20] W.W. Ash,[27] D. Aston,[27] K.G. Baird,[15] C. Baltay,[37] H.R. Band,[36] M.B. Barakat,[14] O. Bardon,[17] T.L. Barklow,[27] J.M. Bauer,[16] G. Bellodi,[21] R. Ben-David,[37] A.C. Benvenuti,[3] G.M. Bilei,[23] D. Bisello,[22] G. Blaylock,[15] J.R. Bogart,[27] B. Bolen,[16] G.R. Bower,[27] J. E. Brau,[20] M. Breidenbach,[27] W.M. Bugg,[30] D. Burke,[27] T.H. Burnett,[35] P.N. Burrows,[21] A. Calcaterra,[11] D.O. Caldwell,[32] D. Calloway,[27] B. Camanzi,[10] M. Carpinelli,[24] R. Cassell,[27] R. Castaldi,[24] A. Castro,[22] M. Cavalli-Sforza,[33] A. Chou,[27] E. Church,[35] H.O. Cohn,[30] J.A. Coller,[5] M.R. Convery,[27] V. Cook,[35] R. Cotton,[4] R.F. Cowan,[17] D.G. Coyne,[33] G. Crawford,[27] C.J.S. Damerell,[25] M. N. Danielson,[7] M. Daoudi,[27] N. de Groot,[27] R. Dell'Orso,[23] P.J. Dervan,[4] R. de Sangro,[11] M. Dima,[9] A. D'Oliveira,[6] D.N. Dong,[17] P.Y.C. Du,[30] R. Dubois,[27] B.I. Eisenstein,[12] V. Eschenburg,[16] E. Etzion,[36] S. Fahey,[7] D. Falciai,[11] C. Fan,[7] J.P. Fernandez,[33] M.J. Fero,[17] K.Flood,[15] R. Frey,[20] T. Gillman,[25] G. Gladding,[12] S. Gonzalez,[17] E.L. Hart,[30] J.L. Harton,[9] A. Hasan,[4] K. Hasuko,[31] S. J. Hedges,[5] S.S. Hertzbach,[15] M.D. Hildreth,[27] J. Huber,[20] M.E. Huffer,[27] E.W. Hughes,[27] X.Huynh,[27] H. Hwang,[20] M. Iwasaki,[20] D. J. Jackson,[25] P. Jacques,[26] J.A. Jaros,[27] Z.Y. Jiang,[27] A.S. Johnson,[27] J.R. Johnson,[36] R.A. Johnson,[6] T. Junk,[27] R. Kajikawa,[19] M. Kalelkar,[26] Y. Kamyshkov,[30] H.J. Kang,[26] I. Karliner,[12] H. Kawahara,[27] Y. D. Kim,[28] R. King,[27] M.E. King,[27] R.R. Kofler,[15] N.M. Krishna,[7] R.S. Kroeger,[16] M. Langston,[20] A. Lath,[17] D.W.G. Leith,[27] V. Lia,[17] C.-J. S. Lin,[27] X. Liu,[33] M.X. Liu,[37] M. Loreti,[22] A. Lu,[32] H.L. Lynch,[27] J. Ma,[35] G. Mancinelli,[26] S. Manly,[37] G. Mantovani,[23] T.W. Markiewicz,[27] T. Maruyama,[27] H. Masuda,[27] E. Mazzucato,[10] A.K. McKemey,[4] B.T. Meadows,[6] G. Menegatti,[10] R. Messner,[27] P.M. Mockett,[35] K.C. Moffeit,[27] T.B. Moore,[37] M.Morii,[27] D. Muller,[27] V.Murzin,[18]

A. SLD COLLABORATION

T. Nagamine,[31] S. Narita,[31] U. Nauenberg,[7] H. Neal,[27] M. Nussbaum,[6] N.Oishi,[19]
D. Onoprienko,[30] L.S. Osborne,[17] R.S. Panvini,[34] H. Park,[20] C. H. Park,[29] T.J. Pavel,[27]
I. Peruzzi,[11] M. Piccolo,[11] L. Piemontese,[10] E. Pieroni,[24] K.T. Pitts,[20] R.J. Plano,[26]
R. Prepost,[36] C.Y. Prescott,[27] G.D. Punkar,[27] J. Quigley,[17] B.N. Ratcliff,[27]
T.W. Reeves,[34] J. Reidy,[16] P.L. Reinertsen,[33] P.E. Rensing,[27] L.S. Rochester,[27]
P.C. Rowson,[8] J.J. Russell,[27] O.H. Saxton,[27] T. Schalk,[33] R.H. Schindler,[27]
B.A. Schumm,[33] J. Schwiening,[27] S. Sen,[37] V.V. Serbo,[36] M.H. Shaevitz,[8] J.T. Shank,[5]
G. Shapiro,[13] D.J. Sherden,[27] K. D. Shmakov,[30] C. Simopoulos,[27] N.B. Sinev,[20]
S.R. Smith,[27] M. B. Smy,[9] J.A. Snyder,[37] H. Staengle,[9] A. Stahl,[27] P. Stamer,[26]
R. Steiner,[1] H. Steiner,[13] M.G. Strauss,[15] D. Su,[27] F. Suekane,[31] A. Sugiyama,[19]
S. Suzuki,[19] M. Swartz,[27] A. Szumilo,[35] T. Takahashi,[27] F.E. Taylor,[17] J. Thom,[27]
E. Torrence,[17] N. K. Toumbas,[27] A.I. Trandafir,[15] J.D. Turk,[37] T. Usher,[27]
C. Vannini,[24] J. Va'vra,[27] E. Vella,[27] J.P. Venuti,[34] R. Verdier,[17] P.G. Verdini,[24]
S.R. Wagner,[27] D. L. Wagner,[7] A.P. Waite,[27] Walston, S.,[20] J.Wang,[27] C. Ward,[4]
S.J. Watts,[4] A.W. Weidemann,[30] E. R. Weiss,[35] J.S. Whitaker,[5] S.L. White,[30]
F.J. Wickens,[25] B. Williams,[7] D.C. Williams,[17] S.H. Williams,[27] S. Willocq,[27]
R.J. Wilson,[9] W.J. Wisniewski,[27] J. L. Wittlin,[15] M. Woods,[27] G.B. Word,[34]
T.R. Wright,[36] J. Wyss,[22] R.K. Yamamoto,[17] J.M. Yamartino,[17] X. Yang,[20]
J. Yashima,[31] S.J. Yellin,[32] C.C. Young,[27] H. Yuta,[2] G. Zapalac,[36] R.W. Zdarko,[27]
J. Zhou.[20]

(The SLD Collaboration)

[1] *Adelphi University, South Avenue- Garden City,NY 11530,*
[2] *Aomori University, 2-3-1 Kohata, Aomori City, 030 Japan,*
[3] *INFN Sezione di Bologna, Via Irnerio 46 I-40126 Bologna (Italy),*
[4] *Brunel University, Uxbridge, Middlesex - UB8 3PH United Kingdom,*
[5] *Boston University, 590 Commonwealth Ave. - Boston,MA 02215,*
[6] *University of Cincinnati, Cincinnati,OH 45221,*
[7] *University of Colorado, Campus Box 390 - Boulder,CO 80309,*
[8] *Columbia University, Nevis Laboratories P.O.Box 137 - Irvington,NY 10533,*
[9] *Colorado State University, Ft. Collins,CO 80523,*
[10] *INFN Sezione di Ferrara, Via Paradiso,12 - I-44100 Ferrara (Italy),*
[11] *Lab. Nazionali di Frascati, Casella Postale 13 I-00044 Frascati (Italy),*
[12] *University of Illinois, 1110 West Green St. Urbana,IL 61801,*

A. SLD COLLABORATION

[13] *Lawrence Berkeley Laboratory, Dept.of Physics 50B-5211 University of California-Berkeley,CA 94720,*
[14] *Louisiana Technical University, ,*
[15] *University of Massachusetts, Amherst,MA 01003,*
[16] *University of Mississippi, University,MS 38677,*
[17] *Massachusetts Institute of Technology, 77 Massachussetts Avenue Cambridge,MA 02139,*
[18] *Moscow State University, Institute of Nuclear Physics 119899 Moscow Russia,*
[19] *Nagoya University, Nagoya 464 Japan,*
[20] *University of Oregon, Department of Physics Eugene,OR 97403,*
[21] *Oxford University, Oxford, OX1 3RH, United Kingdom,*
[22] *Universita di Padova, Via F. Marzolo,8 I-35100 Padova (Italy),*
[23] *Universita di Perugia, Sezione INFN, Via A. Pascoli I-06100 Perugia (Italy),*
[24] *INFN, Sezione di Pisa, Via Livornese,582/AS Piero a Grado I-56010 Pisa (Italy),*
[25] *Rutherford Appleton Laboratory, Chiton,Didcot - Oxon OX11 0QX United Kingdom,*
[26] *Rutgers University, Serin Physics Labs Piscataway,NJ 08855-0849,*
[27] *Stanford Linear Accelerator Center, 2575 Sand Hill Road Menlo Park,CA 94025,*
[28] *Sogang University, Ricci Hall Seoul, Korea,*
[29] *Soongsil University, Dongjakgu Sangdo 5 dong 1-1 Seoul, Korea 156-743,*
[30] *University of Tennessee, 401 A.H. Nielsen Physics Blg. - Knoxville,Tennessee 37996-1200,*
[31] *Tohoku University, Bubble Chamber Lab. - Aramaki - Sendai 980 (Japan),*
[32] *U.C. Santa Barbara, 3019 Broida Hall Santa Barbara,CA 93106,*
[33] *U.C. Santa Cruz, Santa Cruz,CA 95064,*
[34] *Vanderbilt University, Stevenson Center,Room 5333 P.O.Box 1807,Station B Nashville,TN 37235,*
[35] *University of Washington, Seattle,WA 98105,*
[36] *University of Wisconsin, 1150 University Avenue Madison,WS 53706,*
[37] *Yale University, 5th Floor Gibbs Lab. - P.O.Box 208121 - New Haven,CT 06520-8121.*

References

[1] LEPEWWG/98-01, ALEPH 98-037 PHYSICS 98-018, DELPHI 98-46 PHYS 774, L3 Note 2259, OPAL Technical Note TN 541, SLD Physics Note 68 (1998).

[2] Presented at the 34^{th} Rencontres de Moriond, Electroweak Interactions and Unified Theories, Les Arcs, France, March 1999.

[3] DELPHI Collaboration, P. Abreu et al., Z. Phys. **C67** (1995) 1.

[4] OPAL Collaboration, K. Ackerstaff et al., Z. Phys. **C76** (1997) 387.

[5] K. G. Baird, Ph.D. Thesis, Rutgers University, Piscataway, NJ (1996), SLAC-R-483.

[6] T. J. Pavel, Ph.D. Thesis, Stanford University, Stanford, CA (1997), SLAC-R-491.

[7] M. O. Dima, Ph.D. Thesis, Colorado State University, Fort Collins, CO (1997), SLAC-R-505.

[8] SLD Collaboration, K. Abe et al., Phys. Rev. Lett. **78** (1997) 3442.

[9] SLD Collaboration, K. Abe et al., Phys. Rev. **D59** (1999) 52001.

[10] F. Halzen and A. D. Martin, Quarks and Leptons: An Introductory Course in Modern Particle Physics, John Wiley & Sons, New York (1984).

[11] D. J. Griffiths, Introduction to Elementary Particles, John Wiley & Sons, New York (1987).

[12] P. Langacker (ed.), World Scientific (1995).

[13] S. L. Glashow, Nucl. Phys. **22** (1961) 579.

[14] A. Salam and J. C. Ward, Phys. Lett. **13** (1964) 168.

[15] S. Weinberg, Phys. Rev. Lett. **19** (1967) 1264.

[16] P. Clarke, An Introduction to Cross-sections and Asymmetries using Polarized Beams in High-Energy e^+e^- Colliders, RAL-90-055 (1990).

[17] P. W. Higgs, Phys. Lett. **12** (1964) 132.
P. W. Higgs, Phys. Rev. Lett. **13** (1964) 508.

[18] UA-1 Collaboration, G. Arnison et al., Phys. Lett. **122B** (1983) 103.
UA-1 Collaboration, G. Arnison et al., Phys. Lett. **126B** (1983) 398.

[19] The European Physics Journal **C3,1** (1998).

[20] A. Lath, Ph.D. Thesis, Massachusetts Institute of Technology (1994), SLAC-R-454.

[21] Presented at the International Europhysics Conference on High Energy Physics, Tampere, Finland, July 1999.

[22] D. J. Gross and F. Wilczek, Phys. Rev. Lett. **30** (1973) 1343.

[23] D. H. Politzer, Phys. Rev. Lett. **30** (1973) 1346.

[24] M. Gell-Mann, Phys. Lett. **8** (1964) 214.

[25] G. Zweig, CERN-TH-8182 and CERN-TH-8419 (1964).

[26] M. Y. Han and Y. Nambu, Phys. Rev.**139** (1965) 1806.

[27] M. Breidenbach et al., Phys. Rev. Lett. **23** (1969) 935.

[28] J. D. Bjorken, Phys. Rev. **179** (1969) 1547.

[29] MARK I Collaboration, G. Hanson et al., Phys. Rev. Lett. **35** (1975) 1609.

[30] MARK I Collaboration, D. P. Barber et al., Phys. Rev. Lett. **43** (1979) 830.
PLUTO Collaboration, C. Berger et al., Phys. Lett. **B86** (1979) 418.
TASSO Collaboration, R. Brandelik et al., Phys. Lett. **B86** (1979) 243.
JADE Collaboration, W. Bartel et al., Phys. Lett. **B91** (1980) 142.

[31] J. Ellis, M. K. Gaillard, and G. G. Ross, Nucl. Phys. **B111** (1976) 253; erratum **B130** (1977) 516.

[32] A. Ali et al., Nucl. Phys. **B167** (1980) 229.

[33] K. J. F. Gaemers, J. A. M. Vermaseren, Z. Physik **C7** (1980) 81.

[34] V. N. Gribov and L. N. Lipatov, Yad. Fiz. **15** (1972) 781, 1218 (Sov. J. Nucl. Phys. **15** (1972) 438, 675).

[35] Y. L. Dokshitzer, Zh. Eksp. Teor. Fiz. **73** (1977) 1216 (Sov. Phys. JETP, **46** (1977) 641).

[36] G. Altarelli and G. Parisi, Nucl. Phys. **B126** (1977) 298.

[37] T. Sjöstrand et al., "Z Physics at LEP 1", CERN Yellow Book 89-08, vol.3, 143.

[38] R. D. Field and R. P. Feynman, Nucl. Phys. **B136** (1978) 1.

[39] G. Marchesini and B. R. Webber, Nucl. Phys. **B310** (1988) 453.

[40] X. Artru and G. Mennessier, Nucl. Phys. **B70** (1974) 93.

[41] B. Andersson, G. Gustafson and T. Sjöstrand, Z. Phys. **C6** (1980) 235.

[42] T. Sjöstrand, Comput. Phys. Commun. **39** (1986) 347.

[43] B. Foster, Electron-Positron Annihilation Physics (1990).

[44] G. Marchesini et al., Comput. Phys. Commun. **67** (1992) 465.

[45] S. Chun and C. Buchanan, Phys. Rep. **292** (1998) 239.

[46] T. Sjöstrand, Comput. Phys. Commun. **82** (1994) 74.

[47] SLD Design Report, SLAC-R-273, UC-43D (1984).

[48] SLC Design Report, SLAC-R-229 (1980).

[49] P. L. Reinertsen et al., SLAC-PUB-8029 (1998).
Presented at the 5^{th} International Workshop on Tau Physics, Santander, Spain (1998).

[50] R. C. Field et al., OREXP 97-04 (1997).
D. Onoprienko et al., UTKHEP 97-20 (1997).
R C. Field et al., IEEE Trans. Nucl. Sci. **45** (1998) 670.
S .C. Berridge et al., in: Calorimetry in High Energy Physics Proceedings,
ed. E. Cheu et al., World Scientific, Singapore (1998) 170.

[51] H. R. Band et al., Nucl. Instr. Meth. **A400** (1997) 24.

[52] J. Kent et al., SLAC-PUB-4922 (1989).

[53] P. C. Rowson et al., SLD Note 264 (1999).

[54] M. Fero et al., SLD Physics Note 50 (1996).

[55] K. T. Pitts, Ph.D. Thesis, University of Oregon, Eugene (1994), SLAC-R-446.

[56] C. J. S. Damerell et al., Nucl. Instr. Meth. **A288** (1990) 236.
C. J. S. Damerell et al., Nucl. Instr. Meth. **A400** (1997) 287.
K. Abe et al., SLAC-PUB-7385 (1997).

[57] M. Strauss et al., SLAC-PUB-6686 (1994).

[58] T. Abe et al., SLAC-PUB-8239 (1999).
Presented at the 8^{th} International Workshop on Vertex Detectors, VERTEX99, Netherlands, June 1999.

[59] M. D. Hildreth et al., Nucl. Instr. Meth. **A367** (1995) 111.

[60] J. P.Venuti and G. B. Chadwick, IEEE Trans. Nucl. Sci. **NS-36** (1989) 595.

[61] H. Neal, Ph.D. Thesis, Stanford University, Stanford, CA (1995), SLAC-R-473.

[62] D. C. Williams, Ph.D. Thesis, Massachusetts Institute of Technology, Cambridge, MA (1994), SLAC-R-445.

[63] M. D. Hildreth et al., IEEE Trans. Nucl. Sci. **NS-42** (1995) 451.

[64] SLD Collaboration, K. Abe et al., Phys. Rev. **D53** (1996) 1023.

[65] K. Abe et al., Nucl. Inst. Meth. **A343** (1994) 74.

[66] D. Axen et al., Nucl. Inst. Meth. **A328** (1993) 472.

[67] S. Gonzalez, Ph.D. Thesis, Massachusetts Institute of Technology, Cambridge, MA (1994), SLAC-R-439.

[68] A. C. Benvenuti et al., Nucl. Inst. Meth. **A276** (1989) 94.

[69] E. Iarocci, Nucl. Inst. Meth. **A217** (1983) 30.

[70] P. N. Burrows et al., SLD Note 229 (1993).

[71] SLD Collaboration, K. Abe et al., Phys. Rev. **D51** (1995) 962.

[72] A. Marchioro et al., IEEE Trans. Nucl. Sci. **NS-34** (1987) 133.

[73] P. N. Burrows, Z. Phys. **C41** (1988) 375.
OPAL Collaboration, M. Z. Akrawy et al., Z. Phys. **C47** (1990) 505.
P. N. Burrows and H. Masuda, SLD Note 36 (1995).

[74] C. Peterson et al., Phys. Rev. **D27** (1983) 105.

[75] SLD Collaboration, K. Abe et al., Phys. Rev. Lett. **79** (1997) 590.

[76] ARGUS Collaboration, H. Albrecht et al., Z. Phys. **C54** (1992) 13.
ARGUS Collaboration, H. Albrecht et al., Z. Phys. **C58** (1993) 191.

[77] M. Thulasidas, Ph.D. Thesis, Syracuse University, Syracuse, NY (1993).

[78] R. Brun et al., GEANT3, CERN-DD/EE/84-1 (1987).
CERN Application Software Group, GEANT 3.21 Program, CERN Program Library (1994).

[79] W. Nelson, H. Hirayama, D. W. O. Rogers, SLAC-R-265 (1985).

[80] H. C. Fesefeldt, Simulation of Hadronic Showers, Physics and Applications, Technical Report PITHA 85-02, III Physikalisches Institut, Aachen, Germany (1985).

[81] J. Séguinot, T. Ypsilantis, Nucl. Inst. Meth. **A343** (1994) 1.

[82] P. A. Cherenkov, Dok. Akad. Nauk., SSSR **2** (1934) 451.

[83] I. M. Frank and I. E. Tamm, Dok. Akad. Nauk., SSSR **14** (1937) 109.

[84] W. R. Leo, Techniques for Nuclear and Particle Physics Experiments, Springer-Verlag, Berlin (1994).

[85] V. L. Ginzburg, Zh. Eksp. Teor. Fiz. **10** (1940) 589, 608.

[86] A. Roberts, Nucl. Inst. Meth. **9** (1960) 55.

[87] J. Séguinot, T. Ypsilantis, Nucl. Inst. Meth. **142** (1977) 377.

[88] D. F. Anderson, Nucl. Inst. Meth. **178** (1980) 125.

[89] DELPHI 82-1/CERN-LEPC 82-8 and LEPC-16 (1982).

[90] K Abe et al., IEEE Trans. Nucl. Sci. **NS-42** (1995) 518.

[91] J. Séguinot, T. Ypsilantis, Nucl. Inst. Meth. **A343** (1994) 30.

[92] H. Kawahara and J. Va'vra, SLD CRID Note 78 (1993).

[93] K. Abe et al., Novosibirsk Instrumentation Workshop, World Scientific (1990) 221.

[94] T. Bienz, Ph.D. Thesis, Stanford University, Stanford, CA (1990), SLAC-R-369.

[95] J. Vavra et al., SLAC-PUB-7705 (1997).
Presented at the IEEE Nuclear Science Symposium and Medical Imaging Conference, Albuquerque, New Mexico, November 1997.

[96] S. J. Yellin, SLD CRID Note 49 (1988).

[97] K. Abe et al., Nucl. Inst. Meth. **A371** (1996) 195.

[98] D. R. Muller et al., SLAC-PUB-8163 (1999).
Contributed to the International Europhysics Conference on High Energy Physics, Tampere, Finland, July 1999.

[99] T. R. Wright et al., SLAC-PUB-8199 (1999).
Contributed to the International Europhysics Conference on High Energy Physics, Tampere, Finland, July 1999.

[100] K. Abe et al., SLAC-PUB-8200 (1999).
Contributed to the International Europhysics Conference on High Energy Physics, Tampere, Finland, July 1999.

[101] SLD Collaboration, K. Abe et al., Phys. Rev. **D53** (1996) 1023.

[102] M. D. Hildreth, Ph.D. Thesis, Stanford University, Stanford, CA (1995), SLAC-R-458, M. D. Hildreth et al., SLAC-PUB-95-6687 (1995).

[103] K. Hayes, Proceedings of the Third Mark II Workshop on SLC Physics, SLAC-315 (1987).

[104] MARK II Collaboration, R. G. Jacobsen et al., Phys. Rev. Lett. **67** (1991) 3347.

[105] R. G. Jacobsen, Ph.D. Thesis, Stanford University, Stanford, CA (1991), SLAC-R-381.

[106] N. Oishi, Ph.D. Thesis, Nagoya University, Nagoya, Japan (1999), SLAC-R-545.
SLD Collaboration, K. Abe et al., Phys. Rev. **D59** (1999) 12002.

[107] TASSO Collaboration, R. Brandelik et al., Phys. Lett. **B139** (1984) 126.
TPC Collaboration, H. Aihara et al., Phys. Rev. Lett. **57** (1986) 3140.
OPAL Collaboration, P. D. Acton et al., Phys. Lett. **B305** (1993) 415.
ALEPH Collaboration, D. Buskulic et al., Z. Phys. **C64** (1994) 361.
DELPHI Collaboration, P. Abreu et al., Phys. Lett. **B416** (1998) 247.

[108] TASSO Collaboration, R. Brandelik et al., Phys. Lett. **B100** (1981) 357.
TPC Collaboration, H. Aihara et al., Phys. Rev. Lett. **53** (1984) 2199.
A. Breakstone et al., Z. Phys. **C25** (1984) 21.

[109] A. Böhrer et al., Physics Reports **291** 3-4 (1997) 107.

[110] J. B. Stav and H. A. Olsen, Phys. Rev. **D52** (1995) 1359.

[111] P. N. Burrows, SLD Physics Note 29 (1994).

[112] K. Abe et al., SLD Physics Note 66 (1998).

[113] V. V. Serbo, Ph.D. Thesis, University of Wisconsin, Madison (1997), SLAC-R-510.

[114] DELPHI Collaboration, P. Abreu et al. (1998).
Contributed to the International Conference on High Energy Physics, Vancouver, B.C. Canada, July 1998.